2009-02-01

Spectroscopic Imaging of Quantum Dot Cellular Interactions

Lorenzo Salford
Technological University Dublin

Recommended Citation
Salford, L. (2009). *Spectroscopic Imaging of Quantum Dot Cellular Interactions*. Master dissertation. Technological University Dublin. doi:10.21427/D75P6X

Spectroscopic Imaging of Quantum Dot Cellular Interactions

by

Lorenzo Salford

A thesis submitted to the Dublin Institute of Technology in partial fulfilment for the degree of

Master of Philosophy

Supervisors: Prof. Hugh J. Byrne
Mr Aidan Meade
Dr Fiona Lyng

Radiation and Environmental Science Centre / School of Physics,
Focas Research Institute, Dublin Institute of Technology

February 2009

TRAINOR, THE DRUGGIST

Only the chemist can tell, and not always the chemist,

what will result from compounding

Fluids or solids.

And who can tell

How men and women will interact

On each other, or what children will result?

There were Benjamin Pantier and his wife,

Good in themselves, but evils toward each other:

He oxygen, she hydrogen,

Their son, a devastating fire.

I Trainor, the druggist, a mixer of chemicals,

Killed while making an experiment,

Lived unwedded.

Spoon River Antology – Edgar Lee Masters

Abstract

Quantum dots (QDs) are a diverse class of engineered nanomaterials that have great potential for use as agents in imaging, diagnostics and drug-delivery because of their intense and photostable fluorescence. Advances in the field of nanotoxicology, however, have recently identified potential risks and hazards associated with exposure to QDs**.** The main purpose of this research is to investigate the capabilities of a synergistic range of different techniques, including cytotoxicity assays, confocal microscopy and vibrational spectroscopy, to probe their interaction with Biological systems. With the combination of these techniques it is hoped to understand the mechanisms of the interaction of QDs with biological systems.

Cytotoxicity assays demonstrate that polyethylene glycol (PEG) coated CdSe/ZnS quantum dots are at most weakly cytotoxic upon prolonged exposure. Simultaneous exposure to simulated solar illumination indicates an increased cytotoxic response and potential risks of phototoxicity.

Fluorescence and Confocal Microscopy studies demonstrate that the internalization of QDs within HaCaT keratinocytes occurs within 1 hour of exposure, and that QDs are retained in the lysosomes supporting a model of internalisation by endocytosis.

Using an excitation wavelength of 785 nm, the two-photon excitation fluorescence of QDs (emission at 625 nm) is observed, whereby the fluorescent emission is observed in the anti-Stokes Raman signal, together with the usual Stokes Raman scatter of a single cell. Raman microspectroscopy therefore offers the means to both localise (image) and

study the chemical interaction between a nanoparticle and its biological environment as well as the overall changes to the physiology of the cell as a result of interaction with the nanoparticles.

Localisation of QDs is possible due to the high fluorescence of these nanomaterials. In the last chapter a novel technique is investigated for detection of non fluorescent nanomaterials within a cell. The characteristic Raman signature of the nanoparticles is extracted from the mixed nanoparticle/cellular spectrum using a cross correlation technique, and the signature is colocalised with the fluorescent signal in the case of QDs. The technique is validated using simulations and experimental data.

Declaration

I certify that this thesis which I now submit for examination for the award Master of Philosophy (MPhil), is entirely my own work and has not been taken from the work of others, save and to the extent that such work has been cited and acknowledged within the text of my work.

This thesis was prepared according to the regulations for postgraduate study by research of the Dublin Institute of Technology and has not been submitted in whole or in part for another award in any Institute.

The work reported on in this thesis conforms to the principles and requirements of the Institute's guidelines for ethics in research.

The Institute has permission to keep, lend or copy this thesis in whole or in part, on condition that any such use of the material of the thesis be duly acknowledged.

Signature ____________________ Date _______________

Acknowledgements

First of all I would like to thank my supervisor Hugh. J. Byrne for the generosity and intelligence with which he help me with the completion of my thesis.

I am grateful to my other two supervisors, Fiona Lyng and Aidan Meade for their guidance, time and advice.

There were many people who gave interesting feedback and valuable suggestions, for which I would like to thank them: Franck Bonnier, Kelvin Poon, Peter Knife, and Alan Casey.

A special thanks to Amaya Garcia for her help with the cell microscopy.

Finally of course a huge thanks to everyone at the Focas Institute to make my time here so enjoyable. I also wish to thank the "Spanish crowd" for the enjoyable lunches and the laughs. Un agradecimiento sincero a Rosa, Amaya, Sabrina, Maria y Susy.

Un grazie sentito a tutti quelli che hanno percorso un tratto della mia vita irlandese: Chiara Cam., Chiara Col., Murat, Juan, Vivi, Luis, Gabriele.

This project was supported by the National Biophotonics and Imaging Platform (NBIP) Ireland funded under the Higher Education Authority PRTLI (Programme for Research in Third Level Institutions) Cycle 4, co-funded by the Irish Government and the European Union.

Investing in your future

Ireland's EU Structural Funds
Programmes 2007 - 2013

Co-funded by the Irish Government
and the European Union

EUROPEAN REGIONAL
DEVELOPMENT FUND

An Roinn Oideachais agus Eolaíochta
Department of Education and Science

HEA
Higher Education Authority
An tÚdarás um Ard-Oideachas

Abbreviations

AB	Alamar Blue™
ATCC	American type culture collection
BSA	Bovine serum albumin
C_{60}	Fullerene
CO_2	Carbon dioxide
CLSM	Confocal laser scanning microscope
DMEM-F12	Dubecco’s modified essential medium-F12 nutrient mix
DMSO	Dimethylsulfoxide
EC	European Commission
EC_{50}	Effective concentration leading to a 50% response
FU	Fluorescent units
SD	Standard Deviation
SPEF	Single Photon Excitation Fluorescence
TPEF	Two Photon Excitation Fluorescence
RLU	Relative light units

Table of Contents

Page

Chapter 1

Introduction 1

1.1 Objectives 2

1.2 Background on Quantum dots 3

1.2.1 Introduction to Quantum confinement 3

1.2.2 Semiconductor – Band Theory of Solid 4

1.2.3 Exciton Theory 6

1.2.4 Quantum dots: theoretical description 7

1.2.5 Luminescence process 10

1.2.6 Properties of QDs 10

1.2.7 Applications of Quantum dots 12

1.2.8 Biological application of Quantum dots 13

1.3 Toxicology of Quantum dots 15

1.3.1 *In vitro* studies 16

1.4 Summary and Project outline 22

1.5 References 24

Chapter 2

Experimental Methods: Characterisation of Semiconductor QDs 26

2.1 Evident Quantum Dots 27

2.1.1 Core - CdSe 27

2.1.2 Shell - ZnS 29

2.1.3 Organic Coating – Polyethylene glycol 30
2.1.4 Commercially available Quantum Dots 31
2.2 Characterization of Quantum dots 32
2.2.1 Evident Technologies Certificate of Analysis 32
2.2.2 Size 33
2.2.3 Optical Properties 34
2.2.4 Vibrational characterisation 37
2.2.4.1 Infra Red spectroscopy 38
2.2.4.2 Raman spectroscopy 40
2.3 Imaging of QDs 42
2.3.1 Confocal Fluorescence Imaging 42
2.3.2 Raman imaging 44
2.3.3 Two Photon Excitation Fluorescence (TPEF) 46
2.3.4 Two photon fluorescence 48
2.4 Summary 56
2.5 References 57

Chapter 3

Interaction of QDs with cells 58
3.1 Introduction 59
3.2 Materials and Methods 59
3.2.1 Cell culture 59
3.2.2 Quantitative cytotoxicity assessments 60
3.2.2.1 Alamar Blue and Neutral Red assays 61
3.2.2.2 MTT assay 62
3.2.3 Phototoxicity 63

3.2.3.1 Methodology of QDs Phototoxicity assay 63
3.2.4 Confocal Microscopy 65
3.2.5 Statistic 66
3.2.6 Raman mapping of HaCaT cells 66
3.2.7 Hybrid Confocal Raman Fluorescence 68
3.3 Results 69
3.3.1 Cytotoxicity 69
3.3.1.1 Time dependent and dose dependent cytotoxicity 69
3.3.2 Phototoxicity 72
3.3.3 In vitro imaging 74
3.3.3.1 Internalization 75
3.3.3.2 Colocalisation 76
3.3.4 Raman mapping 78
3.4 Conclusion 80
3.4.1 Cytotoxicity 80
3.4.2 Phototoxicity 80
3.4.3 Raman mapping 81
3.4 References 81

Chapter 4

Localisation of QDs using Raman Cross-correlation 82

4.1 Cross Correlation 83
4.1.1 Introduction 84
4.1.2 Cross correlation - Theory 86
4.1.3 CC for identification of external agents in Raman Spectra 87

4.2 Cross-correlation of simulated spectra – Theoretical study 88

4.2.1 Raw data 88

4.2.2 Baseline correction 93

4.2.3 Baseline correction plus filtering.. 98

4.2.4 Filtering and First derivative 101

4.2.5 Conclusion 105

4.3 Cross-correlation- Experimental Study 106

4.3.1 First experiment 111

4.3.2 Second experiment 114

4.3.3 Third experiment 117

4.3.4 Fourth experiment.. 120

4.4 Conclusion 124

4.5 References 125

Chapter 5

Conclusion. 126

Appendix A

MATLAB codes**..I**

Appendix B

Awards, workshops, conferences and training **.....................................XXI**

Table of Figures

Page

Figure 1.1: Valence and conduction bands of metal, insulator, and semiconductor 5

Figure 1.2: A comparison of energy levels between a bulk semiconductor and a quantum dot.................. 9

Figure 1.3: Solution of different sized Quantum dots 11

Figure 1.4: Absorption and emission spectra of 490QDs... 12

Figure 1.5: Quantum dots biological application scheme. 14

Figure 1.6: HaCaT cells. 14

Figure 2.1: Schematic structure of ZnS capped CdSe Quantum dots.. 28

Figure 2.2: 2 Photoluminescence spectra of CdSe-ZnS quantum dots with different core sizes. Quantum dots were excited at 350nm. 30

Figure 2.3: Evident Technologies non functionalized CdSe/ZnS with PEG coating QDs.. 31

Figure 2.4: Absorption spectra of 490QDs and 625QDs.. 36

Figure 2.5: Emission spectra of 490QDs and 625QDs.. 37

Figure 2.6: FTIR spectrum of 625QDs. 40

Figure 2.7: Raman spectrum of 490QDs. 44

Figure 2.8: Raman spectrum of 625QDs 43

Figure 2.9: Confocal laser scanning microscope (Zeiss LSM 510 META). 45

Figure 2.10: Optical and Confocal Fluorescence images of 490QDs on a quartz slide (excitation wavelength = 458nm). 46

Figure 2.11: Raman spectrum of 625QDs in the range from -8000 to 8000 cm^{-1} 81

Figure 2.12: Raman spectrum of 490QDs in the range from -8000 to 8000 cm^{-1} 83

Figure 2.13: Raman spectrum of 625QDs in the range from -8000 to 8000 cm^{-1}. 85

Figure 2.14: Plot of the intensity OUT Vs the intensity IN in logarithmic scale. 51

Figure 2.15: QDs Fluorescence emission in function of time of acquisition and intensity of beam 52

Figure 2.16: SPEF and TFEF of fluorescein 57

Figure 2.17: Z-profile of the 2PEF of 625QDs. Parameters: ex: 785 nm, 15 sec X 2, -2 to 2 µm, Z increment 0.5 µm 58

Figure 3.1 Q-Sun xenon solar simulator test chamber 63

Figure 3.2: Schematic of Phototoxicity assay 64

Figure 3.3: Hybrid Confocal Fluorescence Scheme. 66

Figure 3.4: AB and NR response at 24 and 48 hrs reduction with respect to the control…………..………70

Figure 3.5: AB, NR and MTT response at 72 and 96 hrs reduction with respect to the control…………71

Figure 3.6: MTT response after 1 hr QDs exposure and 30 min of Q-sun exposurewith respect to the control………………………………………………………………………………………… ..…73

Figure 3.7: Confocal slices through the volume of a cell incubated with the QD625 show that the signal originates from the cell interior and not from material adhered to the surface.. 75

Figure 3.8: Images shows the *z,x* section (upper panel) and the *z,y*section (right panel) cutting orthogonally through the cell obtained from *z*-stack image series of the cells. QDs were observed in perinuclear clusters inside the cells. 76

Figure 3.9: Confocal images of HaCaT cell with green Lysotracker (A) and with 625QDs (B)………. 78

Figure 3.10: QDs localization within a single cell. (A) laser line 785. (B) laser line 473. The differential intensity of the QDs emission possibly depends on the concentration of the QDs and on the distance from the focal plane 79

Figure 4.1: QDs and HaCaT cell Raman spectra. 87

Figure 4.2: Cross-correlation of QD spectrum and simulated spectra.. 88

Figure 4.3: Cross-correlation maxima Vs concentration of QDs spectrum in cell spectrum 90

Figure 4.4 Cross-correlation of QDs spectrum and simulated spectra – reduced range............................ 90

Figure 4.5: Cross-correlation maxima Vs concentration of QDs spectrum in cell spectrum 91

Figure 4.6: Effects Spectra of HaCaT cells and QDs before and after the baseline subtraction. 92

Figure 4.7: Cross-correlation among QDs spectrum and simulated spectra.. 93

Figure 4.8 Cross-correlation maxima Vs concentration of QDs spectrum in cell spectrum 94

Figure 4.9: Cross-correlation among QDs spectrum and “artificial” cells spectra.................................... 95

Figure 4.10: Cross-correlation maxima Vs concentration of QDs spectrum in cell spectrum 96

Figure 4.11: Cross-correlation among QDs spectrum and “artificial” cells spectra.................................. 96

Figure 4.12: Cross-correlation maxima Vs concentration of QDs spectrum in cell spectrum 97

Figure 4.13: Cross-correlation among QDs spectrum and “artificial” cells spectra……………………...98

Figure 4.14: Cross-correlation maxima Vs concentration of QDs spectrum in cell spectrum 99

Figure 4.15 Cross-correlation among QDs spectrum and “artificial” cells spectra 100

Figure 4.16: Cross-correlation maxima Vs concentration of QDs spectrum in cell spectrum. 101

Figure 4.17: Cross-correlation among QDs spectrum and “artificial” cells spectra 102

Figure 4.18: Cross-correlation among QDs spectrum and “artificial” cells spectra. 103

Figure 4.19: Line Raman mapping of a single HaCaT cells 104

Figure 4.20: Raman scheme of TPEE and finger print region Raman spectra. 104

Figure 4.21: 473 nm Raman mapping generates the QDs fluorescence distribution within a cell. 107

Figure 4.22: Cross-correlation of 17 points of a single HaCaT cell (the max curve is the autocorrelation of the QDs spectrum) 108

Figure 4.23: Cross-correlation maxima (Stokes side) Vs fluorescence maxima (anti-Stokes side).. 110

Figure 4.24: Cross-correlation maxima Vs fluorescence maxima. 111

Figure 4.25: Cross-correlation 17 points of an HaCaT cell. 111

Figure 4.26: Cross-correlation maxima (Stokes side) Vs fluorescence maxima (anti-Stokes side)……. 112

Figure 4.27: Cross-correlation of 11 points of a HaCaT cell. 113

Figure 4.28: Cross-correlation maxima (Stokes side) Vs fluorescence maxima (anti-Stokes side 113

Figure 4.29: Cross-correlation of 11 points of a HaCaT cell. 114

Figure 4.30: Cross-correlation maxima (Stokes side) Vs fluorescence maxima (anti-Stokes side)……. 115

Figure 4.31: Cross-correlation of 11 points of a HaCaT cell. 115

Figure 4.32: Cross-correlation maxima (Stokes side) Vs fluorescence maxima (anti-Stokes side 116

Figure 4.33: Cross-correlation of 11 points of a HaCaT cell. 116

Figure 4.34: Cross-correlation maxima (Stokes side) Vs fluorescence maxima (anti-Stokes side)……..117

Figure 4.35: Cross-correlation of 11 points of a HaCaT cell. 117

Figure 4.36: Cross-correlation maxima (Stokes side) Vs fluorescence maxima (anti-Stokes side) 118

Figure 4.37: Cross-correlation of 11 points of a HaCaT cell. 119

Figure 4.38: Cross-correlation maxima (Stokes side) Vs fluorescence maxima (anti-Stokes side) 119

Figure 4.39: Cross-correlation of 8 points of a HaCaT cell. 120

Figure 4.40: Cross-correlation maxima (Stokes side) Vs fluorescence maxima (anti-Stokes side). 120

Figure 4.41: Cross-correlation of 11 points of a HaCaT cell. 121

Figure 4.42: Cross-correlation maxima (Stokes side) Vs fluorescence maxima (anti-Stokes side). 122

Figure 4.43: Cross-correlation of 11 points of a HaCaT cell. 122

Figure 4.44: Cross-correlation maxima in the X axis and fluorescence maxima in the Y axis for the all experimental data. 123

Table of Tables

Page

Table 1.1 Summary of the literature review about the QDs toxicity 19

Table 1.2 Summary of the literature review about the QDs toxicity 20

Table 1.3 Summary of the literature review about the QDs toxicity 21

Table 2.1 625QDs certificate of analysis 31

Table 2.2 Assignment of FTIR spectrum of 625QDs 37

Table 2.3 Assignment of Raman spectrum of 625QDs 41

Table 3.1 Raman mapping parameters 67

Table 4.1 Cross-correlation parameters 105

Chapter 1

Introduction

1.1 Objectives

Quantum dots (QDs) are already widely used in emerging and existing technologies and thus it is important to investigate their toxicity and biocompatibility. Before the use of these nanoparticles becomes widespread, the potential occupational and environmental hazards need to be acknowledged.

There are various exposure routes for manufactured nanoparticles; they can enter the body through inhalation, ingestion and dermal absorption. Furthermore nanocrystalline fluorophores such as QDs have several potential medical applications including nanodiagnostics, imaging, targeted drug delivery, and photodynamic therapy. For these kind of applications, the nanoparticles may be directly injected into the body or transported transdermally. In the latter case, the risk of phototoxicity due to exposure to sunlight should also be considered. With respect to *in vivo* applications, a particular caution must be exercised with QDs due to their potentially toxic constituent components (CdSe).

In this study, the focus is on dermal absorption risks by analysis of the interaction of QDs with keratinocyte cells. The skin is the largest organ of the body with a huge surface area (1.6-2 m^2) and represents an important potential exposure route. Moreover, QDs are readily detected because of their intense and photostable fluorescence, making them a useful model for assessing nanomaterial interactions with biological systems in general.

The main purpose of the research is to investigate the capabilities of a synergistic range of different techniques to probe the interaction of QDs with cells. These include cytotoxicity assays, confocal microscopy and vibrational spectroscopy. With the combination of these techniques it is hoped to understand the mechanisms of the interaction of QDs with biological systems.

1.2 Background on Quantum dots

1.2.1 Introduction to Quantum confinement

In general, the energy of electrons in a semiconductor is limited by their temperature and by the properties of the material. Electrons confined in a plane have no freedom of motion in a third dimension. Those confined in a quantum wire are free to move in one dimension only, and those confined in a quantum dot are not free in any dimension.

During the early 1970s, groups at AT&T Bell laboratories and IBM made the first two-dimensional "quantum well", demonstrating quantum confinement in a semiconductor for the first time [1]. The first demonstration of zero-dimensional semiconductors followed in the early 1980s, at Ioffe Physical Technical Institute in St. Petersburg [2].

These zero –dimensional semiconductors, also known as Quantum Dots or nanocrystals, are a special class of semiconductor composed of periodic groups of II-IV, III-V, or IV-VI materials. They consist of only a few hundred to thousand atoms within the quantum dot volume. With a diameter of 10 to 50 atoms; they bridge the gap between the solid-state and atomic properties of inorganic materials [3].

QDs have attracted considerable interest as materials for optical and nonlinear optical applications [4], and their systematically controllable physical properties render them ideal materials for understanding structure property relationships at the nanoscale.

1.2.2 Semiconductor – Band theory of solids

The electronic band structure of a solid describes the ranges of energy that an electron is "forbidden" or "allowed" to have. Thus the bands of possible electron energy levels in a solid are called allowed energy bands. The bands that are impossible for an electron to have in are called forbidden bands, or bandgaps. The allowed energy bands sometimes overlap and sometimes are separated by forbidden bands.

The lowermost, almost fully occupied band is called the valence band. The uppermost, almost unoccupied band is called the conduction band, because only when electrons are excited to the conduction band can current flow in these materials. The energy difference between the top of the valence band and the bottom of the conduction band, called bandgap, can define three different classes of materials: metals, semiconductors and insulators (Figure 1.1).

In metals, the bandgap is negative or zero and there is just a single band, a valence-conduction band that is partially filled. There is therefore no energy gap between the valence and conduction states and electrons are mobile without the necessity of external energy.

In insulators and semiconductors there is a finite positive bandgap. The presence of a gap means that the electrons cannot easily be accelerated into higher energy states by an applied electric field. Insulators are differentiated from semiconductors by the size of the bandgap, a general rule of thumb being that materials with a bandgap > 3-4eV are classed as insulators.

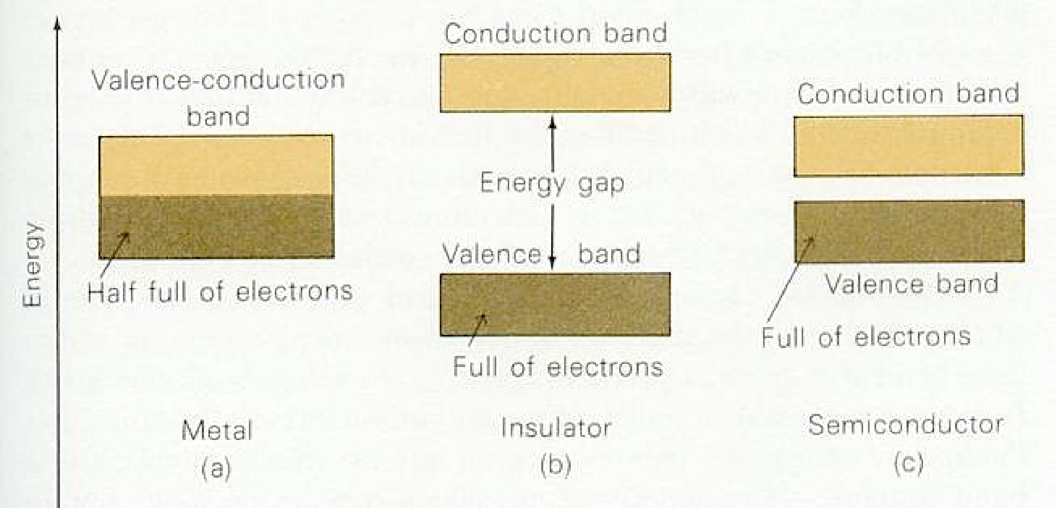

Figure 1.1 Valence and conduction bands of metal, insulator, and semiconductor [5].

1.2.3 Exciton Theory

Exciton theory helps us to understand the electrical and optical properties of semiconductors and particularly of quantum dots. The idea of excitons was first introduced by Frenkel in 1931 and Peierls in 1932 as ‘excitation waves’ when light energy is absorbed and subsequently transformed into heat in solids. Excitons consist of a negatively charged electron and a positively charged hole bound to each other by electrostatic attraction. Excitons exist in all kinds of condensed matter, whenever it is possible for an electron to be excited from valence band to conduction band, leaving behind a hole. This electron hole and the electron are attracted to each other by Coloumb forces creating an electron-hole pair which constitutes a quasi-particle which is mobile within the crystal. Excitons transport energy, not charge or mass. Typically, an exciton is created when a photon is absorbed in a solid; the exciton then moves through the crystal; and finally the electron and hole recombine, resulting in the emission of another photon, often at a wavelength different from that of the original photon [5].

1.2.4 Quantum dots: theoretical description

In the case of the bulk CdSe semiconductor, an electron-hole pair forms a weakly bound exciton. The characteristic distance between these two charges can be expressed as [6]

$$\alpha_{\beta}^{ex} \cong \frac{\hbar^2}{e^2}\left[\frac{1}{m_e}+\frac{1}{m_h}\right] \qquad \text{Equation 1.1}$$

m_e = effective mass of electron

e = elementary charge

m_h = effective mass of hole

ε = dielectric constant of the bulk semiconductor

ħ = reduced Planck Constant

$\alpha^{ex}{}_{B}$ is also known as the Bohr radius of the bulk exciton. For the bulk CdSe semiconductor, $\alpha^{ex}{}_{B}$ is typically about 6 nm.

When the size of the semiconductor crystal is reduced to the Bohr radius or smaller (Eq. 1.1), the exciton will be confined spatially inside the material. This results in quantum confinement, which modifies the electronic and optical properties of the semiconductor. Quantum confinement leads to a collapse of the continuous energy bands of a bulk material into a discreet set of energy levels, similar to single atoms/molecules, as shown in Figure 1.2. The energy states become sharp and the gap larger. The lowest excited state corresponding to the transition $1S_e - 1S_h$ is commonly referred to as the first excitation state. This structure is often referred to an "artificial atom". The properties of the "atom" depend on the size but also the material, through m_e and m_h.

Using the effective mass approximation, Brus showed that for quantum dots the energy gap can be approximately calculated by [6]

$$\Delta E \cong \frac{\hbar^2\pi^2}{2R^2}\left[\frac{1}{m_e}+\frac{1}{m_h}\right]-\frac{1.8e^2}{\varepsilon R} \qquad \text{Equation1.2}$$

m_e = effective mass of electron

m_h = effective mass of hole

e = elementary charge

R = radius of the Quantum dots

ħ = reduced Planck Constant

In Equation 1.2, the first term relates to the quantum localization which shifts the energy gap to higher energies as R squared. The second term is the Coulomb term which shifts the energy to lower energies linearly as function of R. Consequently, the total energy bandgap increases in energy with decreasing quantum dot radius. In common words, one can think that electrons under these "geometrical" constraints respond to changes in particle size by adjusting their energy.

Experimentally, it can be seen that decreasing the size of QDs leads to an increase in energy gap and a consequent shift of their optical absorption and emission wavelength to the blue spectral region [7, 8].

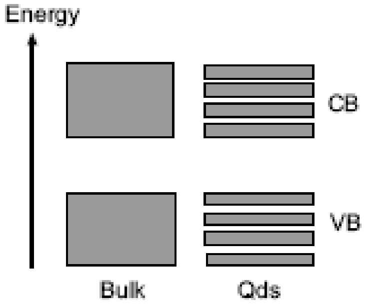

Figure 1.2: A comparison of energy levels between a bulk semiconductor and a quantum dot. The valence and conduction band in a bulk semiconductor consist of an energy continuum. On the contrary, the valence and conduction band in a quantum dot consist of discrete energy levels.

1.2.5 Luminescence process

Photons whose energy is greater than the band gap produce electron-hole pairs, which first decay down to the bottom of the conduction band and to the top of the valence band respectively, forming excitons. For direct gap semiconductors, they subsequently recombine, emitting photons with an energy close to exciton binding energy.

Generally, interactions among electrons, holes, phonons, photons are required to satisfy conservation of energy and crystal momentum. In a nanocrystal, the momentum of the electron-hole pair is not conserved, because they exchange momentum with the boundary of the crystal, so the difference between a direct band gap and indirect band gap is not significant.

1.2.6 Properties of QDs

QDs are usually composed of elements from groups II and VI, e.g, CdSe (most common). The size of a typical QDs is about 2-10 nm (10-50 atoms) in diameter. QDs are fluorophores with a size-tunable emission, strong light absorbance, bright fluorescence, narrow symmetric emission bands, and high photostability. Emission spectra can be quite narrow: from 20 to 40 nm full width at half maximum intensity. The emission wavelength is continuously tunable from the red to the ultraviolet by varying the nanocrystal size, as shown in Figure 1.3.

Figure 1.3 Solutions of different sized Quantum dots.

QDs have a large separation between the excitation and emission spectra (Stokes shift), as shown in Figure 1.4. The fluorescence lifetime (the time the molecules remain in the excited state before emitting a photon) is quite long, about 10-40 ns, which accounts for the stable and strong fluorescence.[8, 9]

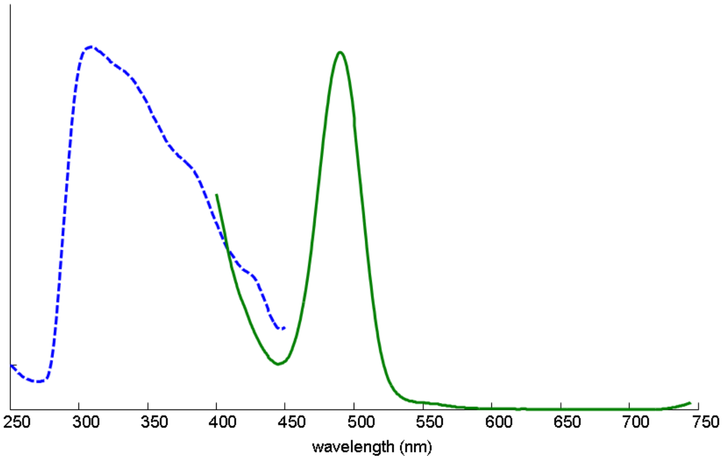

Figure 1.4: Absorption and emission spectra of 490QDs. Y axis is arbitrary units

1.2.7 Applications of Quantum dots

Many industries will profit from the use of quantum dots. The following applications illustrate the many ways that the properties of quantum dots may be exploited [10, 11]:

- Life Sciences
- Displays
- LEDs
- Thermoelectrics
- Photonics & Telecommunications
- Security Inks
- Solar Cells & Photovoltaics

1.2.8 Biological application of Quantum dots

In 1998, Alivisatos reported for the first time the potential of QDs for applications involving biological labelling [10]. They have been demonstrated as suitable for immunolabeling, cell mobility assays, and as live cell markers.[14]. The fact that several QDs can be excited by the same wavelength of light permits the use of these nanocrystals as multi-colour labels.[15] One additional feature of QDs is that they can emit in the infrared and near-infrared regions. This makes them suitable for imaging and diagnostic applications in cells deep within tissues, as the absorption is minimal in this region.[16]. Figure 1.5 is a schematic representation of the range of potential applications of QDs in biological sciences. [10, 11]

Quantum dots are already commercially available and this suggests their use for the above type of applications is increasing. However, very little is currently known about the potential health risks and toxic effect associated with this new material.

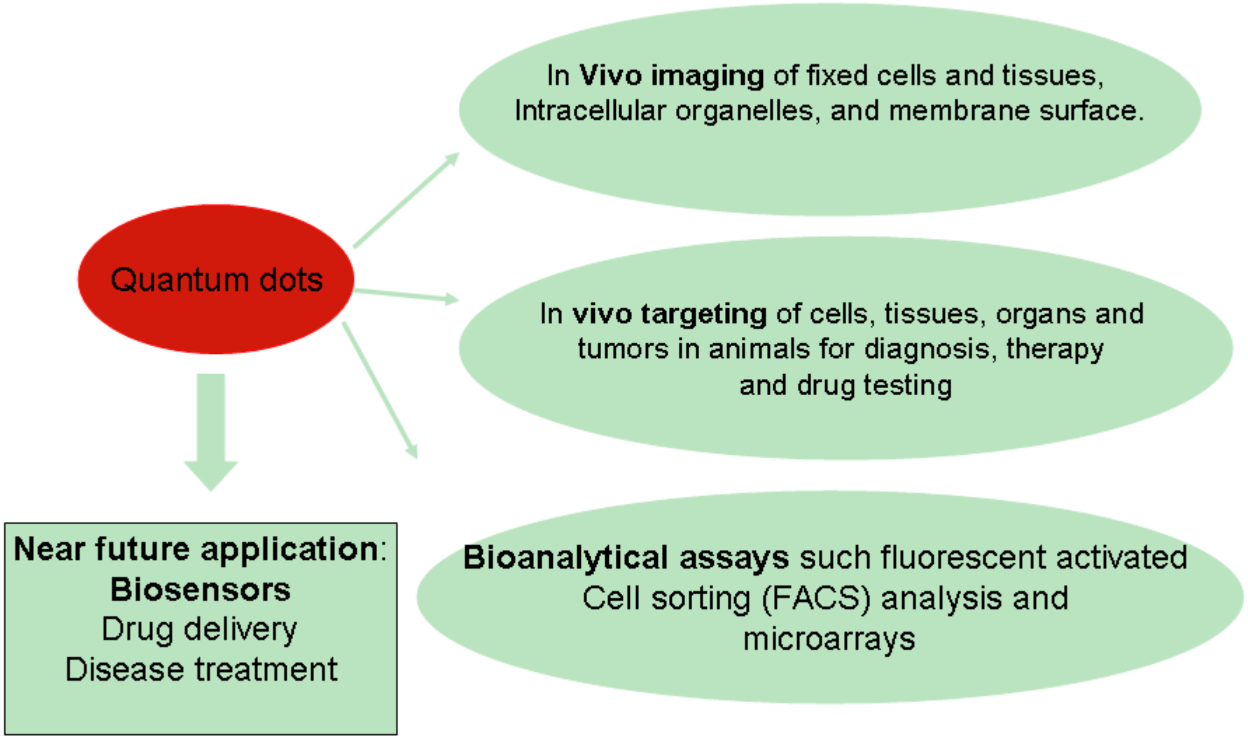

Figure 1.5 Biological applications of Quantum dots

1.3 Toxicology of Quantum Dots

The new field of nanotoxicology leads to novel requirements in terms of risk assessment. The outstanding chemical and physical properties that make nanomaterials so attractive for industrial and medical applications may also lead to unforeseen adverse effects upon environmental and human exposure.

Cadmium and selenium, two of the most widely used constituent metals in QD core metalloid complexes, are known to cause acute toxicity in humans and are of considerable concern for human health. For instance, Cd, a probable carcinogen, has a biological half-life of 15-20 years in humans; bioaccumulate is systemically distributed to all bodily tissues, the liver and kidney being target organs of toxicity.[17]

Ron Hardman [18] carried out a toxicologic review of Quantum Dots. The conclusions of this study are:

1. Not all QDs are alike; engineered QDs cannot be considered a uniform group of substances.
2. toxicity depends on physicochemical properties and environmental conditions; QDs size, charge, concentration, core material, outer coating and functional groups are implicated in QD toxicity.

As part of the current study, a literature review of the known toxic response of QDs was conducted. In this literature review only one class of QDs is considered: CdSe / ZnS core-shell QDs coated with PEG. A summary of the literature review is presented in Tables 1.1, 1.2, 1.3.

1.3.1 *In vitro* studies

In an initial study, Garon at al. [19] showed that QDs can be extremely useful molecular imaging tools for the study of hematologic cells. They demonstrated that dividing cells can be tracked through at least four cells division. Without performing a formal evaluation of cytotoxicity, they observed that proliferation of cells labelled with QDs did not appear different than cells without QDs.

Ryaman-Rasmussen at al. [20] tested two sizes of soluble QDs, QD 565 and QD 655. Both QD 565 and QD 655 were obtained with three different surface coatings: polyethylene glycol (PEG), PEG-amines, carboxylic acids. The study suggested that the surface charge of the QDs, whether cationic or anionic, is an important variable for QD cytotoxicity, with the cationic carboxylic acid-coated QDs showing the highest toxicity response.

In a second study, Ryman-Rasmussen investigated the non selective interaction of primary neonatal human epidermal kerationocytes (NHEK) with the same untargeted QDs used in the previous study [21]. This study showed that untargeted QD can interact with NHEK skin cells and that the variables influencing these interactions are time, QD surface groups, supplements in the culture medium, and temperature.

Blue Knight tested various embryonic kidney cell lines (amphibian, A6 and XLK-WG; human, HEK-293). Results showed that QDs are internalized by all three kidney cell lines and for the human kidney cell line, short-term QD exposure and internalization did not alter membrane integrity or metabolism.

Rouse showed that the application of 10% cyclic strain to HEK caused a significant increased of QD cellular uptake in comparison to QD uptake by HEK that were not exposed to tensile strain [22]. Application of physiological load conditions can increase cell membrane permeability, thereby increasing the concentration of QD in the cells, resulting in irritation and a negative impact on cell viability.

Lin performed the most complete study of the cytotoxicity of QDs [23]. Embryonic stem cells (ES) were labelled with six different QDs (emission at 525, 565, 605, 655,705, 800 nm). In terms of viability, proliferation, and differentiation, no significant difference between labelled and unlabelled cells at 24 hrs, 48 hrs, and 72 hrs was noted.

Muller-Borer tested mesenchymal stem cells with two concentrations of non targeted QDs: 5 and 20 nM. For both concentrations there was no change in proliferation with respect to the control but there was an increase in apoptosis at the highest concentration.

NON-TARGETED QUANTUM-DOTS

Paper	Cell line	QD max emission	Concentration	Exp Time	End points (label/Dye)	Charact. analyzed	Note
Quantum dot labeling of mesenchymal stem cells - B. J Muller-Borer **J of Nanobiotechnology**	mesenchymal stem cells	605 nm	LC= 5 nM HC= 20 nM	24h/72/120h		internalization	QD nanocrystal aggregates in endosomal veiscles around nuclear membrane. Greater number of QD aggregates in the HC vs. LC MSCs at each time point
	mesenchymal stem cells	605 nm	LC= 5 nM HC= 20 nM	24h/120h	Annexin V	Apostosis	Apostosis increased in High Concentration (20 nM/L)
	mesenchymal stem cells	605 nm	LC= 5 nM HC= 20 nM	24 h	Cytokine release	inflammation	The levels of MCP-1 and IL-6 doubled in HC MSCs compared to the LC MSCs and Control MSCs.
	mesenchymal stem cells	605 nm	LC= 5 nM HC= 20 nM	24h/72/120h	CellTiter 96 Aqueous One Solution	proliferation	No change in in MSC metabolic activity as a measure of proliferation.
	mesenchymal stem cells	605 nm	LC= 5 nM HC= 20 nM	24h/72/120h	micro-scale cell-based comet bioassey	DNA damage	The results suggest a trend toward increased DNA damage with increased QD dose. Nevethless, there was no statistically significant difference in comet tail moment measured in LC and HC MSCs compared to Control MSCs
Quantum dot imaging for embryonic stem cells-Shuan Lin - **BMC Biotechnology**	Embryonic stem cells	525, 565, 605, 655, 705, 800 nm	10 nM	24 h	flow cytometry	internalization	Around 72% of the cells were positive 24 hours after labeling and the mean fluorescence intensity (MFI) was 521. After 4 days the percentage of positive cells had dropped to 4%.
		525, 565, 605, 655, 705, 800 nm	10 nM	24/48/72 h	Trypan blue	Viability	no significant difference between unlabeled and labeled ES cells at 24, 48, 72 hrs
	Embryonic stem cells	525, 565, 605, 655, 705, 800 nm	10 nM	24/48/72 hrs	Cyquant cell proliferation	proliferation	no significant difference between unlabeled and labeled ES cells at 24, 48, 72 hrs
	Embryonic stem cells	525, 565, 605, 655, 705, 800 nm	10 nM	24/48/72 h	PCR analysis	differentiation	levels of endoderm(AFP), mesoderm(Flk-1), and ectoderm (Ncam) germ layer markers increased from 0 to day 14 of spontaneous ES cell differentiation using the hanging drop assay.
Cyclic Tensile Strain Icreases interactions between human epidermal keratinocytes and quantum dot nanoparticles- J. Rouse- **Toxicology in Vitro**	hunam epidermial Keratinocytes (HEK)	655 nm	3nM	24h	AlamarBlue and exposed to 10% cyclic strain	Viability	the application of 10% cyclic strain to HEK caused a significant increased of QD cellular uptake in comparison to QD uptake by HEK that were not exposed to tensile strain
						inflammation	Exposure of HEK to QD dose and cyclic strain also showed an increased in IL-8 release compared to media controls.

Table 1.1 Summary of the literature review of QDs toxicity.

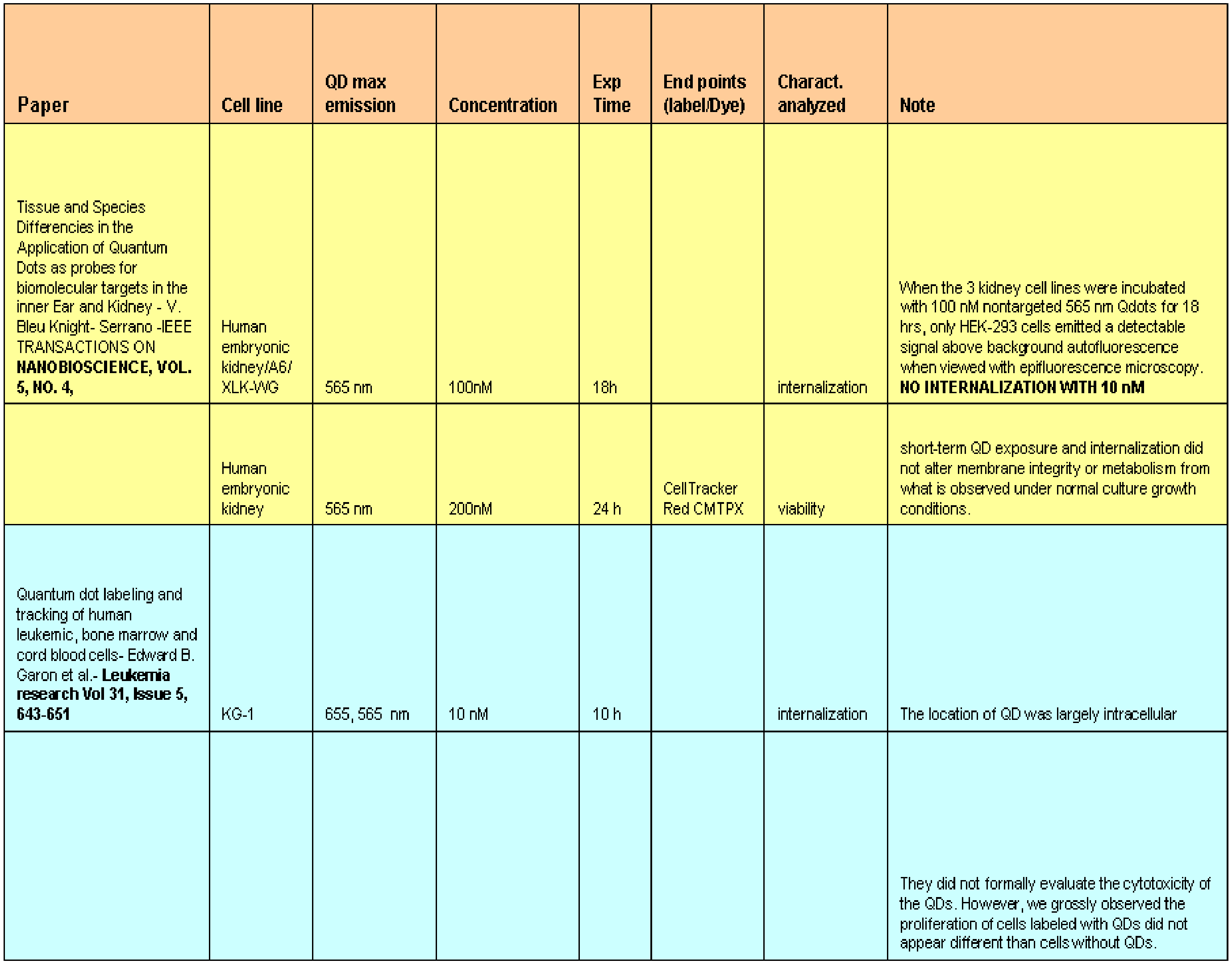

Paper	Cell line	QD max emission	Concentration	Exp Time	End points (label/Dye)	Charact. analyzed	Note
Tissue and Species Differencies in the Application of Quantum Dots as probes for biomolecular targets in the inner Ear and Kidney - V. Bleu Knight- Serrano -IEEE TRANSACTIONS ON **NANOBIOSCIENCE, VOL. 5, NO. 4,**	Human embryonic kidney/A6/ XLK-WG	565 nm	100nM	18h		internalization	When the 3 kidney cell lines were incubated with 100 nM nontargeted 565 nm Qdots for 18 hrs, only HEK-293 cells emitted a detectable signal above background autofluorescence when viewed with epifluorescence microscopy. **NO INTERNALIZATION WITH 10 nM**
	Human embryonic kidney	565 nm	200nM	24 h	CellTracker Red CMTPX	viability	short-term QD exposure and internalization did not alter membrane integrity or metabolism from what is observed under normal culture growth conditions.
Quantum dot labeling and tracking of human leukemic, bone marrow and cord blood cells- Edward B. Garon et al.- **Leukemia research Vol 31, Issue 5, 643-651**	KG-1	655, 565 nm	10 nM	10 h		internalization	The location of QD was largely intracellular
							They did not formally evaluate the cytotoxicity of the QDs. However, we grossly observed the proliferation of cells labeled with QDs did not appear different than cells without QDs.

Table 1.2 Summary of the literature review of QDs toxicity.

Paper	Cell line	QD max emission	Concentration	Exp Time	End points (label/Dye)	Charact. analyzed	Note
Surface Coatings Determine Cytotoxicity and Irritation Potential of Quantum Dot Nanoparticles in Epidermal Keratinocytes -Ryman-Rasmussen et al. - **J of Investigative Dermatology- (2007) 127, 143-153**	Human epidermal keratinocytes HEK	565, 655 nm	2 nM	24 h		internalization	QDs of boths sizes were localized intracellularly by 24 hrs. Punctate staining of QD 565 and QD 655 was observed in the cytoplasm, at the periphery of the nucleus, and in the nucleus (QD 565). NO COLOCALIZATION.
	HEK	565, 655 nm	0.2, 2, 20 nM	48 h	levels of cytokines	inflammation	The cytokines selected for the present study are broad markers for keratinocyte-mediated inflammation. QDs exhibited no increase in cytokine release.
	HEK	565 nm	0.2, 2, 20 nM	24/48 hrs	MTT cell viability	Viability	No differences in HEK viability were observed for three concentrations of PEG-coated QD 565 at 24 or 48 hours.
	HEK	655 nm	0.2, 2, 20 nM	24/48 h	MTT cell viability	Viability	No differences were observed for PEG-coated QD 655 at 24 hours. At 48 hours, however, there was a moderate (20%) but significant decrease in MTT viability at 20 nM compared to vehicle treated controls and lower concentrations.
Variables Influencing Interactions of untargeted Quantum Dot Nanoparticles with Skin Cells and Identification of Biomchemical Modulators-Ryman-Rasmussen et al. - **Nano Letters- 2007 Vol. 7, No. 5 1344-1348**	NHEK- Primary neonatal human epidermal keratinocytes	655 nm	10nM	24 h		internalization	By 2 h, QD 655 were visible on the interior of NHEK, with more visible at 5 h and 24 h.
		655 nm	10nM	24 h	effect of medium		Omitting supplements significantly decreased QD-NHEK interactions. Interaction was 2-fold less in the absence of supplemts thain in a complete medium (KGM-2).
		655 nm	10nM	24 h	effect of temperature		A significant decrease in QD-NHEK interactions at 4 degC and 37 degC was observed. Decreasing the NHEK incubation temperature from 37 to 4 degC was accompanied by a decrease in ATP levels.
		655 nm	10nM	24 h	inhibitors of endocytosis		genistein and nocodazole not attenuated the QD with NHEK. Cytochalasin D potentiated QD-NHEK onteractions for QD

Table 1.3 Summary of the literature review of QDs toxicity.

1.4 Summary and Project outline

From the literature review of the CdSe / ZnS core-shell QDs coated with PEG, it is more than clear that further studies are required. It is still not clear what kind of relationship exists between the shape, size, time of exposure, concentration, and the toxic response.

Due to their optical properties (bright emission), QDs can be used to investigate more generally the interaction of nanoparticles with various biological systems. The biological system interacts primarily with the external coating (PEG) and it may be possible to extend the toxicological results to all kinds of nanparticles with the same coating, shape and size.

A spontaneously immortalized human epithelial keratinocyte cell line (HaCaT) derived from adult skin will be employed throughout this work. HaCaT cells are normal, non-tumourogenic and p53 mutated adult keratinocytes. The cells are polygonal, of approximately 20-µm diameter, producing a 'cobblestone' appearance in culture (Figure 1.6)

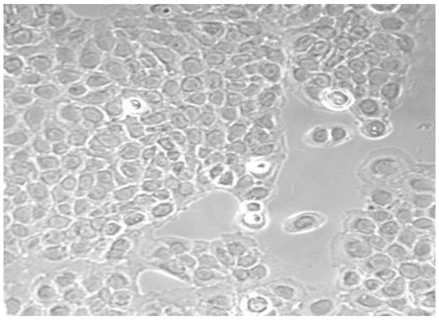

Figure 1.6: HaCaT cells

The starting point of this project will be the characterization of the quantum dots in terms of their dimensions and optical properties.

Classical cytotoxic assays will be used to test the toxicity of the QDs and the results will be compared with similar studies present in the literature.

Finally a range of microscopic and spectroscopic techniques will be employed to examine the localisation of the quantum dots within the cells.

The study will demonstrate the usefulness of QDs to explore and develop methods of detection of nanoparticles in cells.

1.5 References

1. Dingle, R., W. Wiegmann, and C.H. Henry, *Quantum States of Confined Carriers in Very Thin Al_{x}Ga_{1-x}As-GaAs-Al_{x}Ga_{1-x}As Heterostructures.* Physical Review Letters, 1974. 33(14): p. 827.
2. Reed, M.A., *Quantum Dots.* Scientific American, 1993: p. 118-123.
3. Klimov, V.I., *Nanocrystal Quantum Dots - From fundamental photophysics to multicolor lasing.* Los Alamos Science, 2003. 28: p. 214-220.
4. Horan P.G., *Nonlinear optics in quantum confined semiconductor particles* Zeitschrift für Physik D Atoms, Molecules and Clusters, 1989. 12(1-4).
5. *McGraw-Hill Concise Encyclopedia of Physics. 2002.*
6. Bawendi, M.G., *The Quantum Mechanics of Larger Semiconductor Cluster ("Quantum Dots").* Annu. Rev. Phys. Chem., 1990. 41: p. 477-96.
7. Juzenas, P., et al., *Quantum dots and nanoparticles for photodynamic and radiation therapies of cancer.* Advanced Drug Delivery Reviews, 2008. 60(15): p. 1600-1614.
8. Yoffe, A.D., *Semiconductor quantum dots and related systems: electronic, optical, luminescence and related properties of low dimensional systems.* Advances in Physics, 2001. 50(1): p. 1-208.
9. Alivisatos, A.P., W. Gu, and C. Larabell, Annu. Rev. Biomed. Eng., 2005. 7: p. 55.
10. Bruchez, M., Science, 1998. 281: p. 2013.
11. Gao, X., et al., *In vivo molecular and cellular imaging with quantum dots.* Current Opinion in Biotechnology, 2005. 16(1): p. 63-72.
12. www.evidenttech.com.
13. www.invitrogen.com.
14. Michalet, *Quantum dots for live cells, in vivo imaging, and diagnostic.* science, 2005.
15. Gao, X., et al., *In vivo cancer targeting and imaging with semiconductor quantum dots.* Nat Biotechnol, 2004. 22(8): p. 969-76.

16. Azzazy, H.M.E., M.M.H. Mansour, and S.C. Kazmierczak, *From diagnostics to therapy: Prospects of quantum dots.* Clinical Biochemistry, 2007. 40(13-14): p. 917-927.

17. Hardman, R., *A toxicologic review of quantum dots: toxicity depends on physicochemical and environmental factors.* Environ Health Perspect, 2006. 114(2): p. 165 - 172.

18. Garon, E.B., et al., *Quantum dot labeling and tracking of human leukemic, bone marrow and cord blood cells.* Leukemia Research, 2007. 31(5): p. 643-651.

19. Ryman-Rasmussen, J.P., J.E. Riviere, and N.A. Monteiro-Riviere, *Surface Coatings Determine Cytotoxicity and Irritation Potential of Quantum Dot Nanoparticles in Epidermal Keratinocytes.* J Invest Dermatol, 2006. 127(1): p. 143-153.

20. Ryman-Rasmussen, J.P., J.E. Riviere, and N.A. Monteiro-Riviere, *Variables Influencing Interactions of Untargeted Quantum Dot Nanoparticles with Skin Cells and Identification of Biochemical Modulators.* Nano Letters, 2007. 7(5): p. 1344-1348.

21. Rouse, J.G., et al., *Cyclic tensile strain increases interactions between human epidermal keratinocytes and quantum dot nanoparticles.* Toxicology in Vitro, 2008. 22(2): p. 491-497.

22. Lin Wang, D.K.N., Selvapraba Selvarasah, Mehmet R Dokmeci and Rebecca L Carrier, *Toxicity of CdSe Nanoparticles in Caco-2 Cell Cultures.* Journal of Nanobiotechnology, 2008. 6(11).

Chapter 2

Experimental Methods: Characterisation of Semiconductor Quantum Dots

2.1 Evident Quantum Dots

The nanoscrystalline QDs (490QDs and 625QDs) used in this study are commercially available and were purchased from Evident Technology, Troy, N.Y. The core of CdSe and the shell of ZnS are surrounded with polyethylene glycol (PEG). PEG renders the nanoparticles water soluble and biocompatible.[5,6] Figure. 2.1 shows the schematic structure of these water soluble nanoparticles.

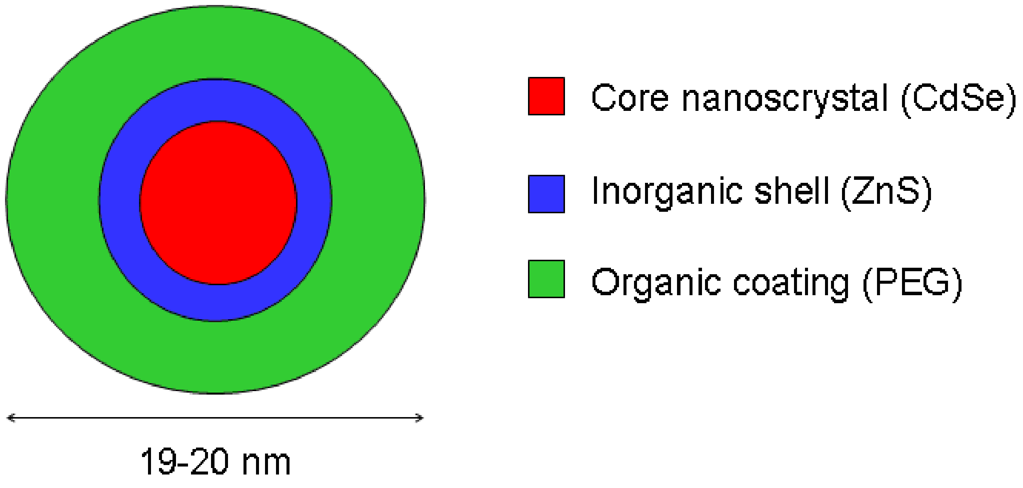

Figure 2.1 Schematic structure of ZnS capped CdSe Quantum dots.

2.1.1 Core – CdSe

The core material that makes up a quantum dot defines its intrinsic energy signature and, as a function of its size, the optical absorption and emission characteristics. When the radius of a QD is smaller than the bulk Bohr exciton radius, it is reasonable to refer to energy levels rather than energy bands as a result of the quantum confinement. Each energy level corresponds to a characteristic feature in the absorption/emission spectrum. For CdSe dots the bulk Bohr excitation radius is 50 Å. [1]

Figure 2.2 shows emission spectra for CdSe quantum dots of different sizes, demonstrating that decreasing the CdSe radius results in increased quantum confinement of the exciton and an increase of the emission energy. [3]

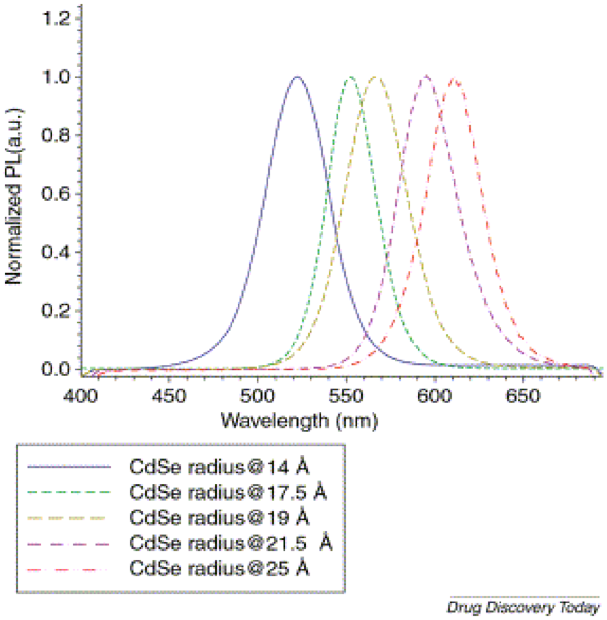

Figure 2.2 Photoluminescence spectra of CdSe-ZnS quantum dots with different core sizes. Quantum dots were excited at 350nm [2]

2.1.2 Shell – ZnS

The surface of quantum dots has both free (unbonded) electrons and crystal defects. Both of these characteristics tend to reduce the luminescence quantum yield (QY) by allowing for nonradiative electron energy transitions at the surface. [4] It is well established that capping a core quantum dot with a shell (several atomic layers of a wide band inorganic semiconductor) reduces nonradiative recombination and results in brighter emission, provided the shell is of a different semiconductor material with a wider bandgap than that of the core semiconductor material. The addition of a shell reduces the opportunities for these nonradiative transitions by giving conduction band electrons an increased probability of directly relaxing to the valence band. The shell also neutralizes the effects of many types of surface defects. [4] Adding one or two layers of ZnS has the further advantage of significantly reducing ambient air oxidation, increasing the stability of the QDs, although it does not fully eliminate photooxidation. [5]

2.1.3 Organic Coating – Polyethylene glycol

In order to use QDs in a biological environment, they need to be water soluble. One strategy to make them hydrophilic is capping them with an organic coating. Polyethylene glycol is a neutral, nontoxic and nonirritating hydrophilic polymer. Derfus et al. showed that successive addition of a layer of PEG, increases the biocompatibility and progressively minimizes the cytotoxicity of CdSe/ZnS QDs. [5] Pishko et al. found that nanoparticles coated with PEG had the lowest percentage of uptake by macrophages when compared to nanoparticles with either negative or positive charges on their surface. The researchers showed that a PEG coating keeps changes in nanoparticle surface to a minimum and therefore protects the nanoparticles from elimination by the immune system. [6]

2.1.4 Commercially available Quantum Dots

Evident Technologies markets QDs as fluorescent cellular probes because they have many advantages such as narrow emission, high brightness and superior photostability over conventional organic fluorochromes. They provide four non-functionalized QDs with various fluorescent emissions: 490QDs, 605QDs, 625QDs, 650QDs. The nomenclature indicates the wavelength of maximum emission. In this study, blue/green QDs (490QDs) are used for the cytotoxicity studies and red ones (625QDs) for the spectroscopy analysis (Figure 2.3).

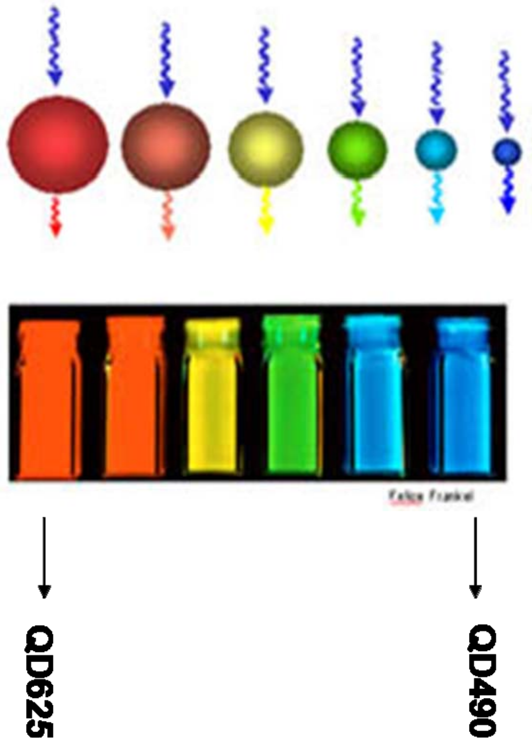

Figure 2.3 Evident Technologies non functionalized CdSe/ZnS with PEG coating QDs. [4]

2.2 Characterization of Quantum dots

2.2.1 Evident Technologies Certificate of Analysis

A certificate of analysis is supplied with the 625QDs. The physical characteristics are presented in the Table 2.1. Unfortunately, a similar certificate was not supplied for 490QDs.

Physical characteristic	
Appearance	Red suspension
Emission Maximum [nm]	627
1st Excitation Peak [nm]	609
Concentration [nmol/ml]	10
Full width at Half Maximum (FWHM) [nm]	34.4
Quantum Yield [%]	62
Reference Dye:	Rhodamine 6G
Volume [ml]	0.2

Table 2.1 625QDs certificate of analysis.

2.2.2 Size

Dynamic light scattering sizing measurements were performed with the aid of a Malvern Instruments Zetasizer Nano Series (purchased from Particular Sciences, UK) operating with version 5.03 of the system's Dispersion Technology Software (DTS Nano). The

Malvern Instruments Zetasizer range uses light scattering techniques to measure hydrodynamic size, zeta potential and molecular weight of proteins and nanoparticles.

The average size of the both QDs, 625QDs and 490QDs, was determined to be 19 nm in diameter, as determined by DLS (Dynamic Light Scattering). A monomodal dispersion was observed in both cases indicating a good dispersion of the QDs with no aggregation.

It is interesting to notice that most of volume of the nanoparticle is due by the PEG coating; the CdSe/ZnS component is approximately 4-6 nm in diameter and in terms of volume is less than 5% of the nanoparticle. As a consequence, it can be assumed that the biological system interacts predominantly with the PEG coating, in the absence of coating degradation.

2.2.3 Optical Properties

The UV/visible absorption characteristics of the materials were determined using a Perkin Elmer Lambda 900 UV/VIS/NIR absorption spectrometer. The spectrometer is a double-beam, double monochromator ratio recording system with pre-aligned tungsten-halogen and deuterium lamps as sources. The wavelength range is from 175 to 3,300 nm with an accuracy of 0.08 nm in the UV-vis region and 0.3 nm in the NIR region. It has a photometric range of ± 6 in absorbance. For all the experimental studies, the absorption was measured at all times with reference to a blank sample in a double beam arrangement, to eliminate variations caused by the difference in lamp intensities at different frequencies.

Absorption and luminescence spectra in nanostructures are associated with optical transitions between electronic states and provide information about the electronic structure of CdSe QDs. In figure 2.4 it can be seen that the absorption spectra of both 490QDs and 625QDs, have a very similar pattern. For the 625QDs, the lowest energy excitonic peak is at ~570 nm, and progressive shoulders appear at 428nm, 389nm, 350 nm and 310nm. It is interesting to note that absorption at 310 nm is significantly more intense than that at 560 nm. In the case of the 490QDs, the lowest energy excitonic absorption peak at ~ 460nm is experimentally obscured by the strong luminescence emission.

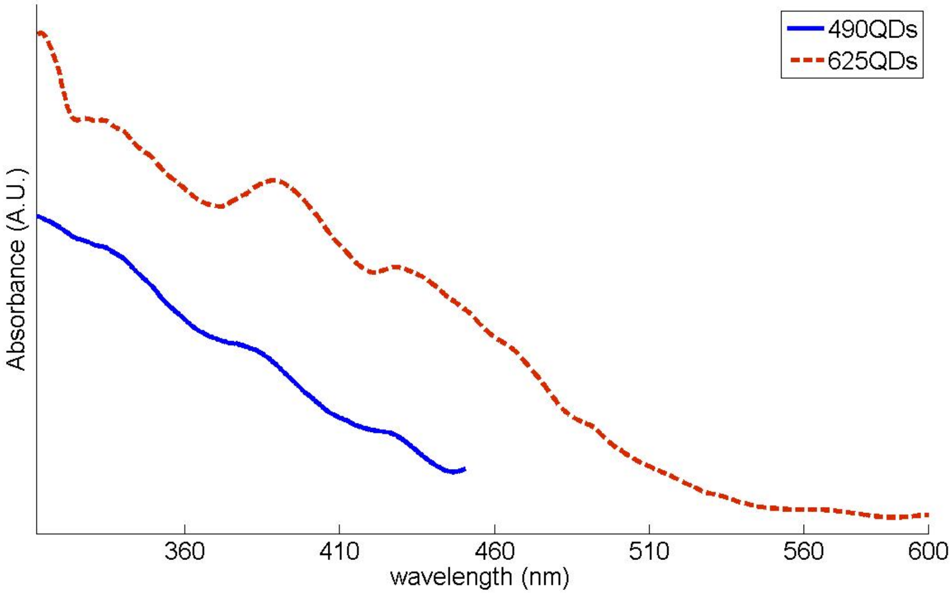

Figure 2.4 Absorption spectra of 490QDs and 625QDs

The emission properties of the QDs were characterised using a Perkin Elmer LS55B Luminescence Spectrometer. The LS55B is a computer controlled luminescence spectrometer with the capability of measuring fluorescence or phosphorescence, as well as a range of other processes including electro-, chemi- and bio-luminescence. Excitation is provided by a pulsed Xenon discharge lamp, of pulse width at half peak height of <10 micro seconds and pulse power 20kW. The source is monochromated using a Monk-Gillieson type monochrometer and can be scanned over the range 200-800nm.

The luminescence is passed through a similar monochromator, which can be scanned over the range 200-900nm. Holographic gratings are incorporated on both monochromators to reduce stray light. Synchronous scanning is available with constant wavelength or frequency difference. Excitation spectra are automatically corrected and sensitivity is specified as a signal to noise ratio of 500:1 rms using the Raman band of water with the excitation at 350nm and 10nm excitation and emission bandpass. The excitation slits (2.5 - 15nm) and the emission slits (2.5 - 20nm) can be varied and selected in 0.1nm increments. In the phosphorescence mode, delay and gate times can be varied with a minimum total period of 13.0msecs. Excitation and emission polarizers consisting of two filter wheels each with horizontal and vertical polarizer elements are also included.

Figure 2.5 shows the emission spectra of the 490QD and 625QD in water solution. The emission spectra are bell-shaped (Gaussian) and have maxima respectively at 489 and 627 nm. The emission characteristics agree well with the manufacturer’s specifications (table 2.1).

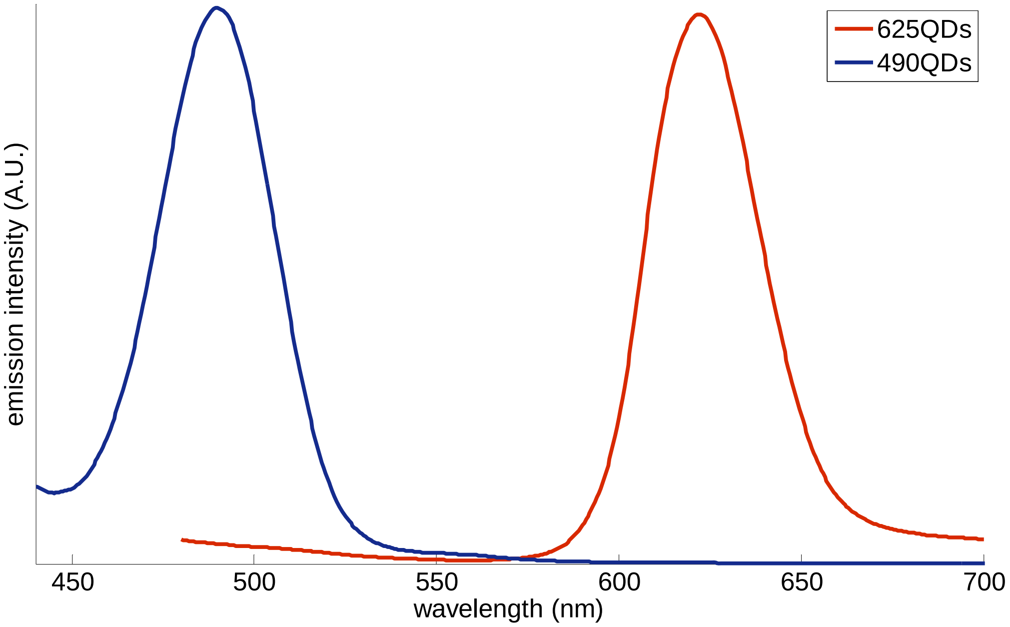

Figure 2.5 Emission spectra of 490QDs and 625QDs .

Figure 2.4 and Figure 2.5 show that 490QDs and 625QDs can be excited by a wide range of excitation wavelengths (310-450 nm) but have narrow, weakly Stokes shifted emission spectra. The Full Width at Half Maximum (FWHM) is ~ 35 nm, again in agreement with manufacturer's specifications.

2.2.4 Vibrational characterisation

Vibrations can be excited by the absorption of electromagnetic radiation at appropriate frequency and analysis of the frequencies where absorption is observed yields information about the identity of the material and the flexibility of its bonds. A material can absorb radiation of frequencies which exactly match the characteristic frequencies of vibration. The characteristic frequencies depend on the forces between the atoms, the mass of the atoms and the bonding geometry. The stronger the forces between the atoms, the higher the vibrational frequency while heavier atoms display lower vibrational frequencies. Traditionally, there are two techniques used to obtain a vibrational spectrum; infrared absorption (IR) and Raman spectroscopy.

2.2.4.1 Infra Red spectroscopy

The IR imaging system employed is a PerkinElmer Spotlight 400 imager (Wellesley, Massachusetts), which consists of a classical Fourier Transform IR spectrophotometer coupled to an infrared microscope. The microscope has a provision to view/focus the specimen using visible light, and a moving stage (moves in xyz directions) on which the specimen can be mounted. Spectra can be accumulated over the range 7800 cm^{-1} to 750 cm^{-1}.

Figure 2.6 shows the FTIR spectrum of the sample of 625QDs. Peak assignments according to Shanmukaraj et al. are given in Table 2.2. Clearly, the spectrum is dominated by the features of the polyethylene glycol coating and there no peaks related with the core/shell (CdSe/ZnS). The peaks related to CdSe and ZnS are probably between 200-300 cm^{-1}, out of the range that can be detected the FTIR imaging system.

Wavenumber [cm^{-1}]	**Assignment**
963 cm^{-1}	CH_2 rocking
1109 cm^{-1}	C-O-C sym stretching
1150-1350 cm^{-1}	CH_2 wagging
1241 cm^{-1}	C-O-C asym stretching
2990 cm^{-1}	CH_2 stretching

Table 2.2 Assignment of FTIR spectrum of 625QDs.

In the Aldrich Library of FT-IR Spectra (Edition I) are presented the spectra of polyethylene glycol (PEG) with two molecular weights: M.W 400 and M.W. 14000.[7]. The two spectra have similar pattern with few differences. The main difference is the presence of an intense and broad peak at 3334 cm^{-1} in the M.W 400 PEG spectrum which is completely absent in the spectrum of M.W. 14000 PEG.

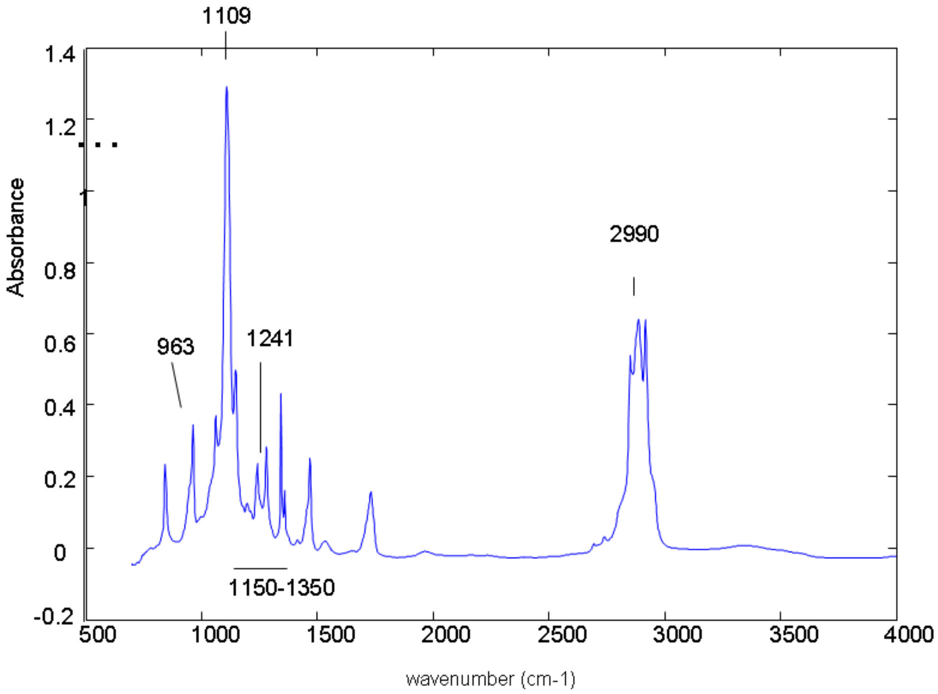

Figure 2.6 FTIR spectrum of 625QDs.

The spectrum presented in Figure 2.6 is very close to the spectrum M.W. 14000. This similarity suggests that molecular weight of the PEG coating of Evident Technology QDs is closer to 14000 than to 400.

2.2.4.2 Raman spectroscopy

Raman spectroscopy similarly provides data about the vibrational states of materials. With a confocal Raman microspectroscope, Raman spectra of a very small measurement volume (less than 1 μm^3) can be measured and therefore the chemical composition of very small structures can be determined.

Raman spectral analysis was performed with a Horiba Jobin Yvon HR800 microspectrometer. The excitation sources used were diode lasers generating single mode lines at 473nm and/or 785 nm. All the measurements were recorded using a 100X water immersion objective (NA=0.9). The nominal spot sizes at the sample were ~ 0.7 (473 nm) and 1 μm (785 nm). A multichannel CCD device was used to detect the Raman Stokes and anti-Stokes signals dispersed by a holographic grating of 600 lines/mm giving approximately 2 cm^{-1} per pixel spectral dispersion. The spectral dispersion is not constant over the spectral range, however. It is about 2.3 cm^{-1} at -6000 cm^{-1} and 1.5 cm^{-1} at 1000 cm^{-1}.

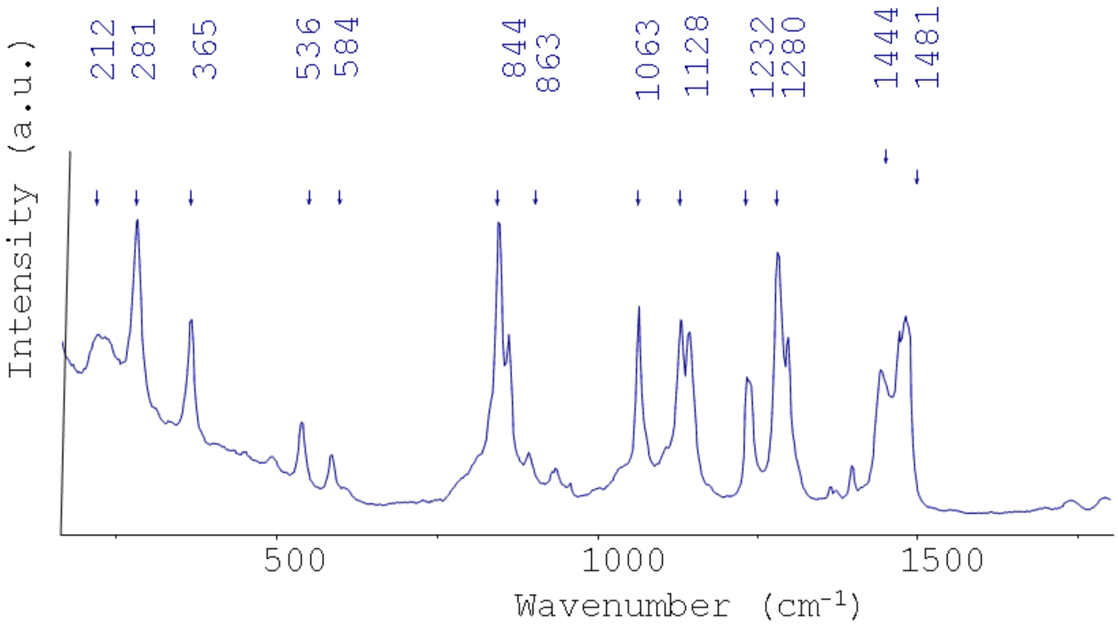

Figure 2.7 Raman spectrum of 490QDs.

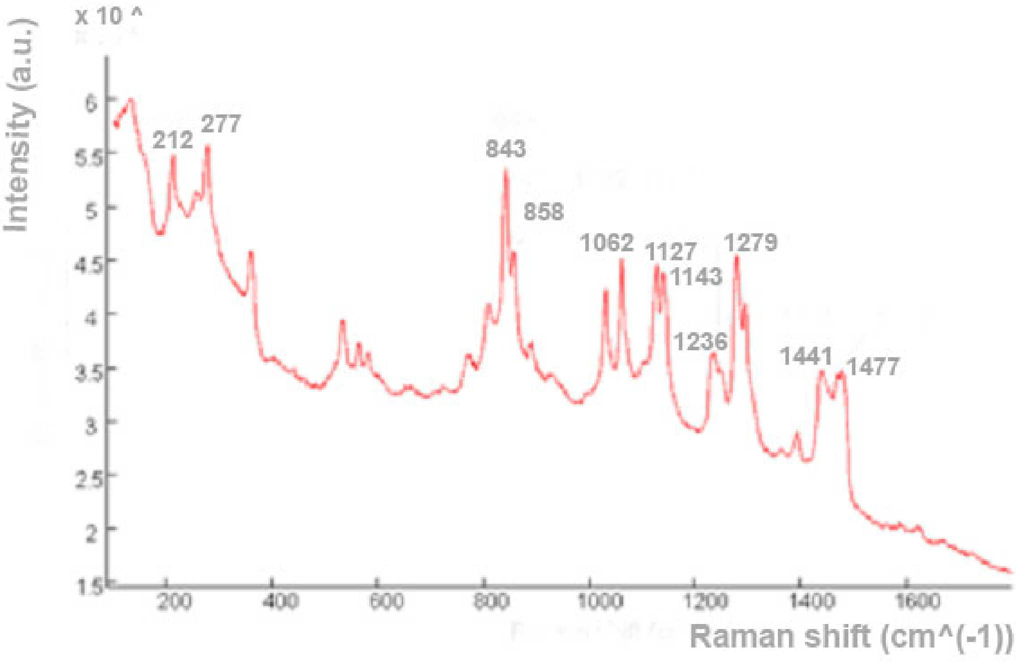

Figure 2.8 Raman spectrum of 625QDs.

Figure 2.7 and Figure 2.8 show the Raman spectra of the QDs in the region of 100-1800 cm^{-1} using a 785 nm diode laser. The two spectra have almost the same features, but in Figure 2.8 we can see an additional peak between 858 and 1062 cm^{-}1. In Table 2.3 the assignment of the bands of 625QD is presented. The peak at 212cm^{-1} is related to longitudinal optical (LO) phonon of the QD core material (CdSe) and the peak at ~277 cm^{-1} is probably related to the longitudinal mode of the ZnSe shell.[8] The rest of the peaks are due to the PEG coating [9].

Raman shift cm[$^{-1}$]	**Assignment**
212	Longitudinal optical (LO) phonon of the QD core material (CdSe)
277	probably related to longitudinal mode of the ZnSe shell
843 and 858	skeleton vibrations
1062	stretching vibrations COH
1127 and 1143	twisting vibrations of CH_2
1236 and 1279	stretching vibrations of C-H
1441 and 1477	stretching vibrations of C-H

Table 2.3 Assignment of Raman spectrum of 625QDs.

FTIR and Raman spectra of the QD samples are dominated by the polyethylene glycol signals. Raman spectroscopy reveals contributions from the core (CdSe) and the shell (ZnS) and at the same time has a significantly higher spatial resolution than the FTIR.

The spatial resolution is intrinsically diffraction limited by the wavelength of the light employed, being < 1 μm in the case of Raman versus ~ 10 μm for FTIR spectroscopy.

2.3 Imaging of QDs

2.3.1 – Confocal Fluorescence imaging

Quantum dots were observed with a confocal laser scanning fluorescence microscopy (Zeiss LSM 510 META, Jena, Germany). The system (figure 2.9) offers 6 excitation wavelengths (458nm**,** 477nm**,** 488nm**,** 514nm, 543nm and 633nm) and for detection, three separate reflected light PMTs, each with its own adjustable pinhole and emission filter wheel.

Figure 2.9: Confocal laser scanning microscope (Zeiss LSM 510 META).

Confocal Fluorescence Microscopy was initially tested as a probe to detect the 490QDs fluorescence emission. 490QDs in water solution were deposited on a quartz slide and left to dry completely and then exposed to different excitation wavelengths. QDs dried in a circular and almost uniform layer on the quartz slide. In the optical image in figure 2.10, the presence of the dry 490QDs on the left side and a clear border between the dry layer and the quartz on its own can be seen. As expected from the 490QDs absorption spectrum (Figure 2.4), the presence of 490QDs using 458 nm, 477 nm and even 488 nm excitation wavelengths was detected, but not with 514 nm, at which wavelength the sample is not resonant. The readily detectible fluorescence signal promises ease of detection of the QDs internalised within cells, as will be demonstrated in chapter 3.

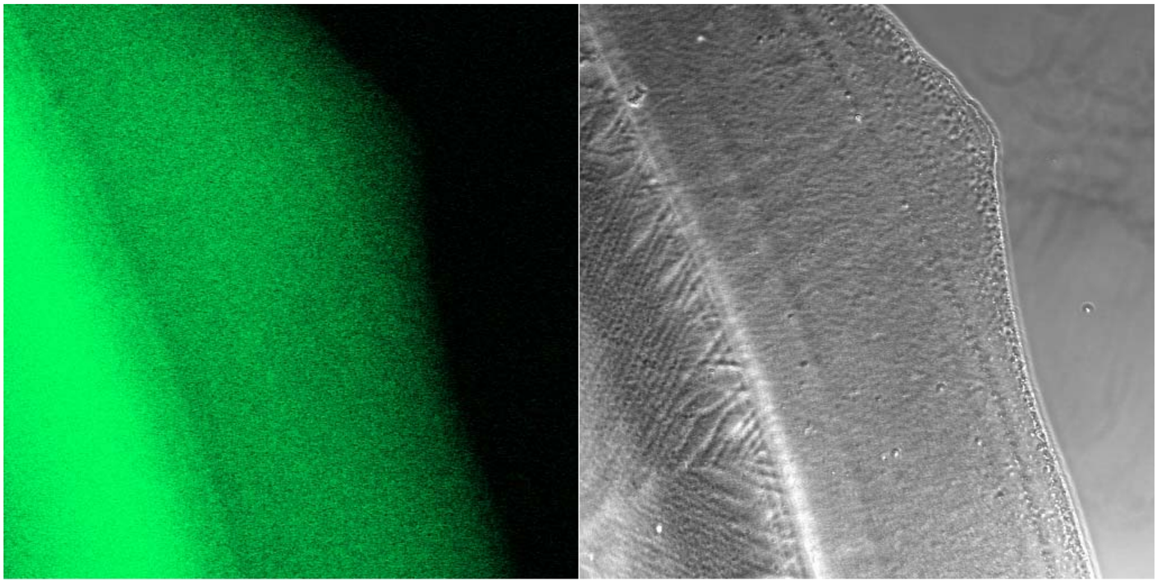

Figure 2.10 Optical and Confocal Fluorescence images of 490QDs on a quartz slide (excitation wavelength = 458nm).

2.3.2 – Raman imaging

The Raman microspectroscope can similarly be used to detect and image the fluorescence from the QDs, provided the excitation wavelength is resonant with the material absorption. In this case, an Instruments SA (Jobin-Yvon) Labram 1B, was employed. It is similar in design to the Horiba Jobin-Yvon HR800, having 514.5nm or 633nm (Argon ion and Helium Neon lasers) as sources, and a choice of 1800 lines/mm or 600 lines/mm gratings.

Figure 2.11 shows the spectrum of a dried sample of 625QD on quartz using the 514.5 nm laser as excitation source. It is dominated by the photoluminescence emission and, as expected, has the same shape and FWHM (~35 nm) as that measured with the luminescence spectrometer (figure 2.5). It is interesting to note, however, that the peak wavelength has shifted from 627 nm to 632 nm. This difference can be explained considering that the QDs were in a solution for the experiment with the luminescence spectrometer and in the solid state for Raman analysis; the aggregation of nanoparticles could induces a redshift of the peak emission. This result could potentially be used to identify and localise high concentrations of QDs in a biological sample.

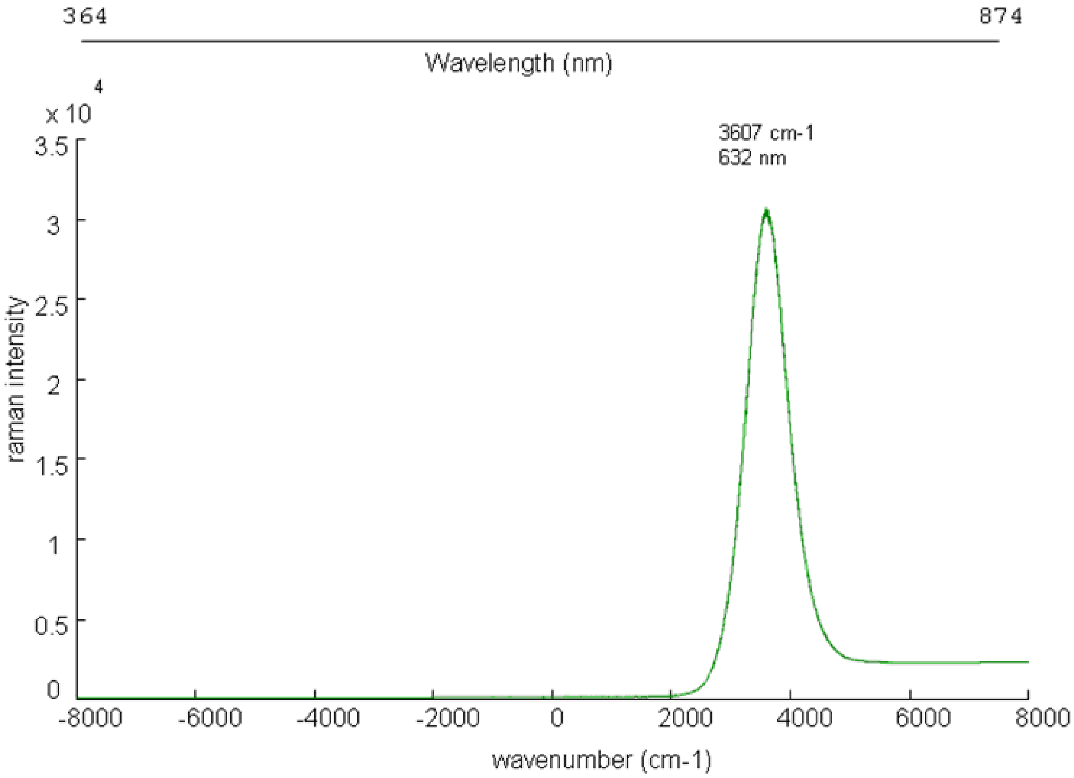

Figure 2.11 Raman spectrum of 625QDs in the range from -8000 to 8000 cm^{-1}.

2.3.3 Two Photon Excitation Fluorescence (TPEF) in Raman spectra

Using 785nm excitation, away from the absorbance of either QD, it would be expected that the Raman spectrum should be free of the strong optical emission. Figures 2.11 and 2.12 show a very broad Raman spectrum of QDs (from -8000 to 8000 cm^{-1}) for both 490QDs and 625QDs. In both cases, the luminescent emission observable from one photon excitation continues to dominate the spectrum. In figure 2.12, for example, the broad features at -7044 cm^{-1} corresponds to a wavelength of 506 nm. The aggregation of 490QDs red shifts the emission from 490 nm to 506 nm and generates a second weak band at 557 nm. The superimposed structure of narrow intense peaks is due to the transmission characteristics of the dielectric edge filter present in the Raman spectrometer.

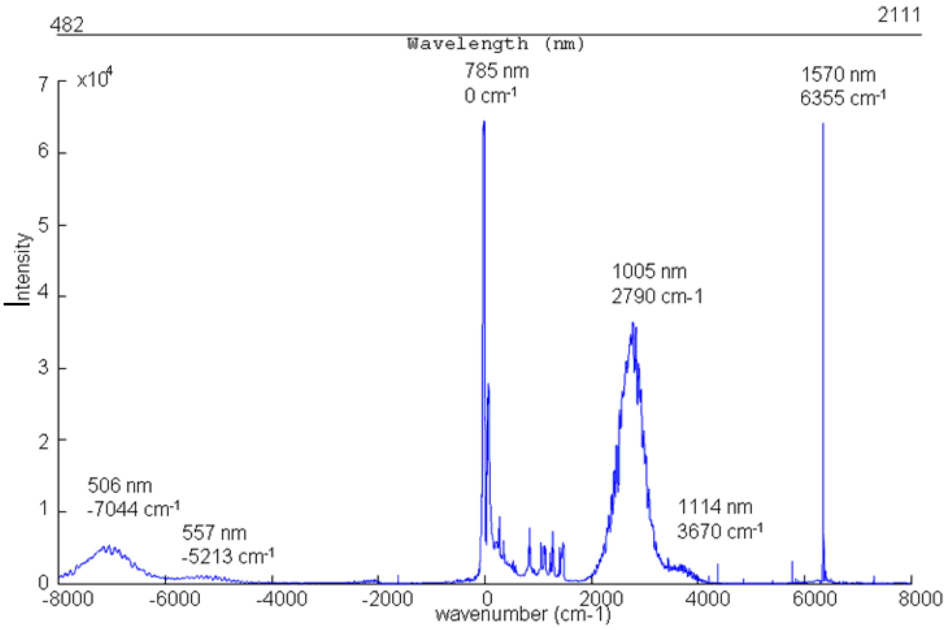

Figure. 2.12 Raman spectrum of 490QDs in the range from -8000 to 8000 cm^{-1}.

The peaks at 2790 cm^{-1} (1005nm) and 3670 cm^{-1} (1114nm) are the second order diffraction features. It is interesting to notice that the second order diffraction peak for 490QDs is more or less 8 times more intense than the corresponding first order peak, although the second order diffraction peak should be less intense than the first order peak. This is due to the fact that the dielectric edge filter of the Raman spectrometer has only ~ 5% transmission in this region.

Notably, the Raman spectrum of the quantum dots (figure 2.12) is also visible in the region 200cm^{-1} – 2000cm^{-1}. This observation promises combined mapping of the Raman and photoluminescence of the QDs.

A similar behaviour is observed for 625QDs as shown in figure 2.13. Although 785nm is used as source, the QD emission at 616nm as well as the second order is clearly visible. Again, the Raman spectrum is simultaneously visible between 200cm^{-1} and 2000cm^{-1}.

2.3.4 Two Photon Excitation Fluorescence (TFEF): Theory

The concept of two-photon excitation is based on the idea that two photons of energy less than the bandgap, co-incident on a material, combine to excite a fluorophore. Any combination of photons of different energies that sum up to give the energy difference between the ground state and the excited state will suffice.

The probability of the near-simultaneous absorption of two or more photons is extremely low, but by concentrating photons both temporally and spatially, the probability of multiphoton absorption is greatly increased. Furthermore, the two-photon requirement for fluorescence excitation implies that the generated fluorescence will depend on the square of the number of photons per unit time and area, the intensity squared (the reason this phenomenon is called “nonlinear”). [10]

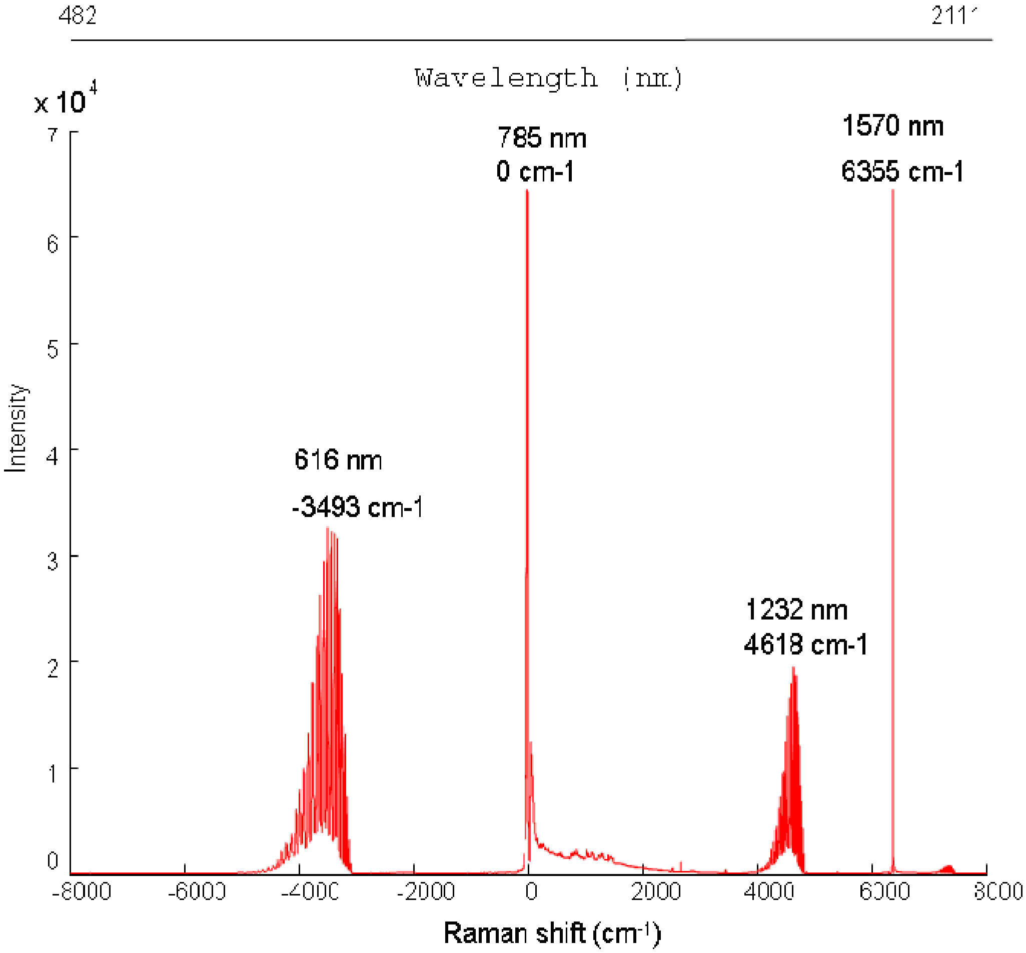

Figure 2.13 Raman spectrum of 625QDs in the range from -8000 to 8000 cm^{-1}.

In order to demonstrate that the broad peak in the anti-Stokes side of the Raman spectrum is due to a Two-Photon excitation process, the spectrum recorded by the Raman spectrometer was measured using 4 different excitation powers.

The Raman spectrometer is provided with multiple neutral density filters that permit variation of the incident light levels. 10%, 25%, 50% and 100% of the beam power for the same acquisition time of 90 sec was employed. Table 3 shows the maximum intensity of the 625QDs fluorescence peak in the anti-Stokes side as a function of intensity.

BEAM %	**Raman intensity**		
INT in	**INT out**	**ln(INT in)**	**ln(INT out)**
10	678.585	2.302585	6.52001
25	2938.24	3.218876	7.985566
50	12614.8	3.912023	9.442626
100	53077	4.60517	10.8795

Table 2.3 Raman intensity in function of the percentage of beam power and corresponding logarithmic values.

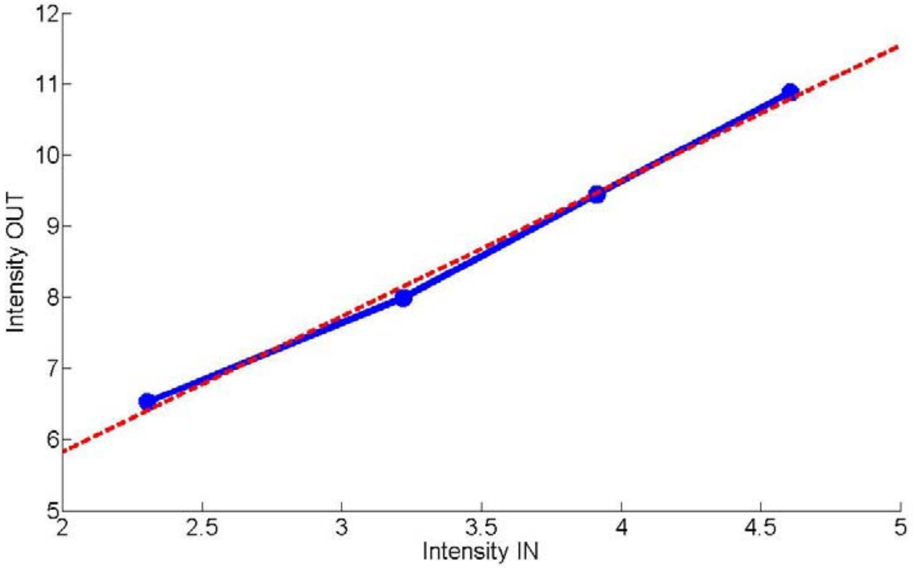

Figure 2.14 Plot of the intensity OUT Vs the intensity IN in logarithmic scale.

Figure 2.14 shows a plot of the luminescent intensity I_{out} versus the incident intensity, I_{in}. The best fit slope of 1.903 in this logarithmic representation is indicative of a quadratic dependence of the emission intensity with respect to the excitation intensity, characteristic of a two photon excitation process.

A second experiment was performed, varying the excitation intensity and the time of acquisition and then comparing the intensity response as measured by the Raman spectrometer. The spectrum with acquisition time of 22.5 sec using an intensity of 100% has almost the same intensity values as the spectrum with acquisition time 90 sec and 50% intensity, as shown in figure 2.15. This result provides further confirmation of Raman intensity's quadratic response respect to the excitation intensity.

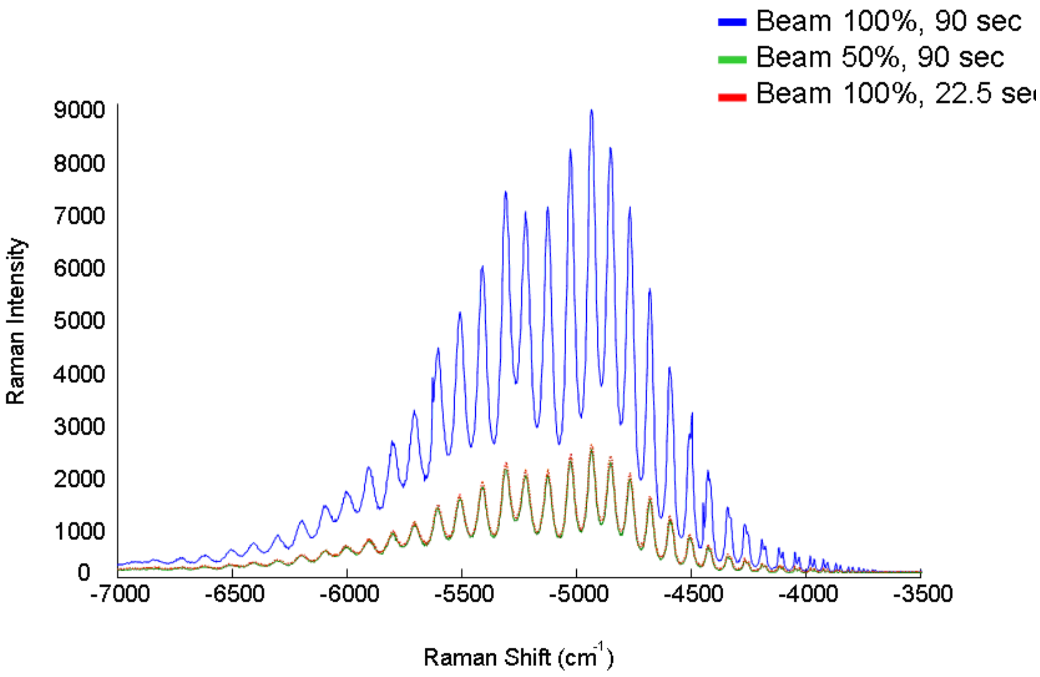

Figure 2.15 QDs Fluorescence emission in function of time of acquisition and intensity of beam.

As a probe, two photon fluorescence has intrinsically higher spatial resolution than single photon fluorescence[10]. In the case of the single photon excitation it can be assumed that the spatial resolution (X-Y) depends on the diffraction-limited laser focal point. [11]

$R= (1.22\ \lambda/ NA)/2$ Equation 2.1

where NA is the numerical aperture of the objective. For a microscope objective of

NA=0.9, R= 0.532 µm at a wavelength of 785nm and 0.321 µm at a wavelength of 473nm.

In the z-direction, the depth resolution is limited by the depth of focus:

Depth of focus = $4 \lambda \backslash (NA)^2$ Equation 2.2

Depth resolution is half of the depth of focus and thus for a wavelength of 785 nm the depth resolution is 1.939 µm while for 473nm it is 1.168 µm.

As shown above the spatial and depth resolutions are both a function of the laser wavelength (λ) and the Numerical Aperture (NA), and thus reducing the laser wavelength yields better spatial resolution.

Two-photon excitation fluorescence (TPEF) is a nonlinear phenomenon: the two-photon requirement for fluorescence excitation implies that the generated fluorescence will depend on the square of the number of photons per unit time and area, the intensity squared. As a result of focusing the beam, the intensity along the optical axis increases at the focus and decreases as the distance squared, so that 2PEF increases and then diminishes as the distance raised to the fourth power, confining 2PEF to the immediate vicinity of the focal point. [10]

In a mathematical form this can be expressed in the following way:

I_{in} α 1/ d^2 Equation 2.3

I_{out} α $(Iin)^2$ Equation 2.4

therefore

I_{out} α 1/d^4 Equation 2.5

I_{in} = intensity of the laser

I_{out} = intensity of the TPEF

d = distance from the focal plan in the optical axis (z)

Therefore the spatial resolution due to two photon excitation fluorescence should not be limited by the diffraction limit.

Figure 2.16 clearly demonstrates this phenomenon for the case of a fluorescein solution. For identical microscope objectives and incident powers, the single photon emission profile (330nm) traces the focal profile of the objective, whereas the TPEF profile is limited to the focal point.

Figure 2.16 SPEF and TFEF of fluorescein. [12]

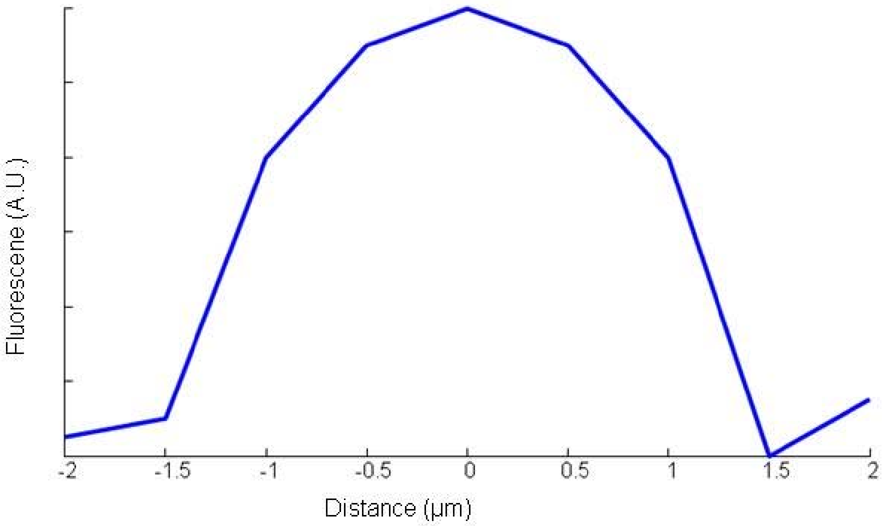

Figure 2.17 Z-profile of the 2PEF of 625QDs. Parameters: ex: 785 nm, 15 sec X 2, -2 to 2 µm, Z increment 0.5 µm.

Figure 2.17 shows the Z-profile of the 2PEF of 625QDs with an increment of 0.5 µm. At position 0 the maximum intensity of the fluorescence of the QDs is observed. The FWHM is 1.1 µm and it can be used as an estimation of the depth resolution. Assuming there is a cluster of QDs in the zero position it should be possible to localise the QDs with a resolution of 1.1 µm, a significant improvement compared to the single photon depth resolution (1.939 µm).

The Raman spectrometer can therefore be used to locate the QDs within the cells via their fluorescent emission. The QDs also have a characteristic Raman spectrum which can be used to identify them, and also to identify their local environment within a cell, giving an indication of the internalisation and transport mechanisms.

Raman spectroscopy has also been extensively used to identify physiological changes to cells and tissue due to disease, fixation and nanotoxicants.[13,14,15] Thus the combination of techniques promises an overall profiling of the interaction of nanoparticles with cellular material.

2.4 Summary

Starting with identifying the relevant information about the commercially available QDs used in this study, the present chapter analyzed the physical (size and material composition) and optical properties of the QDs employed. Particle size and optical properties agree well with manufacturers specifications. It was noted that the particle size is dominated by the PEG coating of the QDs rather than the core material.

The vibrational properties in both IR and Raman spectroscopy are similarly dominated by those of the PEG coating, although the Raman spectrum does show some features assigned to the CdSe core and the ZnS shell. Raman also affords significantly higher spatial resolution and can simultaneously record the vibrational spectrum and the emission spectrum via TPEF. Thus it is the method of choice for probing the interaction of QDs with biological cells.

2.5 References

1. Yoffe, A.D., *Semiconductor quantum dots and related systems: electronic, optical, luminescence and related properties of low dimensional systems.* Advances in Physics, 2001. 50(1): p. 1-208.

2. Hedi, M., et al., *Electroluminescence from heterostructures of poly(phenylene vinylene) and inorganic CdSe nanocrystals.* Journal of Applied Physics, 1998. 83(12): p. 7965-7974.

3. Dabboussi, *(CdSe)ZnS Core-Shell Quantum Dots: Synthesis and Characterization of a Size Series of Highly Luminescent Nanocrystallites.* J. Phys. Chem. B 1997, 1997. 101: p. 9463-9475.

4. www.evidenttech.com.

5. Derfus, A.M., W.C.W. Chan, and S.N. Bhatia, Adv. Mater., 2004. 16: p. 961.

6. Zahr, A.S., C.A. Davis, and M.V. Pishko, *Macrophage Uptake of Coreâˆ'Shell Nanoparticles Surface Modified with Poly(ethylene glycol).* Langmuir, 2006. 22(19): p. 8178-8185.

7. Pouchert, C.J., *The Aldrich Library of FT-IR spectra* Edition I. 2.

8. Liu Lu, X.-L.X., Wen-Tao Liang and Hai-Fei Lu, *Raman analysis of CdSe/CdS core–shell quantum dots with different CdS shell thickness.* JOURNAL OF PHYSICS: CONDENSED MATTER, 2007.

9. Kozielskia, M., *The Raman scattering study of selected polyoxyethyleneglycols.* Journal of Molecular Liquids 111 () 1–5, 2004. 111(1-5).

10. Oheim, M., et al., *Principles of two-photon excitation fluorescence microscopy and other nonlinear imaging approaches.* Advanced Drug Delivery Reviews, 2006. 58(7): p. 788-808.

11. Everall, N.J., *Modeling and Measuring the Effect of Refraction on the Depth Resolution of Confocal Raman Microscopy.* Applied Spectroscopy, 2000. 54(6): p. 773-782.

12. *[Online] Available* http://belfield.cos.ucf.edu/one%20vs%20two-photon%20excitation.html*, July 21,2009.*

13. Meade AD, Clarke C., Draux F, Sockalingum GD, Manfait M, Lyng FM, Byrne HJ, *Studies of chemical fixation effects in human cell lines using Raman microspectroscopy.* Anal Bioanal Chem., 2010.

14. Peter Knief, Colin Clarke, Eva Herzog, Maria Davoren, Fiona M. Lyng, Aidan D. Meade and Hugh J. Byrne, *Raman spectroscopy - a potential platform for the rapid measurement of carbon nanotube-induced cytotoxicity*. The Analyst, 134, 1182-1191 (2009).

15. Fiona Lyng, PhD, Eoghan Ó Faoláin, Jennifer Conroy, Aidan Meade, Peter Knief, Brendan Duffy, Mary Hunter, Joe Byrne, Peter Kelehan, Hugh J Byrne, *Vibrational Spectroscopy for Pathology, from biochemical analysis to diagnostic tool*. Experimental and Molecular Pathology, 82, 121-129 (2007).

Chapter 3

Interaction of QDs with cells

3.1 Introduction

The biological interactions of nanoparticles, both at the tissue and cellular levels, are dictated by the unique physiochemical properties inherent in nano-sized structures. The objective of this study is to investigate the mechanisms of interaction between nanoparticles and the biological environment using different techniques: cytotoxicty assays, confocal microscopy and vibrational spectroscopy. The combination of techniques permits visualisation and understanding of different aspects of the mechanism of interactions. A key point of this study was to connect the information gleaned from these techniques and reach a more broad vision of the issue.

3.2 Materials and Methods

3.2.1 Cell culture

A spontaneously immortalized human epithelial keratinocyte cell line (HaCaT) derived from adult skin was used throughout this work. The cells are normal, non-tumorigenic and p53 mutated adult keratinocytes. The cells are polygonal, approximately 20-μm diameter, and produce a 'cobblestone' appearance when confluent. [1]

HaCaT cells were grown in Dubeccos's modified minimum essential medium (DMEM, Cambrex). All media were supplemented with 10% foetal bovine serum (FBS) and 45 IU/ml penicillin and 45 μg/ml streptomycin and cells were maintained at 37 C in a 5% CO_2 humidified incubator.

3.2.2 Quantitative cytotoxicity assessments

For cytotoxicity assays, cells were seeded in 96-well microplates (Nunc, Denmark) at a density of 1 x 10^5, 7 x 10^4, 3 x 10^4 and 2 x 10^4 cells/ml in Dubeccos's modified minimum essential medium (DMEM, Cambrex) for 24, 48, 72 and 96 h studies, respectively. These seeding densities were found to be optimal to achieve 80% confluency at the end of each respective exposure period. After 24 h of cell attachment, plates were washed with 100 μl/well phosphate buffered saline (PBS) and the cells were treated with increasing concentrations of QDs. All media were supplemented with 10% foetal bovine serum (FBS) and 45 IU/ml penicillin and 45 μg/ml streptomycin and cells were maintained at 37°C in a 5% CO_2 humidified incubator. Three replicate wells were used for each control and test concentration per microplate. Cytotoxicity was assessed using three assays as outlined below.

3.2.2.1 Alamar Blue and Neutral Red assays

The Alamar Blue (AB) and Neutral Red (NR) assays were conducted consecutively on the same set of plates. The AB assay was performed first. The bioassay was carried out according to manufacturer's instructions. Briefly, control media or test exposures were removed; the cells were rinsed with PBS and 100 µl of an AB/NR medium (5% [v/v] solution of AB and 1.25% [v/v] of NR dye) prepared in fresh media (without FBS or supplements) were added to each well. Following 3 h incubation, AB fluorescence was quantified at the respective excitation and emission wavelength of 540 and 595 nm using a microplate reader (Tecan GENios, Grödig, Austria). Wells containing medium and AB without cells were used as blanks. The mean fluorescent units for the 3 replicate cultures were calculated for each exposure treatment and the mean blank value was subtracted from these. Viability and protein determination of the cells following exposure to each chemical were then subsequently investigated using the NR.

3.2.2.2 MTT assay

The MTT assay is a standard laboratory test and standard colorimetric assay for measuring of viable cells.

The plates for the MTT assay were seeded and exposed identically to the first series of plates prepared for the AB, NR. 10 µl of MTT (5mg/ml) prepared in PBS were then added to each well and the plates were incubated for 3 h at 37^{o}C in a 5% CO_2 humidified incubator. After this incubation period the medium was discarded, the cells were washed with 100 µl of PBS and 100 µl of DMSO were added to each well to extract the dye. The plates were shaken at 240 rpm for 10 min and the absorbances were measured at 570 nm using a microplate reader (Tecan GENios, Grodig, Austria).

3.2.3 Phototoxicity

The Q-sun solar spectrum simulating irradiator (Q-Panel, Cleveland, USA) is a solar simulator whose spectral output mimics that of natural sunlight reasonably well and it offers a unique opportunity to assess the effect of sunlight on human keratinocytes.

Figure 3.1 Q-Sun xenon solar simulator test chamber

3.2.3.1 Methodology of QDs Phototoxicity assay

The protocol for the assessment of the phototoxicity of QDs was as follows:

- HaCaT cells were seeded in two 96 well plates (10,000 /well). [day 1]
- HaCaT cells were exposed to QDs625 for 1 hr (20, 2, 0.2 nM and control). [day 2]
- QDs+medium were replaced with 200 µl PBS.
- One 96 well plate was exposed to solar light for 30 min.
- PBS was replaced with cell culture medium
- HaCaT cells were incubated at 37º C and 5% CO_2 for 24 hrs
- The MTT assay was conducted [day 3]

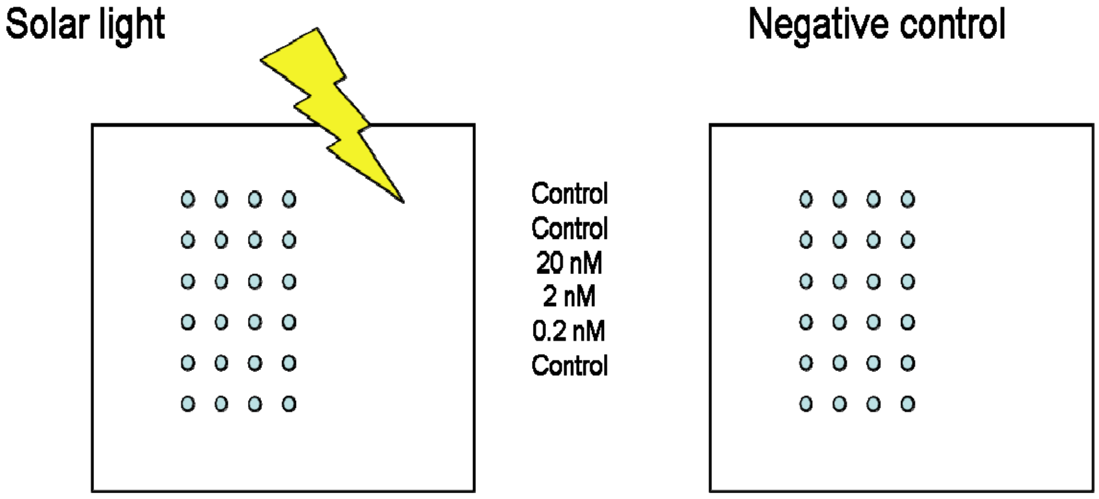

Figure 3.2 Schematic of Phototoxicity assay.

Prior to exposure, it is important to replace the medium with PBS because it has been demonstrated that absorption by the cell culture medium can modify the effective spectrum of the Q-sun. [3] Moreover, the cell culture medium can itself photodegrade and significantly contribute to cell death. PBS is however transparent in the spectral region of interest and does not photodegrade.

3.2.4 Confocal Microscopy

The Zeiss LSM 510 META, (Jena, Germany) (section 2.3.1.1) Confocal Fluorescence microscope was employed as a probe of the QDs within the cells. Evident Technologies 490QDs and 620QDs were used as supplied. HaCaT cells were incubated with 20 nM QDs solution for 1-2 hours and then washed in PBS to remove excess QDs. Finally 3ml saline solution was added.

Lysotracker probes are fluorescent acidotropic probes for labelling and tracking acidic organelles in live cells. Lysotracker (511 nm fluorescence peak emission) was purchased from Invitrogen**,** Carlsbad**,** CA . [2]

Cell were incubated with 60 nM Lysotracker solution for 2 hours and then washed three times in PBS and finally 3 ml of saline was added to the Petri dish. To examine co-localization of the QDs with the lysotracker, HaCaT cell were incubated first with the QDs for 1 hour and then with the Lysotracker for 2 hours. Finally images were taken using the 458nm line of the argon laser to excite the QDs and 488 nm line to excite the Lysotracker.

3.2.5 Statistics

For the cytotoxicity assays, fluorescence as fluorescent units (FU), luminescence as relative light units (RLU) and absorbance were all quantified using a microplate reader (TECAN GENios, Grödig, Austria). Experiments were conducted in at least triplicate (three independent experiments). Test treatments for each assay (AB, NR, MTT) were expressed as percentage of the unexposed control ± standard deviation (SD). Control values were set at 100%.

3.2.6 Raman mapping of HaCaT cells

HaCaT cells were loaded at a concentration of 6 X 10^4 per quartz substrate and, after 24 hours, QDs probe solution was added to the cells at the final QDs concentration of 20 nM for 1-2 hours and then washed to remove excess QDs. Finally, the cells were fixed in 4% formalin in PBS for Raman analysis.

For Raman spectral imaging, isolated single cells were scanned with a 1 µm step (ex = 785 nm) and with 0.5 µm step (ex = 473 nm). Table 3.1 shows the parameters used for these Raman acquisitions.

	Parameters A	Parameters B
Laser Line	*785 nm*	*473 nm*
Binning Factor	*2*	*1*
Filter	*100%*	*50%*
Number of Accumulations	*1*	*2*
Increments	*1 µm*	*0.5 µm*
Range and Time of acquisition	*400-1800 cm^{-1}: 45 sec* *-8000 to -5000 cm^{-1}: 45 sec*	*600-1800 cm^{-1} : 1.5 sec* *2500-400 cm^{-1} : 0.3 sec* *4500-5800 cm^{-1} : 0.3 sec*

Table 3.1 Raman mapping parameters.

3.2.7 Hybrid Confocal Raman Fluorescence

Section 2.3 demonstrated how hybrid confocal Raman fluorescence microscopy (Figure 3.3) can detect the presence of the quantum dots and at the meantime determine information from the cell in the finger print region (400 -1800 cm^{-1}).

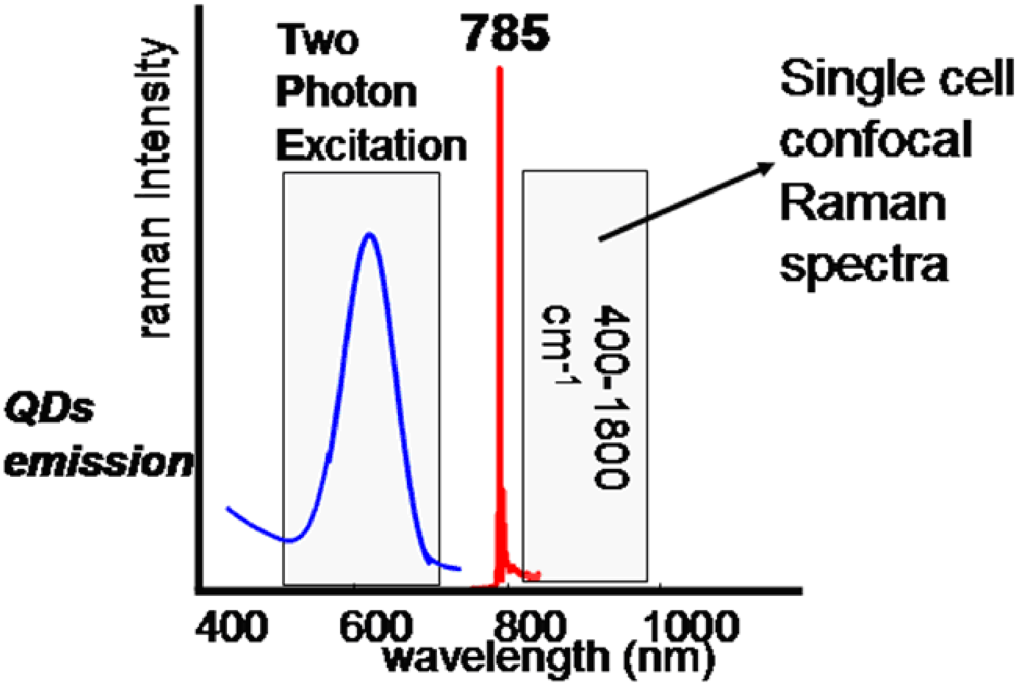

Figure 3.3 Hybrid Confocal Fluorescence Scheme

Using an excitation wavelength of 785 nm it is possible to combine the two-photon excitation fluorescence emission of QDs (emission at 625 nm) on the anti-Stokes side with the Stokes signal of human cells and the quantum dots (Figure 3.3).

3.3 Results

3.3.1 Cytotoxicity

3.3.1.1 Time dependent and dose dependent cytotoxicity

HaCaT cells were treated for 24, 48, 72 and 96 hours with 490QDs at a final concentration of 0.02 nM, 0.2 nM, 2 nM, 20 nM and 200 nM. Then Alamar Blue and Neutral Red assays were performed.

The AB assay is designed to quantify the proliferation of various cell lines and is widely used as a measure of cytotoxicity. Viable proliferating cells cause a reduction of the dye causing a colour change from a non-fluorescing indigo blue (oxidized) to a fluorescent pink species (reduced). As displayed in Figure 3.5, exposure of HaCaT cells to QDs resulted in a small time-dependent decrease in AB reduction close to 10% compared to control levels following 72 h exposures just at highest concentration (200 nM). However, no AB reduction has been noticed after 96 h exposures.

The NR cytotoxicity assay is based on the ability of viable cells to incorporate and bind neutral red, a weak cationic dye that readily penetrates cell membranes by non-ionic diffusion. [5] It accumulates in the lysosomes of cells where it binds to the sensitive lysosomal membrane. Cells damaged by xenobiotic action have decreased ability to take up and bind NR, so that viable cells can be distinguished from damaged or dead cells.

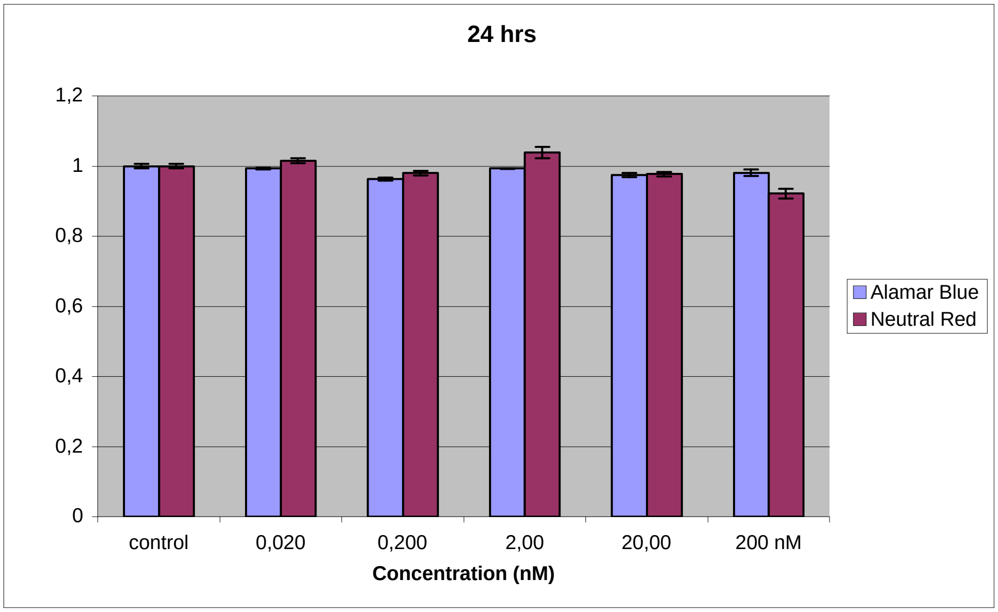

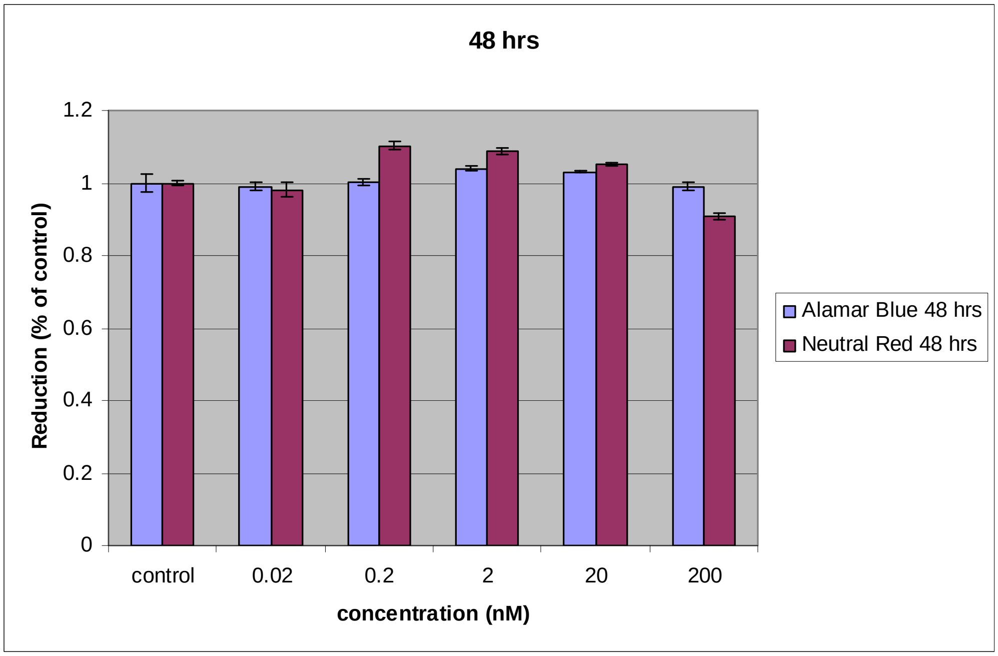

Figure 3.4 Alamar Blue and Neutral Red response at 24 and 48 hrs reduction with respect to the control.

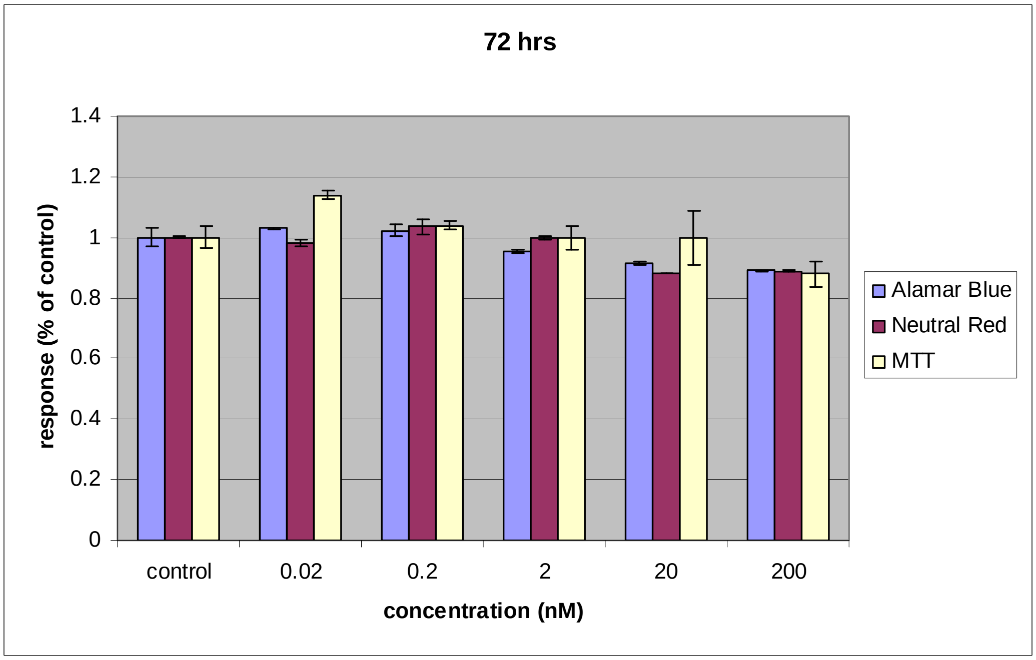

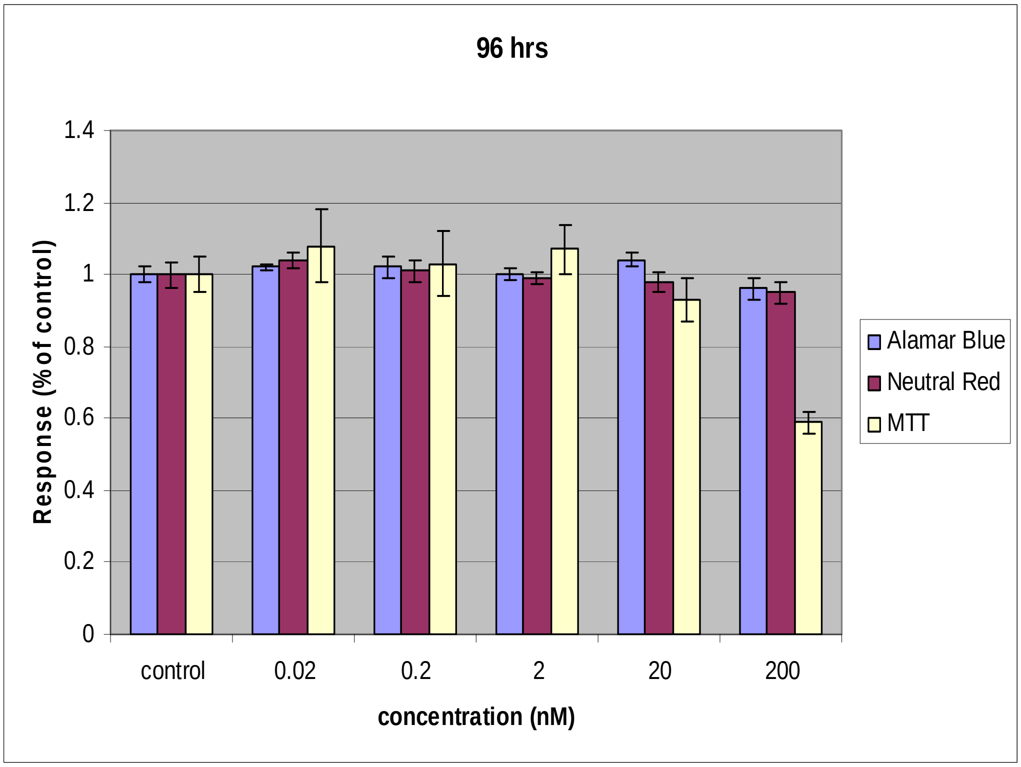

Figure 3.5 Alamar Blue, Neutral Red and MTT response at 72 and 96 hrs reduction with respect to the control.

Exposured of HaCaT cells to QDs resulted in a dose-dependent decrease in NR by only 5 % compared to control levels at all time points. It is interesting to notice that the highest NR reduction, close to 10%, occurred after 72 h exposure and not after 96 h exposures.

The MTT colorimetric assay determines the ability of viable cells to reduce the soluble yellow tetrazolium salt MTT into an insoluble purple formazan precipitate [6,7]. Addition of solvent destroys the cell membrane and results in liberation and solubilisation of the crystals. The number of viable cells is thus directly proportional to the level of the initial formazan product created and can be quantified by measuring the absorbance at 570 nm. [6] The MTT assay was conducted in parallel with AB and NR assays. No significant cytoxicity was determined following 72 h exposure of the HaCaT cells. Following 96 h exposure, significant cytotoxicity was determined however, with approximately 42% inhibition recorded at the top concentration (Figure 3.5)

3.3.2 Phototoxicity

As some applications envisage transdermal exposure to QDs, it was decided to investigate the phototoxicity of QDs by exposing HaCaT cells with increasing QDs concentrations (0.2, 2, 20 nM) for 1 h, and simultaneously irradiating with simulated solar radiation.

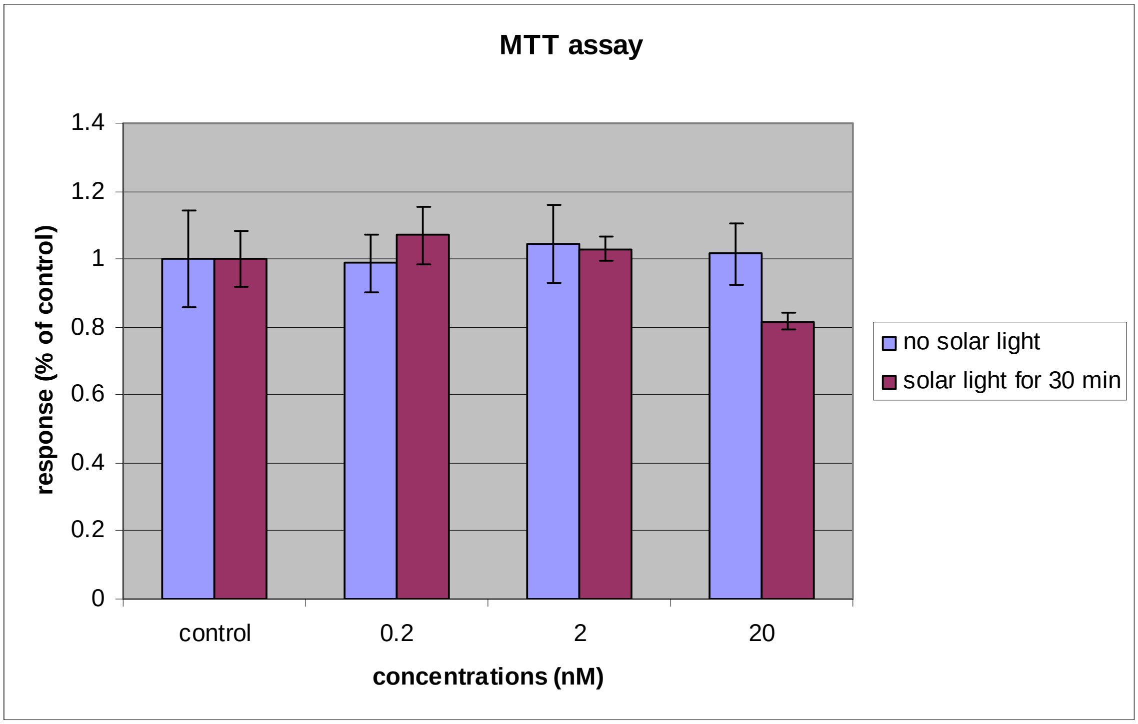

Figure 3.6 MTT response after 1 hr QDs exposure and 30 min of Q-sun exposure with respect to the control.

In this study, two different kinds of exposures are of relevance: exposure of the QDS and subsequent interaction of the excited QDs with the cells, and direct exposure of the cells. Consequently two independent controls have to be considered; two identical 96 well plates were prepared, one of which was not been exposed to the solar light radiation (control 1). As expected, no sign of cytotoxicity in the plate not exposed to the solar light simulator was observed. In contrast, in the 96 well plate exposed for 30 min to the Q-sun radiation there is a reduction in MTT compared to the control (not exposed to the solar light) close to 20%.(Figure 3.6).

From the cytotox analysis without the solar exposure it can be seen that after an exposure of 96 hrs with 20 nM there is a reduction in MTT of just 5% with respect to the control (cells not exposed to QDs).

Repeat the same test in the presence of the solar exposure for 30 min, a reduction in MTT of 18% with respect to the control is observed; in this case it should be noted that the control is the MTT value of HaCaTs simply exposed to the nanoparticles for 96 hrs.

3.3.3 In vitro imaging

Intracellular accumulation of 625QDs after 1-2 hr exposure was revealed in HaCaT cells through confocal fluorescence microscopy by combining “z-stack” image series cutting through the cell in single z-steps of X μm (Figure 3.7) with three-dimensional (3D) animation using the Zeiss LSM Image software.

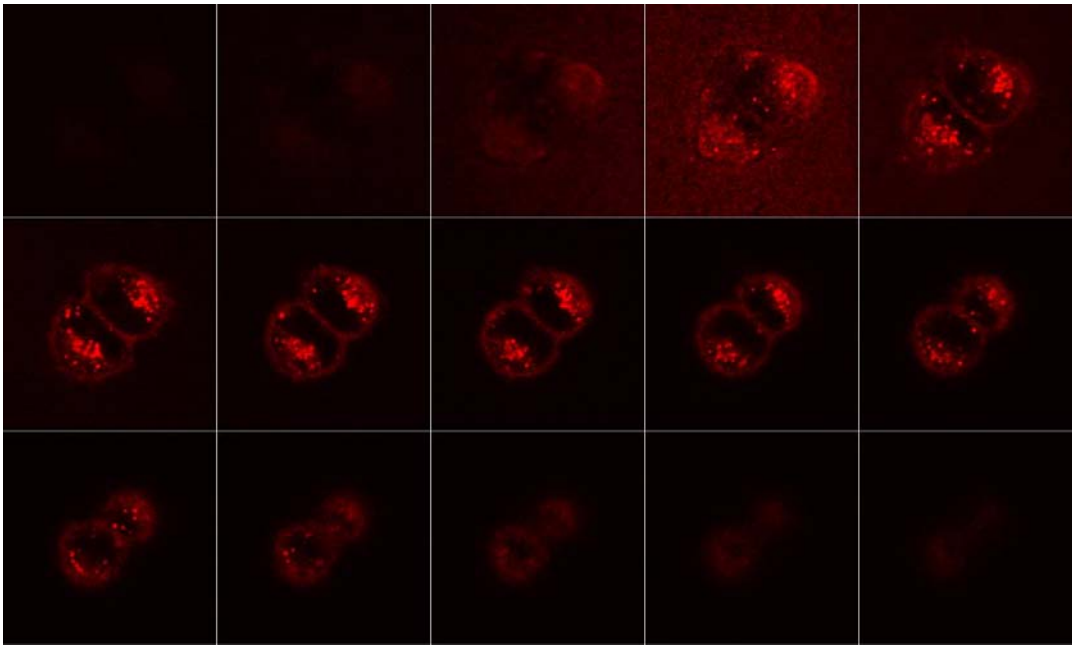

Figure 3.7 Confocal slices through the volume of a cell incubated with the QD625 show that the signal originates from the cell interior and not from material adhered to the surface.

3.3.3.1 Internalization

After a 2hr incubation period, QDs were present in most of the cells analysed appearing as aggregates within the cell cytoplasm, indicating that the uptake was accomplished in a relatively short period of time. This pattern is likely due to the presence of vesicles that result from the endocytotic uptake of QDs.

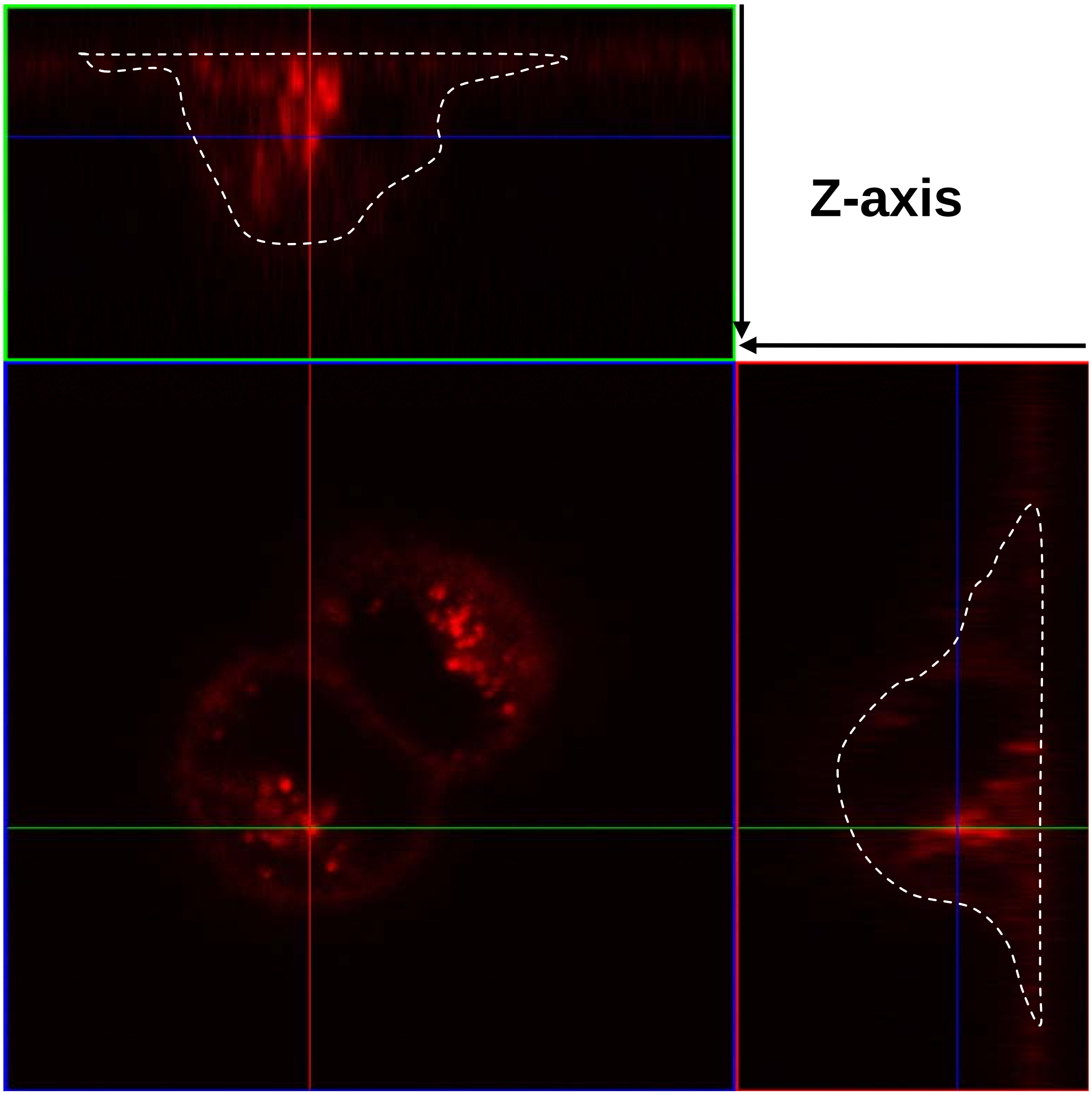

Figure 3.8 Images shows the *z,x* section (upper panel) and the *z,y*section (right panel) cutting orthogonally through the cell obtained from *z*-stack image series of the cells. QDs were observed in perinuclear clusters inside the cells.

3.3.3.2 Colocalisation

The perinuclear distribution of the QDs in the HaCaT cells (Figure 3.8) is consistent with location within the lysosomes. Lysosomes are spherical organelles that contain enzymes (acid hydrolases). They break up food so it is easier to digest. They are found in animal cells and their function is to digest excess or worn-out organelles, food particles, and engulfed viruses or bacteria.[4]

The presence of QDs within the lysosomes was tested by analyzing the HaCaT cells labelled with green Lysotracker probes and red-emitting QDs. The vesicles containing QDs colocalized almost completely with those labelled by the lysosome marker as shown in Figure 3.9. This represents strong evidence that the QDs are internalized by endocytosis and localized in the lysosomes. This mechanism has similarly been proposed by Montiero.[8]

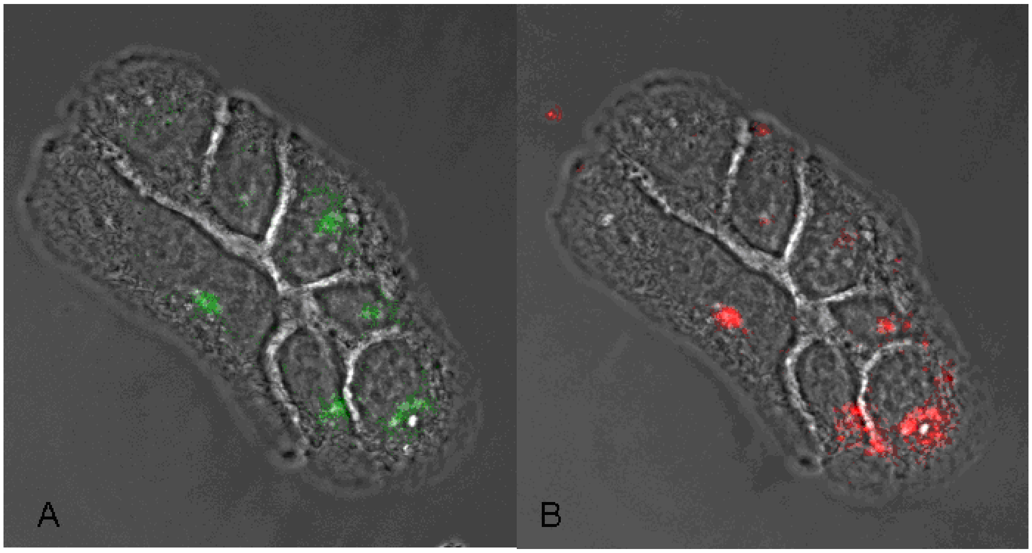

Figure 3.9 Confocal images of HaCaT cell with green Lysotracker (A) and with 625QDs (B)

3.3.4 Raman mapping

Figure 3.10 demonstrates the possibility of Raman spectroscopy to localise the presence of the QDs within the cell using two different approaches: single photon excitation fluorescence (SPEF, ex = 473 nm) and two-photon excitation fluorescence (2PEF, ex = 785 nm). Spectra were collected over a HaCaT cell (~ 20x15 μm) respectively over the range 4000 – 6000 cm^{-1} and -5000 to - 3000 cm^{-1}.

The step size was 0.5 μm for the single photon excitation process and 1 μm for the two photon excitation process. The two maps give a broad idea about the distribution of the NPs within a cell and demonstrate that either one or two photon fluorescence can be employed to localize the QDs inside the cells.

After the localisation of QDs based on their fluorescence, it is possible to record spectra of the cell in the fingerprint region (600-1800 cm^{-1}); potentially changes to the cellular spectrum can be mapped and localised with the QDs fluorescence. Ultimately Raman can look at local changes as well as over changes to cellular physiology as a result of interaction with the QDs.

785 nm

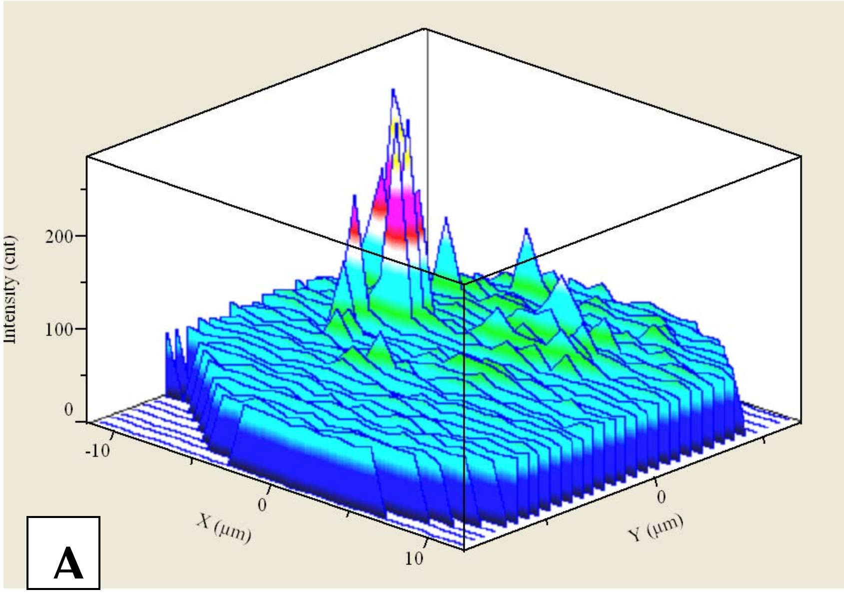

473 nm

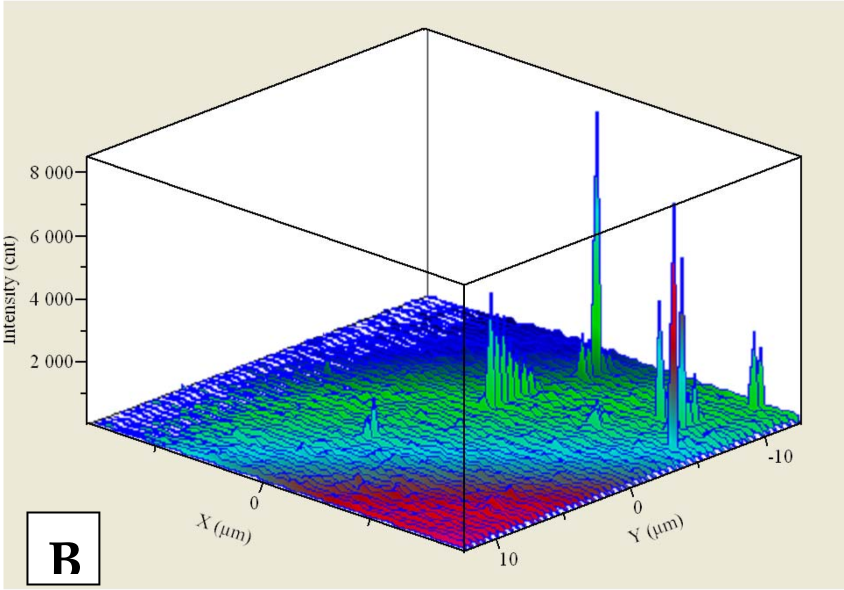

Figure 3.10, QDs localization within a single cell. (A) laser line 785. (B) laser line 473. The differential intensity of the QDs emission possibly depends on the concentration of the QDs and on the distance from the focal plane.

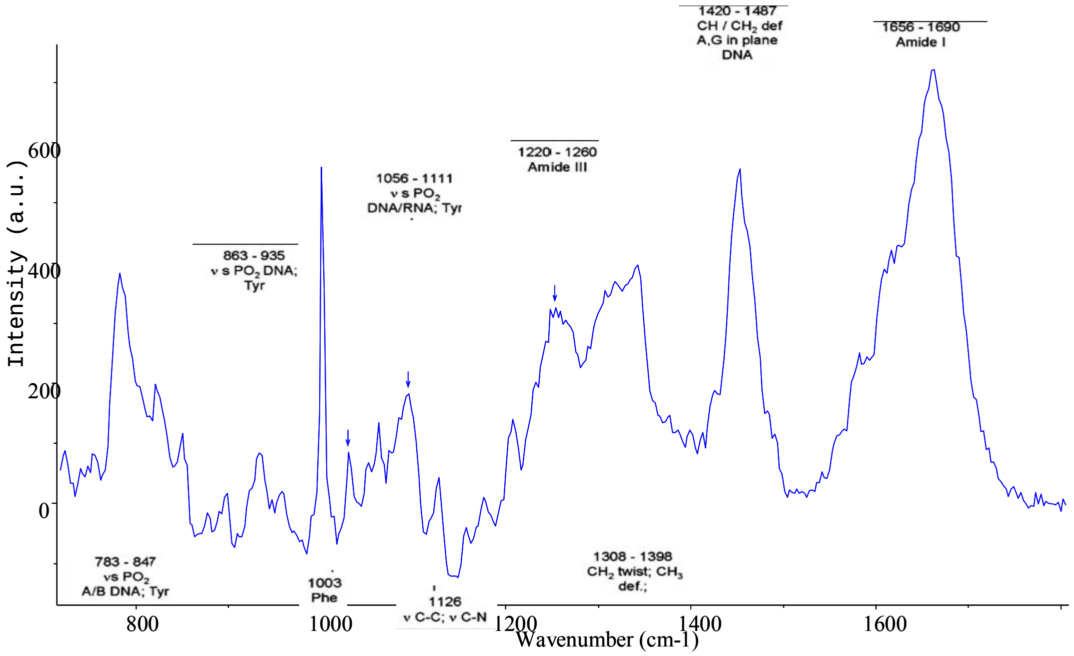

Figure 3.11, Raman spectrum of HaCaT cells exposed to QDs.

It is interesting to note that it is not possible to see any difference between the Raman spectrum of HaCaT cells exposed to QDs and not exposed to QDs.

3.4 Conclusion

3.4.1 Cytotoxicity

Results suggest no significant change in metabolic activity as a measure of proliferation and viability at 24 hrs and 48 hrs. At 72 hrs, however, a moderate decrease in the metabolic activity at high concentrations (20 nM, 200 nM) is discernable. After 96 hrs of exposure at a concentration of 200 nM no significant change in proliferation and viability activity but a significant reduction of the mitochondrial activity is observed. The weak or negligible cytotoxicity of these materials is not unexpected as the PEG coating is specifically added to improve the biocompatibility of the QDs.

3.4.2 Photoxicity

The three concentrations chosen (0.2, 2, 20 nm) are part of the concentration set utilized for the dose and time dependent toxicity study; this choice permits us to give a more broad vision of sun light, concentration and time of exposure effects. The results show a reduction of almost 20% in mitochondrial activity due to the exposure to the solar light simulator.

In conclusion it is confirmed that QDs nanoparticles are not particularly toxic even after long exposures and high concentrations (200 nm) but they become toxic under solar light irradiation.

3.4.3 Confocal and Raman mapping

The confocal fluorescence study showed that the QDs after one hour exposure stay in the lysosomes, supporting an internalisation of endocytosis. The particles are easily detectable inside the cells using the Raman spectrometer. At the same time with Raman spectroscopy it should be possible to detect the local environment of QDs within a HaCaT cell. Ultimately, Raman spectroscopy can be used to monitor changes in the physiology of the cell as a result of interaction with the QDs.

3.5 References

1. Meade, A.D., *Growth substrate induced functional changes elucidatedby FTIR and Raman spectroscopy in in–vitro cultured human keratinocytes.* Anal Bioanal Chem, 2006.

2. www.invitrogen.com

3. *Based on Alanna Maguire research at the FOCAS Institute.*

4. Alberts, B., *Molecular Biology of the Cell.*

5. Borenfreund, E., H. Babich, and N. Martin-Alguacil, *Comparisons of two in vitro cytotoxicity assays--The neutral red (NR) and tetrazolium MTT tests.* Toxicology in Vitro, 1988. 2(1): p. 1-6.

6. Mosmann, T., *Rapid colorimetric assay for cellular growth and survival: Application to proliferation and cytotoxicity assays.* Journal of Immunological Methods, 1983. 65(1-2): p. 55-63.

7. Supino, *MTT Assays. In O'Hare, S. and Atterwill, C.K., .* In vitro toxicity testing protocols, 1995. Humana, Clifton: p. 137-149.

Chapter 4

Localisation of QDs using Raman Cross-correlation

4.1 Introduction

In Chapter 2 it was shown that it is possible to localize Quantum dots by both single photon excitation fluorescence (SPEF) and two photon excitation fluorescence (PEF). In the latter case, the Raman and fluorescence can be collocated by analyzing respectively the Stokes and the anti-Stokes side of the Raman spectra.

In general, however, nanoparticles are not fluorescent and it is a challenge to locate the particles within cells and even more so to perform collocation studies such as those of section 3.2.4 using lysotracker. Such studies are extremely valuable in identifying uptake mechanisms, mechanisms of toxicity and ultimate fate of the nanoparticles in cells [1] Although fluorescent labelling of nanoparticles is common practice, the stability of the labels has been called into question. [2] Ultimately it is desirable to be able to locate the nanoparticles within cells based on their chemical composition. To this end the highly luminescent QDs can be employed to explore detection methods.

In Chapter 1 it was shown that the QDs used in this study are coated externally with a thick layer of PEG. The PEG coating constitutes more than 90% of the entire volume of the NP. As shown in chapter 2, it gives the QDs a characteristic Raman signature which can potentially be used to locate them within a cellular environment. Collocation of the PEG Raman signature with the intrinsic luminescence can be used to validate the use of the Raman signature as a detection and location technique, such that it can be potentially extended to non fluorescent nanoparticles.

The PEG signature spectrum will be locally correlated with the cellular spectrum and thus a cross-correlation method will be developed to extract the PEG signal and thus locate the QDs within the cells. The feasibility of the process will initially be demonstrated using simulated mixtures of cellular and QD Raman spectra, whereby the sensitivities and detection limits can be explored. The process will then be demonstrated experimentally.

Before presenting the theoretical and experimental study, the mathematical concept of cross-correlation is outlined.

4.1.1 Cross correlation - Theory

Cross correlation is a measure of similarity between two data sets, computed by the sum of the products between the two data sets at different (x-axis) off sets. In another words, the cross-correlation function gives a measure of the extent to which two signals correlate with each other as a function of the displacement between them. If the signals are identical, an autocorrelation is performed and the result will be one, and if they are completely dissimilar, the cross correlation will be zero.

The complex *cross correlation* of *f(x)* with *g(x)* is defined as: [3]

$$c_{fg}(x) = f(x) \star g^{*}(x) = \int_{-\infty}^{\infty} f(u)\, g^{*}(u - x)\, du$$

Equation 4.1

The corresponding definition of cross correlation for sequences would be:

$$c_{fg}[m] = \sum_{n=-\infty}^{\infty} f[n+m]g^{*}[n]$$

Equation 4.2

If the functions are identical, the cross correlation gives the autocorrelation function.

Cross correlating one signal with another is a means of measuring how much of the second signal is present in the first. This can be used to “detect” the presence of known signals as components of more complex signals. The cross-correlation function is used extensively in pattern recognition and signal detection.[4] In the current study, the Raman spectrum of PEG is known and the objective is to detect and localise it within a spectral map of a cell. In this scenario, x of equation 4.1 is the spectral axis in wavenumber and the process of cross correlation is performed by shifting the spectra along the axis an amount u.

Cross correlation analysis was performed with MATLAB, using the function *crosscorr*. It computes and plots the sample cross correlation function (XCF) between two univariate, stochastic time series. In MATLAB *crosscorr* produces correlations identically equal to 1.0 at zero lag only when an autocorrelation is performed.

4.1.2 Cross-correlation for identification of external agents in Raman Spectra of a single cell.

The potential uses of the cross correlation technique for the localization of QDs within a cellular map were initially explored using simulated mixtures of cellular and QD spectra. Raman spectra of QDs (i.e. PEG spectrum) and HaCaT cells were initially recorded (Figure 4.1) and simulated spectra of mixtures of QDs within a cell were generated. After a normalization of both QD and cell spectra, varied percentages of the QD spectrum: 100% - 0.01%, are added to simulate varying contributions in a real sample. A second normalization is then performed. Subtraction of background from both spectra as well as derivatisation was explored to improve the correlation process. The simulated spectra were loaded in MATLAB and then a cross-correlation of the simulated spectra with respect to the QD spectrum was performed. [Appendix A - MATLAB codes]

To decide the most appropriate spectral windows to apply the cross-correlation to, the QD spectrum compared to the HaCaT cell spectrum was analysed. The ideal region is one with intense QD peaks and no peaks in the cellular spectrum.

As described in chapter 2 and shown in figure 4.1, the QD spectrum shows various intense peaks at 850, 1062,1129/1145, 1281 (shoulder at 1295), 1442/1475 cm^{-1}.

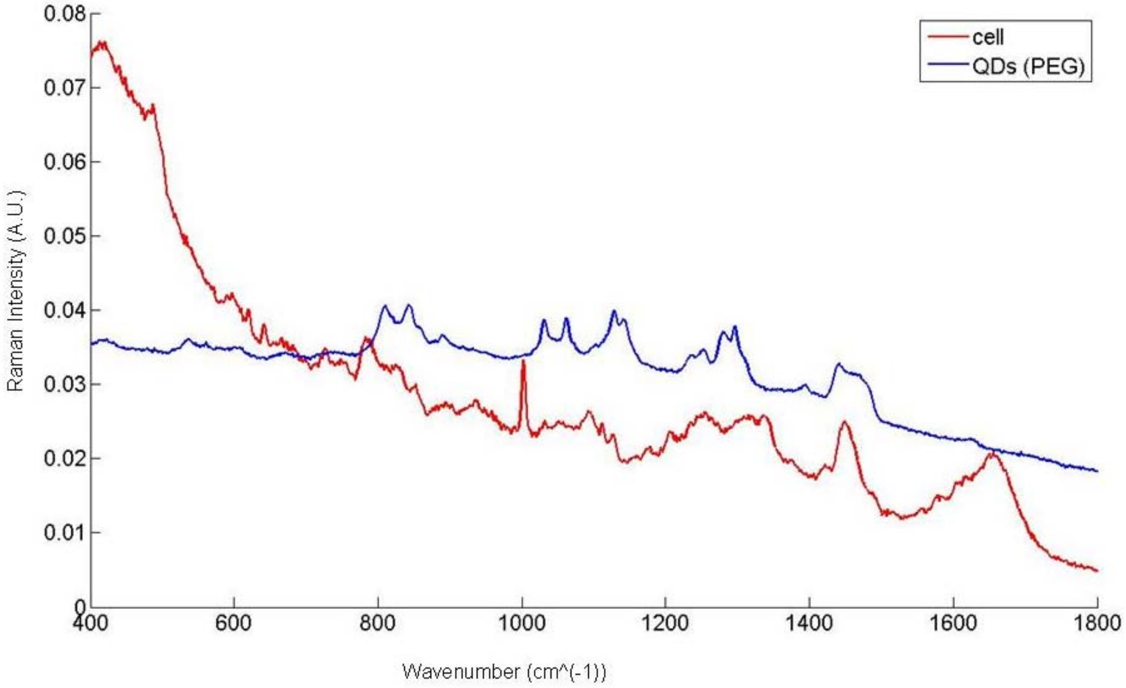

Figure 4.1 QDs and HaCaT cell Raman spectra.

Comparing the QD spectrum with the cellular spectrum, (Figure 4.1) it can be seen that there is no clear window where QDs peaks do not overlap with cellular features. The best region to perform the cross correlation was chosen to be 800-1250 cm^{-1}, because the QDs peaks at 1281 (shoulder at 1295) and 1442/1475 cm^{-1} overlap with some characteristic Raman peaks of human cells. For comparison, in this study the cross correlation was applied to two different spectral windows: the *extended region*, 800-1800 cm^{-1}, and the *reduced region*, 800-1250 cm^{-1} .

4.2 Cross-correlation of simulated spectra

4.2.1 Raw data

Initially, the cross correlation of the raw data was performed without any preprocessing such as baseline correction or filtering.

4.2.1a. Window: 800-1800 cm^{-1}

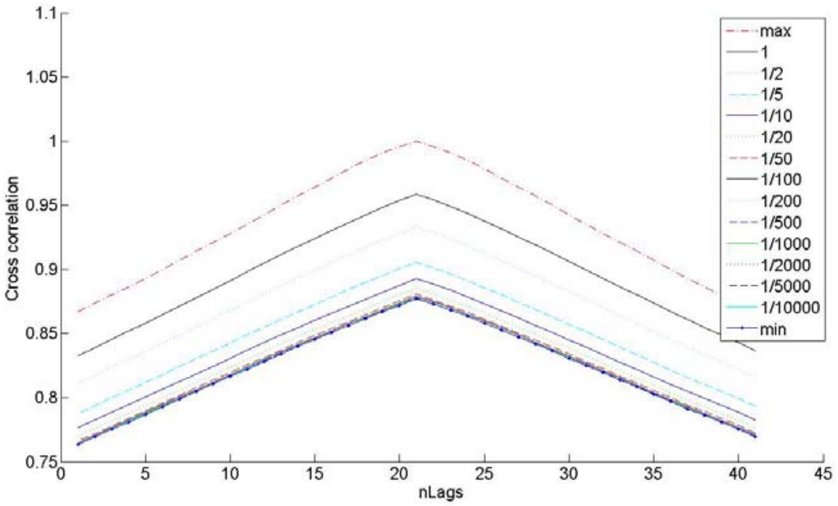

Figure 4.2 Cross-correlation of QD spectrum and simulated spectra.

Figure 4.2 shows the cross correlation curves of the QD spectrum with the simulated spectra of decreasing ratios of QD:cellular spectra. The parameter nLags describes the x-axis shift and the response is peaked at nLags = 21. The “max” curve of Figure 4.2 shows an auto-correlation which shows a maximum of 1, as expected.

Figure 4.3 shows a plot of the cross-correlation maxima as a function of spectral ratio. It is first noted that there is very little difference between the maximum (autocorrelation) and minimum curve (correlation between cell spectrum without QDs and QD spectrum). The Range of Maxima expresses this difference; Range of Maxima: 0.88-0.96 (ΔMax=0.08). The cross-correlation is also observed to be distinctly sublinear. In this study the norm of residuals is used as a measure of the goodness of the linear fit; a lower norm means a better fit. In this case the norm of residuals is 0.017339.

In figure 4.4, for visual purposes, the lowest value is subtracted from the cross-correlation maxima.

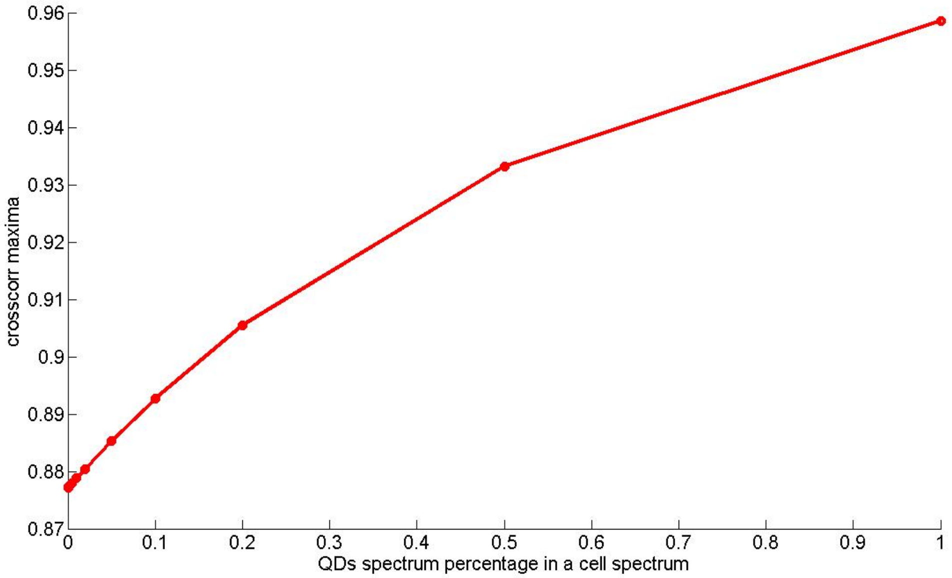

Figure 4.3 Cross-correlation maxima Vs concentration of QDs spectrum in a cell spectrum.

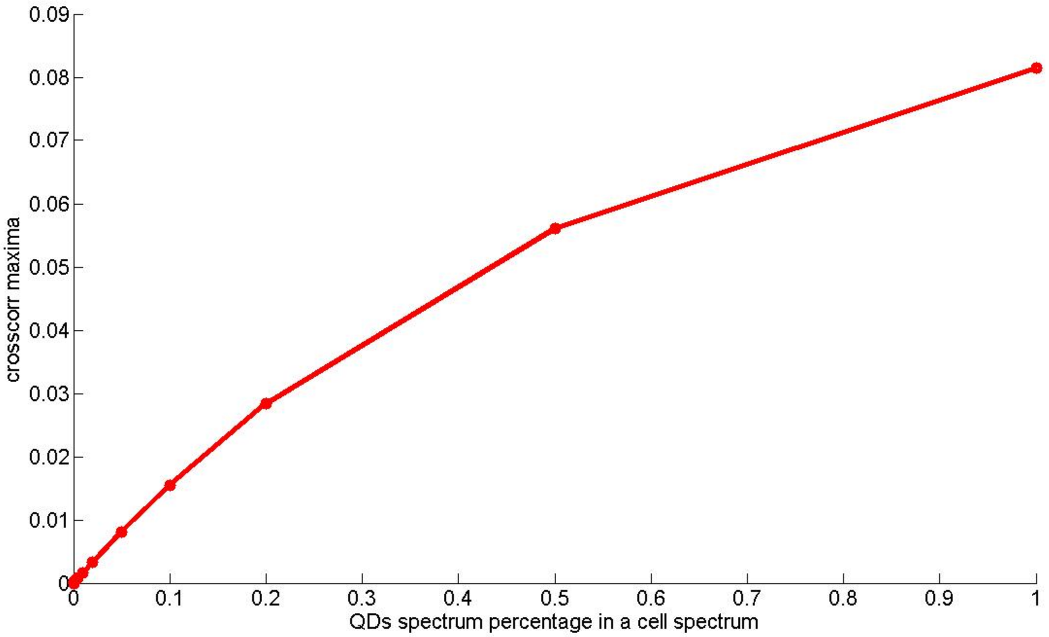

Figure 4.4 Cross-correlation maxima (after the deduction of the lowest value) Vs concentration of QDs spectrum in a cell spectrum.

Finally in figure 4.5 the data is presented in a log-log representation from which it is possible to deduce the limit of detection; the intercept of the curve with the x axis in a log-log scale is a measure of the limit of detection for the cross-correlation method. The limit of detection can be extrapolated to 6×10^{-5}, which indicates that the technique could be employed to detect “concentrations” of QDs as low as 0.01%.

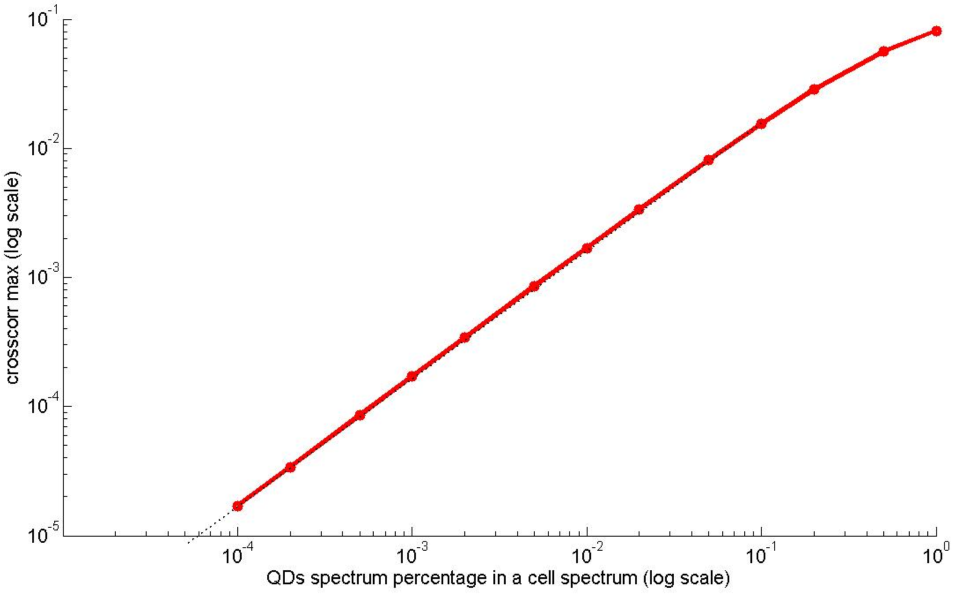

Figure 4.5 Cross-correlation maxima Vs concentration of QDs spectrum in cell spectrum in a log-log scale.

4.2.1b. Window 800-1250 cm^{-1}

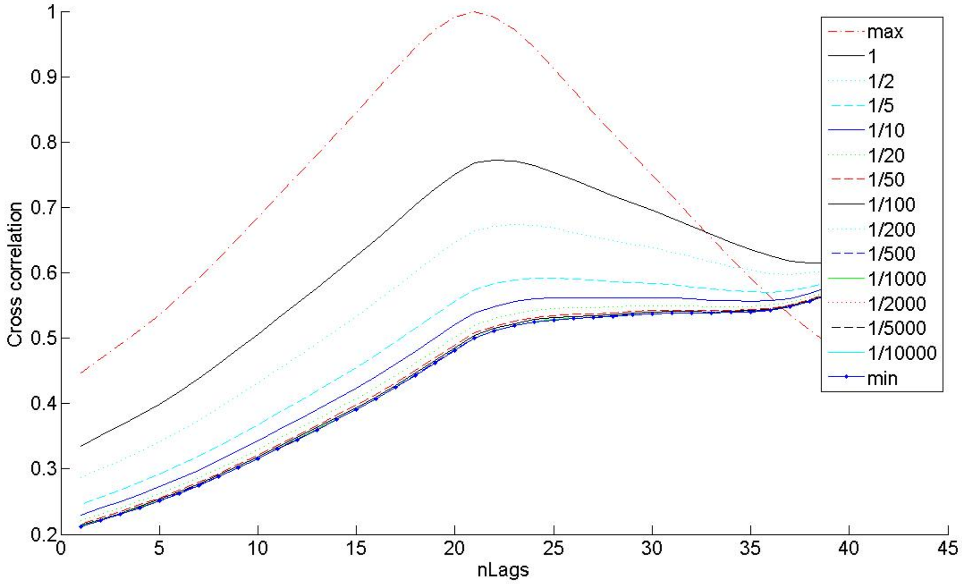

Figure 4.6 Cross-correlation of QDs spectrum and simulated spectra – reduced range.

The cross-correlation of the raw data was performed in the reduced spectral window: *800-1250 cm^{-1}*. The range of maxima increases sensibly compared to the full range: 0.5-0.78 (ΔMax=0.28). The linearity is reduced, however, the norm of residuals increasing from 0.017339 (full window) to 0.024787 (small window). The extrapolated limit of detection has been reduced to 1 x 10^{-5}.

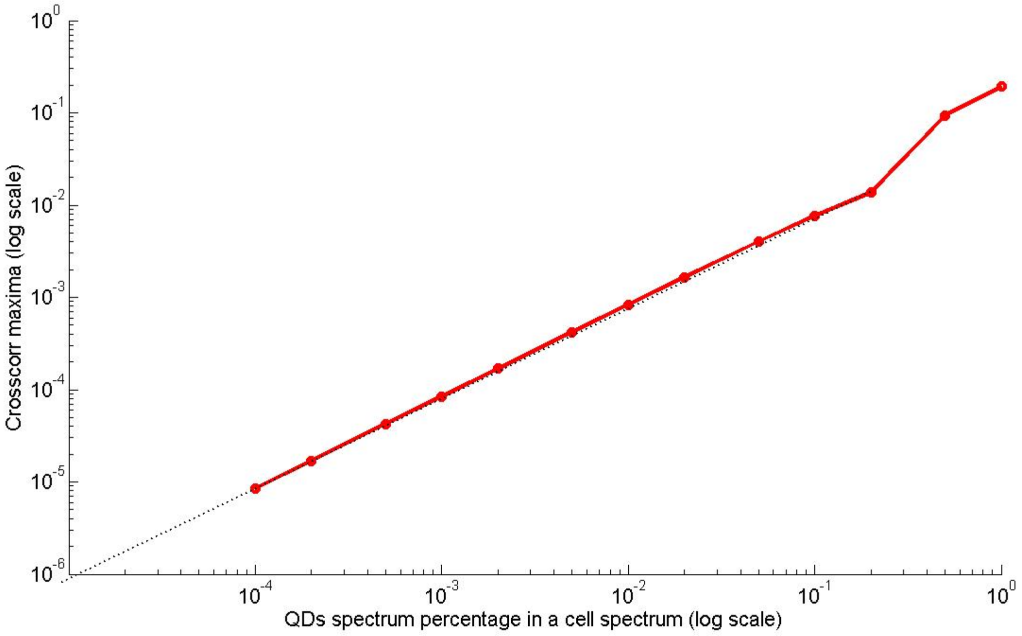

Figure 4.7 Cross-correlation maxima Vs concentration of QDs spectrum in cell spectrum in a log-log scale.

4.2.2 Baseline correction

Although the cross-correlations of 4.2.1 promise extreme sensitivity, the correlation range and linearity are disappointing. An ideal Raman spectrum has Raman bands which lie on a flat baseline. A broadband perturbing spectrum or background spectrum, generally from fluorescence or Mie scattering, is unfortunately often superimposed on the Raman spectra. This perturbing spectrum may have very different profiles. In any event, a perturbing spectrum falsifies the desired Raman spectrum and makes it difficult to evaluate. Various methods have therefore already been employed in order to eliminate the perturbing spectrum from the Raman spectrum.

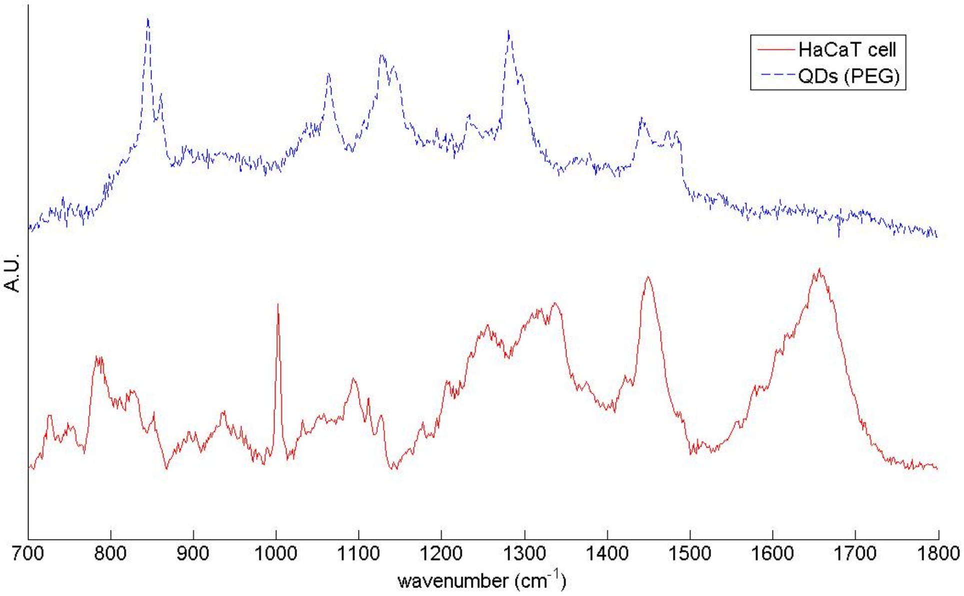

Figure 4.8 Spectra of HaCaT cells and QDs after the baseline subtraction.

A baseline correction to the QD and cellular spectra using a “rubber band” function was performed.[5] A “rubber band” function consists of finding a convex envelope of the spectrum and subtracting the convex part of the envelope lying below the spectrum from the spectrum in the portion to be corrected. Figure 4.8 shows the cellular and QD Raman spectra after background subtraction.

4.2.2.a Window: 800-1800 cm^{-1}

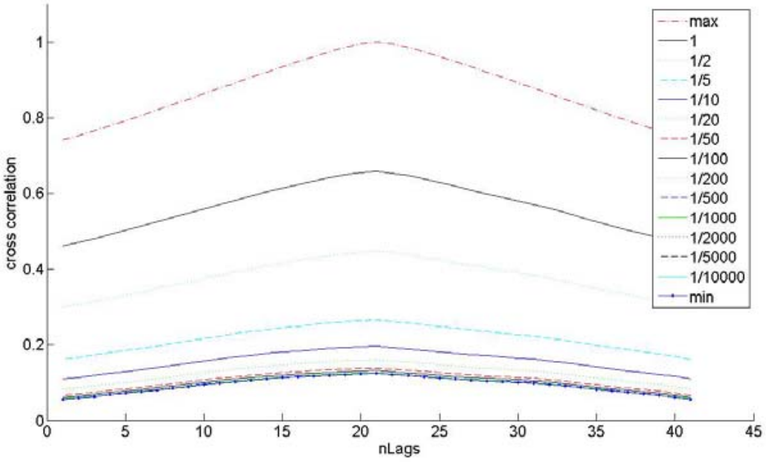

Figure 4.9 Cross-correlation of background subtracted QDs and simulated spectra.

Figure 4.9 shows that the baseline correction considerably improves the range of maxima: 0.1 – 0.6 (ΔMax=0.5). Strangely, the linearity is decreased with respect to the raw data. The norm of residuals is now 0.057078. The limit of detection is ~1.5 x 10^{-5}.

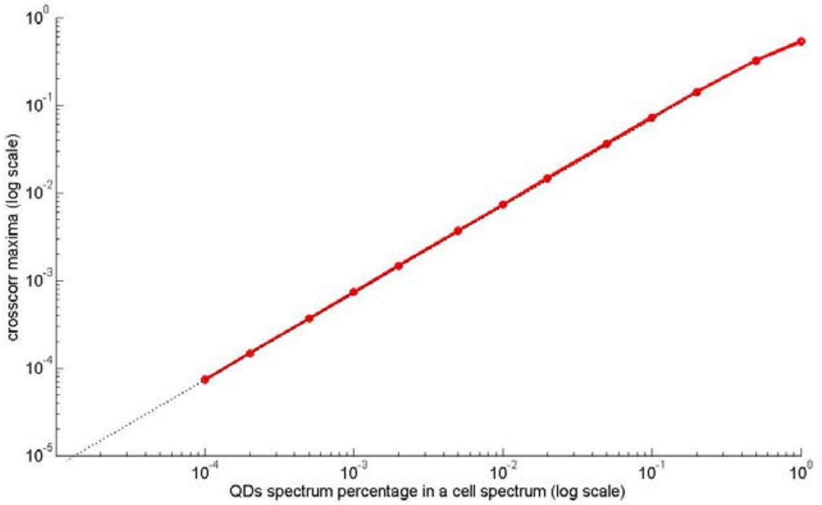

Figure 4.10 Cross-correlation maxima Vs concentration of QDs spectrum in cell spectrum in a log-log scale.

4.2.2.b Window 800-1250 cm^{-1}

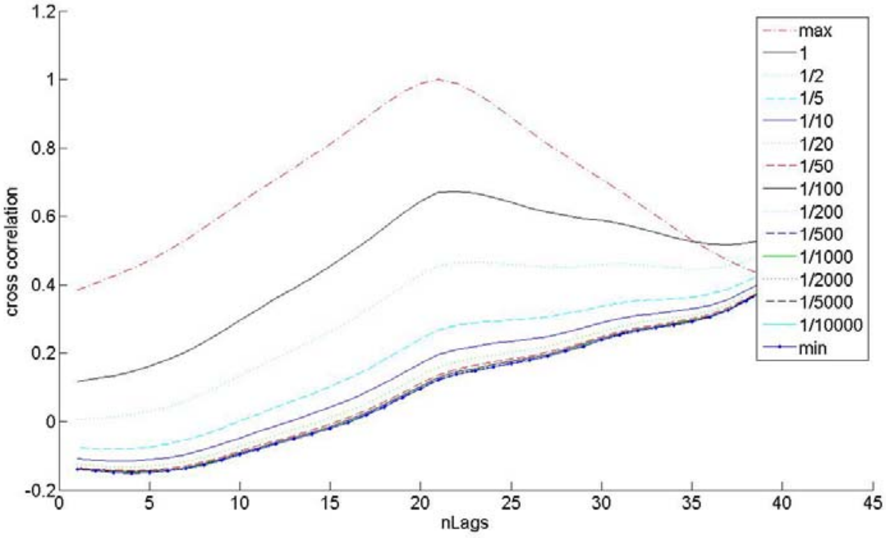

Figure 4.11 Cross-correlation among QDs spectrum and simulated cells spectra.

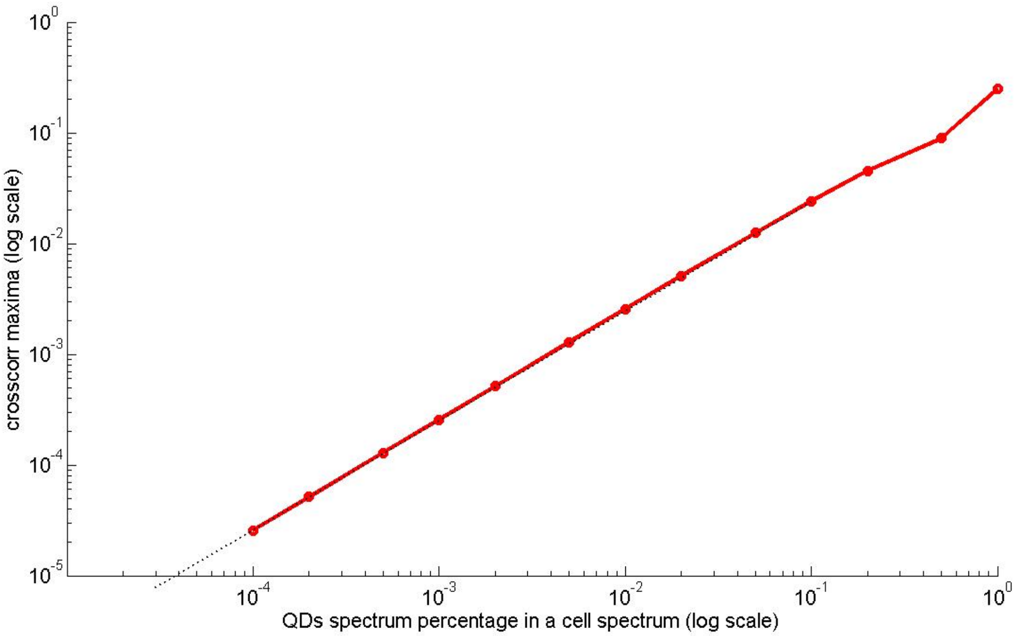

Figure 4.12 Cross-correlation maxima Vs concentration of QDs spectrum in cell spectrum in a log-log scale.

Using the reduced spectral window, the Range of Maxima is slightly improved: 0.1-0.63 (ΔMax=0.5). As compared to the raw data, the linearity is negatively affected by the reduction of the window. The norm of residuals increases from 0.024787 to 0.030756. The limit of detection is increased to ~ 4 x 10^{-5}.

4.2.3 Baseline correction plus filtering

Filtering of the spectra was performed by use of Savitzky-Golay filters. This filter is used for smoothing of one-dimensional data. The fundamental idea is to fit a different polynomial to the data surrounding each data point. The smoothed points are computed by replacing each data point with the value of its fitted polynomial. The smoothing function was applied to the baseline subtracted spectra and the simulated cross correlation repeated.

4.2.3a Window: 800-1800 cm^{-1}

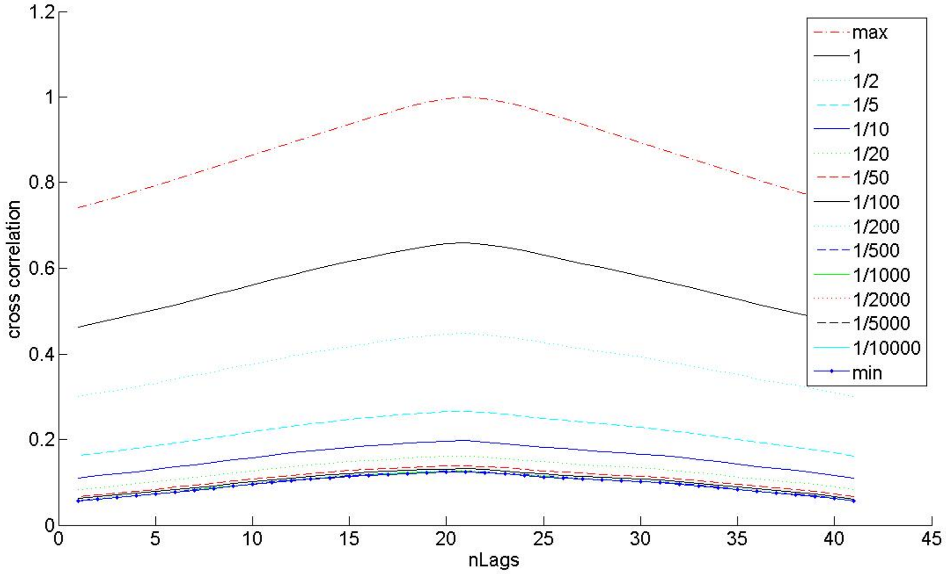

Figure 4.13 Cross-correlation of smoothed and baseline subtracted QDs simulated spectra.

Filtering is seen to increase the range of Maxima with respect to the baseline correction data: 0.1-0.63 (ΔMax=0.53). The linearity is slightly improved due to the filtering; the norm of residuals is now 0.0072434. The Limit of detection is now ~1.5 x 10^{-5}.

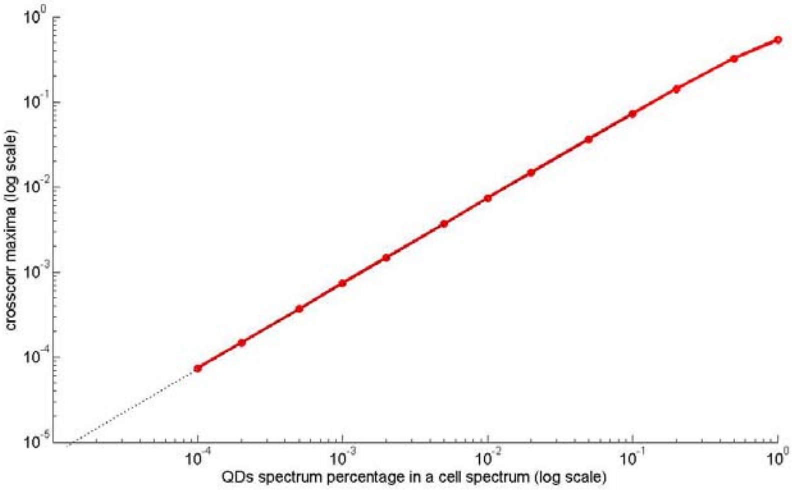

Figure 4.14 Cross-correlation maxima Vs concentration of QDs spectrum in cell spectrum in a log-log scale.

4.3.3b Window 800-1250 cm^{-1}

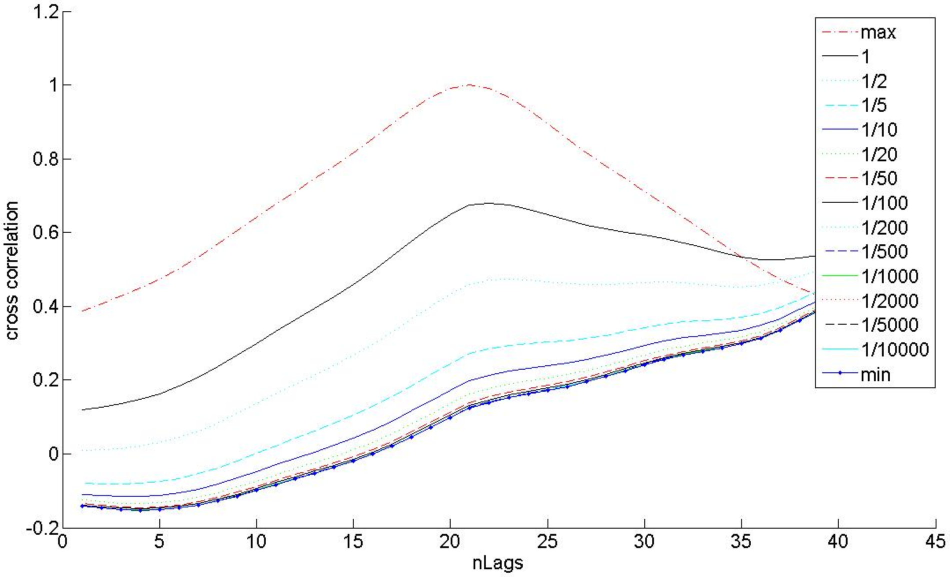

Figure 4.15 Cross-correlation among QDs spectrum and “artificial” cells spectra.

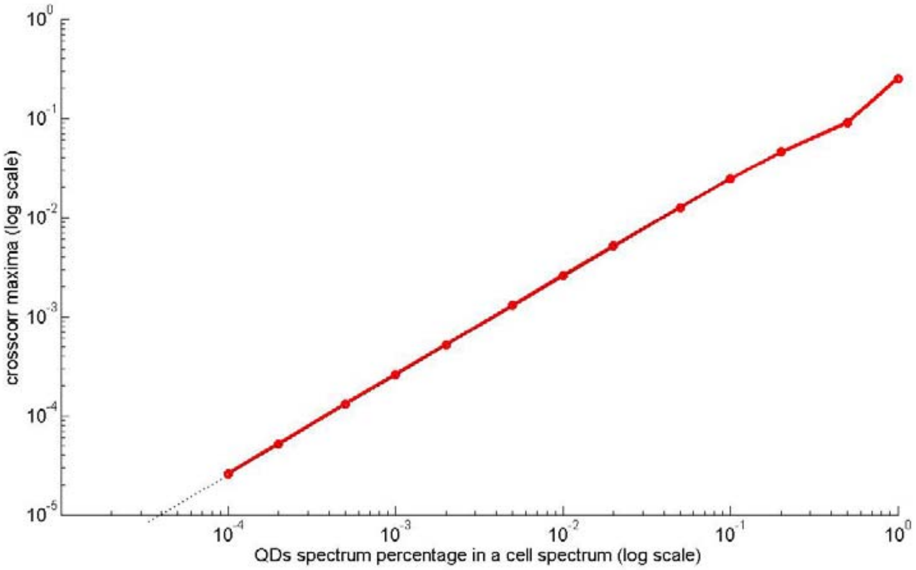

Figure 4.16 Cross-correlation maxima Vs concentration of QDs spectrum in cell spectrum in a log-log scale.

With the reduced window, the range of maxima is increased from 0.1 to 0.7. The linearity is also positively affected by the reduction of the window. In this case the norm of residuals is 0.0.031425. The Limit of Detection remains at 4 x 10^{-5}.

4.2.4 Filtering and First derivative

In the last case studied, filtering of the QDs and cell spectra was performed and subsequently the first derivative of both was taken before cross correlation. In this case, the baseline correction is not necessary because the baseline is effectively removed by derivatisation.

4.2.4a. Window: 800-1800 cm^{-1}

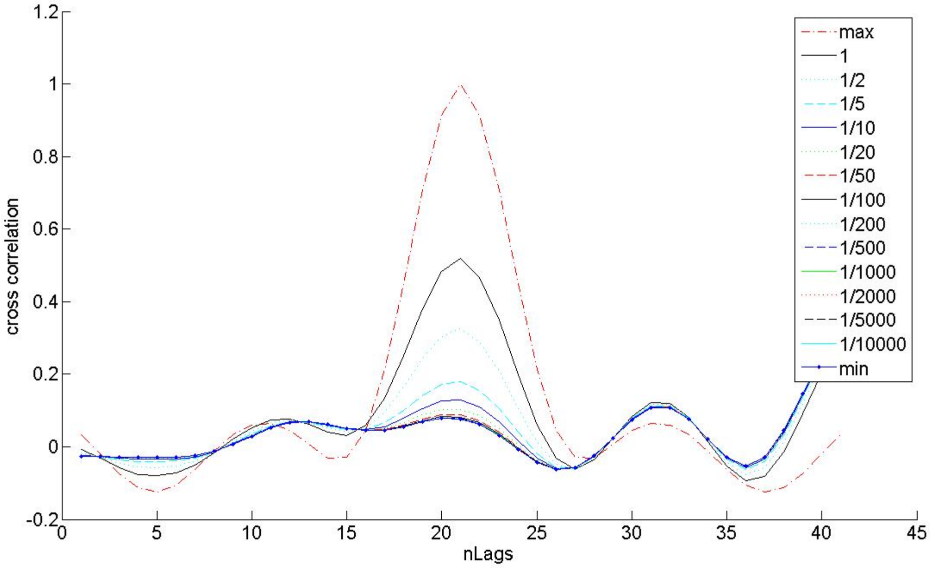

Figure 4.17 Cross-correlation among QDs spectrum and "artificial" cells spectra.

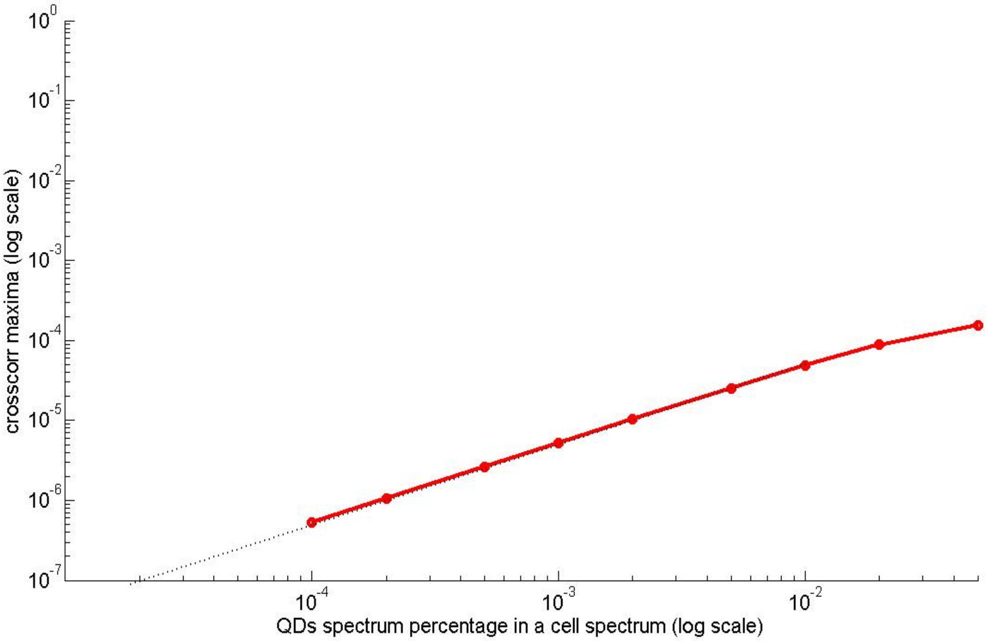

Figure 4.18 Cross-correlation maxima Vs concentration of QDs spectrum in cell spectrum in a log-log scale.

The first derivative doesn't increase the Range of Maxima: 0.1-0.5 (ΔMax=0.4). In general, the linearity is very badly affected by the first derivative as the norm of residuals is 0.086059. The limit of detection is ~2 x 10^{-5}.

4.2.4b Window 800-1250 cm^{-1}

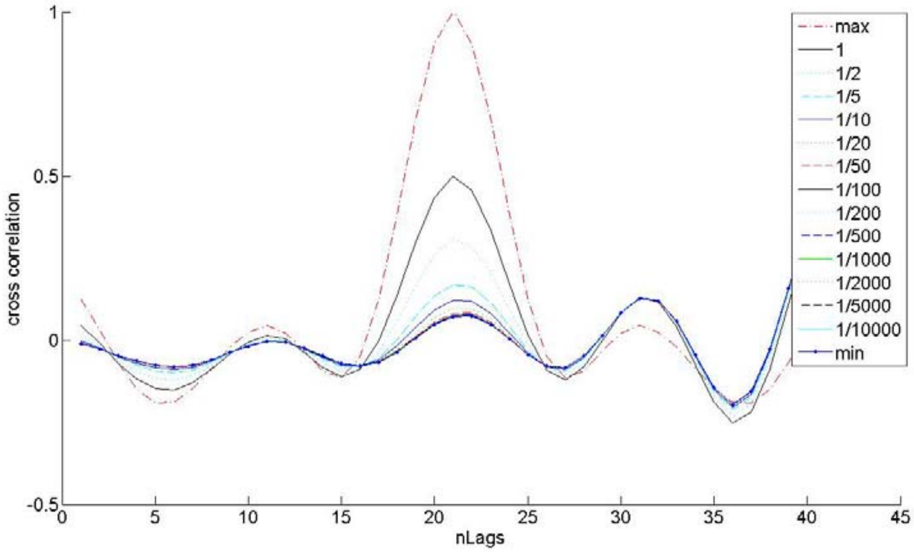

Figure 4.19 Cross-correlation among QDs spectrum and "artificial" cells spectra.

With the reduced spectral range, the Range of Maxima is still high: 0.1-0.5 (Δ=0.4). The linearity improved sensibly using the reduced range. The norm of residuals 0.014287, the best value among all the cases studied. The limit of detection has decreased to ~ 2 x 10^{-5}.

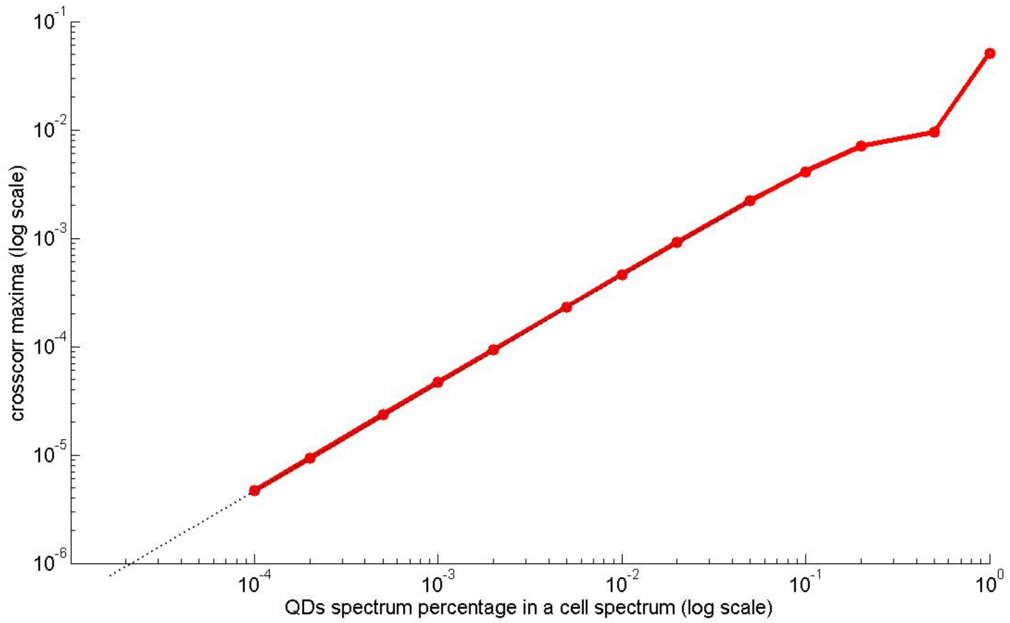

Figure 4.20 Cross-correlation maxima Vs concentration of QDs spectrum in cell spectrum in a log-log scale.

4.2.5 Conclusion

Table 4.1 summarises the results of the simulation study. It is concluded that the best compromises among the various parameters (range of Maxima, linearity, limit of detection) are the filtering and baseline correction and filtering and first derivative both in the reduced spectral range (800-1250 cm^{-1}).

	Range 800-1800 cm^{-1}	**Range 800-1250 cm^{-1}**
Raw data	Range of Maxima: 0.88-0.96 (Δ=0.08) Norm of residuals: 0.017339 Limit of detection: 6 x 10^{-5}	Range of Maxima: 0.5-0.78 (Δ=0.28) Norm of residuals: 0.024787 Limit of detection: 1.5 x 10^{-5}
Baseline correction	Range of Maxima: 0.1 – 0.6 (Δ=0.5) Norm of residuals: 0.057078 Limit of detection: 2 x 10^{-5}	Range of Maxima: 0.1 – 0.63 (Δ=0.53) Norm of residuals: 0.030756 Limit of detection: 4x 10^{-5}
Filtering and baseline correction	Range of Maxima: 0.1-0.63 (Δ=0.53) Norm of residuals: 0.057358 Limit of detection: 2 x 10^{-5}	Range of Maxima: 0.1-0.7 (Δ=0.60) Norm of residuals: 0.031425 Limit of detection: 4 x 10^{-5}
Filtering and first derivative	Range of Maxima: 0.1-0.5 (Δ=0.4) Norm of residuals: 0.086059 Limit of detection: 2 x 10^{-5}	Range of Maxima: 0.1-0.5 (Δ=0.4) Norm of residuals: 0.014287 Limit of detection: 2 x 10^{-5}

Table 4.1 Cross-correlation parameters

4.3 Cross-correlation - Experimental Study

In the previous section, the potential of the cross-correlation method to detect and locate the presence of known external agents within a cell was demonstrated using simulated spectral mixtures. In the case of the highly luminescent inorganic semiconductor quantum dots, in Chapter 2 it has been shown that it is possible to localize them by both single photon excitation fluorescence (SPEF) and two photon excitation fluorescence (TPEF). In the latter case the Raman and fluorescence can be collocated by analyzing respectively the Stokes and the anti-Stokes side of the Raman spectra. (Figure 4.22). A comparison between the spatial profile of the fluorescence and that of the cross-correlation maxima can demonstrate whether cross-correlation is a suitable method to detect and locate any nanoparticles or external agents within a cell.

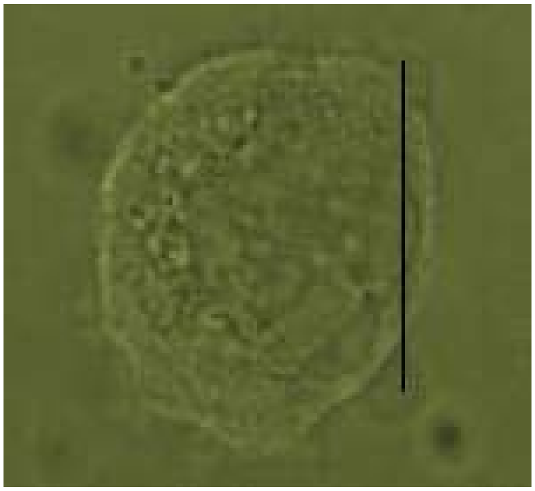

Figure 4.21 Line Raman mapping of a single HaCaT cells.

To this end, fluorescent maps of HaCaT cells exposed to QDs were performed, and in regions where the QD were identified, Raman line maps (Figure 4.21) were performed and subsequently cross-correlated with the QD spectrum. The fluorescence spatial profiles were then compared to the cross-correlation profiles.

Below, the procedures used to perform this experimental study are listed:

- Seeding of 20,000 HaCaT cells on a quartz slide.
- HaCaT cells exposed to 20 nM of 625QDs for 1 h.
- Line Raman mapping of two widows: -4000 to -2700 cm^{-1} (anti-Stokes side) and 400-1800 cm^{-1} (Stokes side).
- Line Raman mapping in the Stokes-side, 400 to 1800 cm^{-1}.
- Raman spectrum of dried QDs, 400-1800 cm^{-1}.
- Cross-correlation of the Raman spectra respect to the QDs Raman spectrum in the finger print region.
- Comparison of the fluorescence profile of the QDs with the cross-correlation maxima profile in the finger print region.

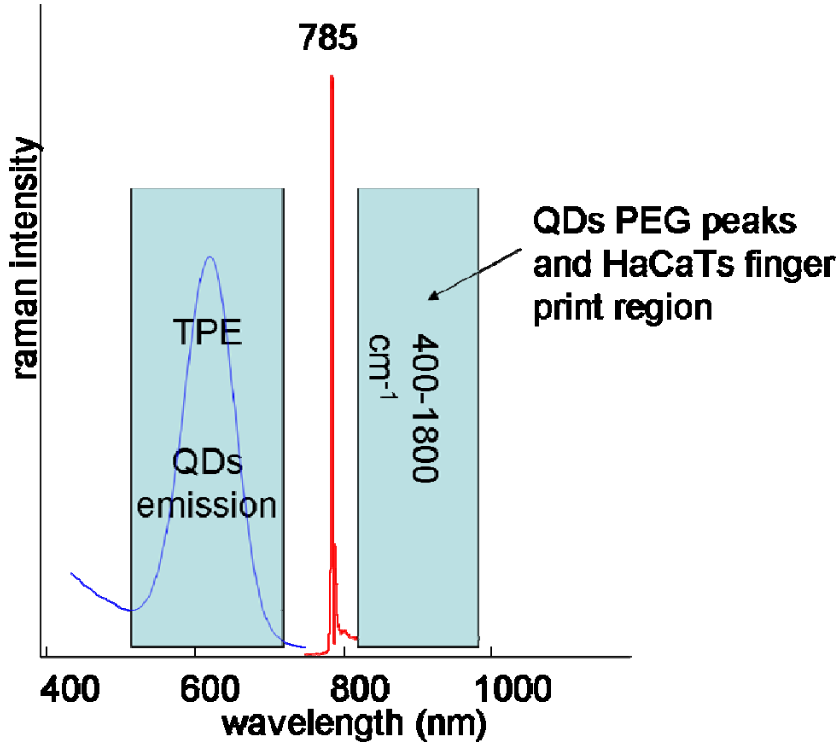

Figure 4.22 Raman scheme of TPFE and finger print region Raman spectra.

Four independent experiments were performed. The Raman spectra were exported to MATLAB and subsequently preprocessed. From the simulated study it was concluded that, regarding the cross-correlation results, the best compromise among the various parameters (range of Maxima, linearity, limit of detection) is the filtering and baseline correction or filtering and first derivative both in the reduced window (800-1250 cm^{-1}). For each experiment, the cross-correlation was performed after a filtering (Savitzky-Golay filters) and a baseline correction or applying the first derivative.

Just before the first experiment, the laser line was changed from 785 nm to 473 nm; because of the strong fluorescence emission at this wavelength, the 473 nm laser of the

Raman microscope is able to map very quickly (0.1 second per point) and give a detailed distribution of the 625QDs within the cell. It was subsequently possible to identify the area of the cell with highest concentration of QDs was and centre the study there (Figure 4.23).

A problem of this methodology is that the lasers of the Raman Spectrometer can lose alignment in the transition from one laser to another one. The process of alignment is quite long and complicated and makes this methodology not suitable for this study.

The problem was overcome by using just the 785 nm laser line and line mapping the fluorescence of 3 or 4 areas of the cell. This procedure is a bit longer and does not produce a complete and detailed fluorescence distribution within the cell but it still can provide an indication of where there are the highest concentrations of QDs are.

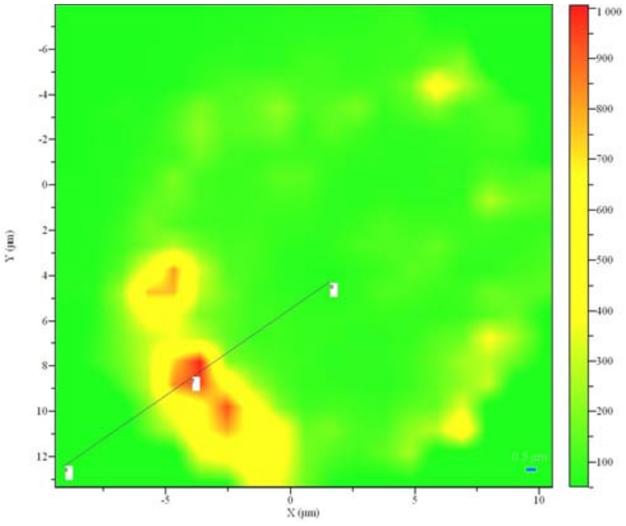

Figure 4.23 473 nm Raman mapping generates the QDs fluorescence distribution within a cell. The solid line indicates a line to be mapped using the 785nm laser.

4.3.1 First experiment

4.3.1a Filtering and baseline correction of the first set of data

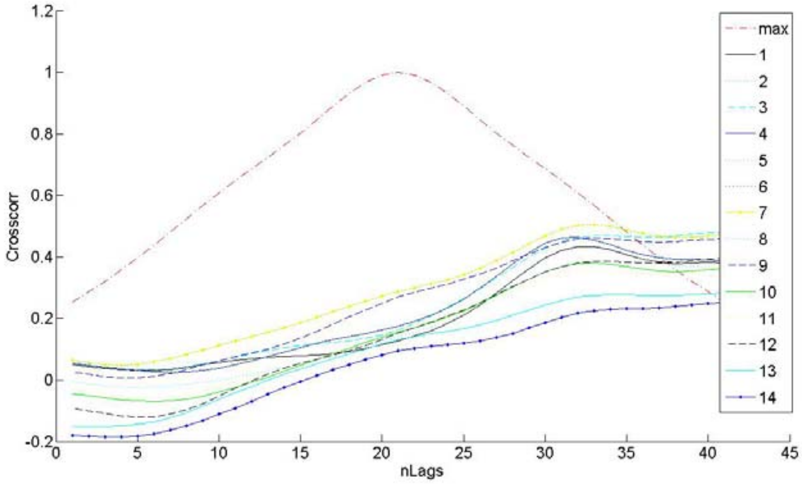

Figure 4.24 Cross-correlation of 14 points of a single HaCaT cell (the max curve is the autocorrelation of the QDs spectrum).

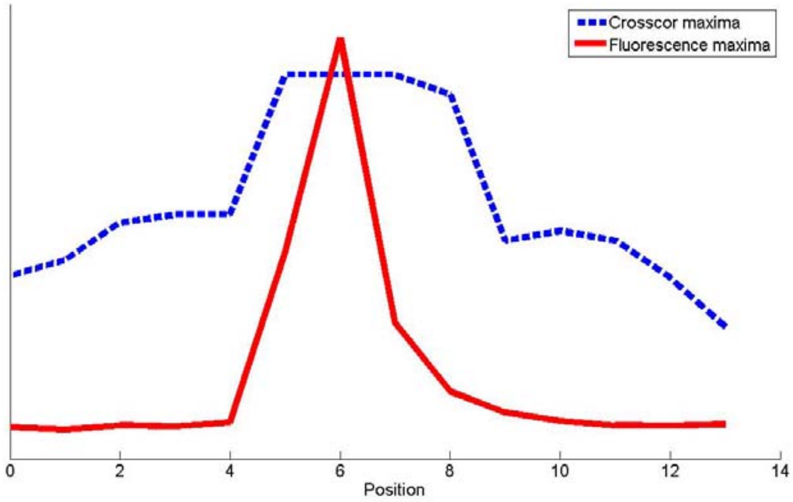

Figure 4.25 Cross-correlation maxima (Stokes side) compared to fluorescence maxima (anti-Stokes side). The y-axis indicates signal strength.

Figure 4.25 shows the profile of the line mapping indicating the fluorescence as measured on the anti-Stokes side and the corresponding profile of cross-correlation maxima. There is a good correspondence between the two profiles. The cross-correlation maximum is plotted as a function of fluorescence in figure 4.26 and an approximate linear correspondence is noted for low values. At high fluorescence intensities, however, the cross-correlation is seen to saturate, which results in the profile of figure 4.5 being rather flat in comparison to the sharply peaked fluorescence profile.

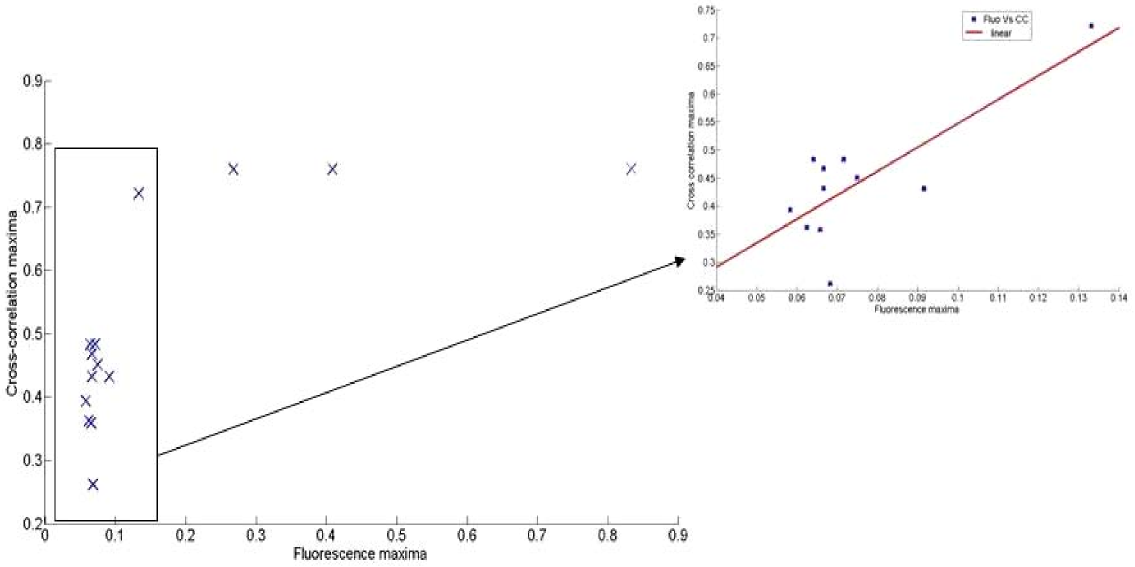

Figure 4.26 Cross-correlation versus fluorescence

4.3.1b Filtering and first derivative of the first set of data

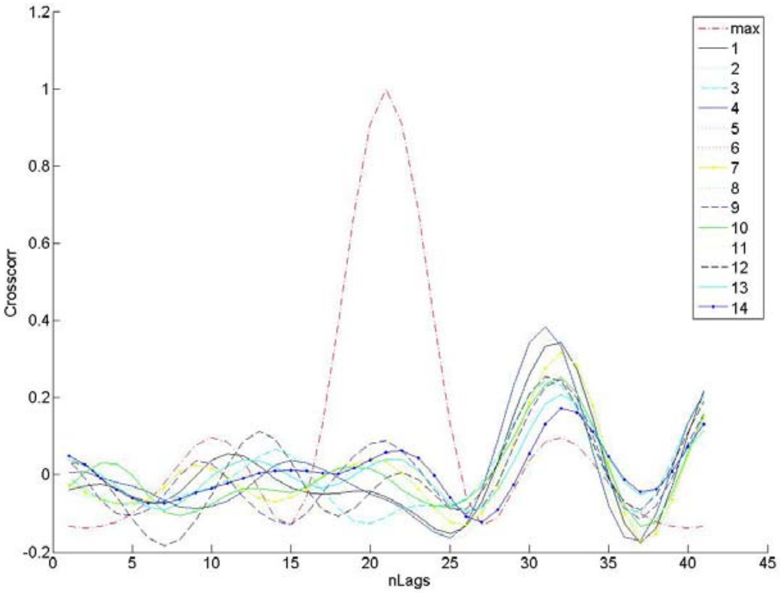

Figure 4.27 Cross-correlation 17 points of an HaCaT cell

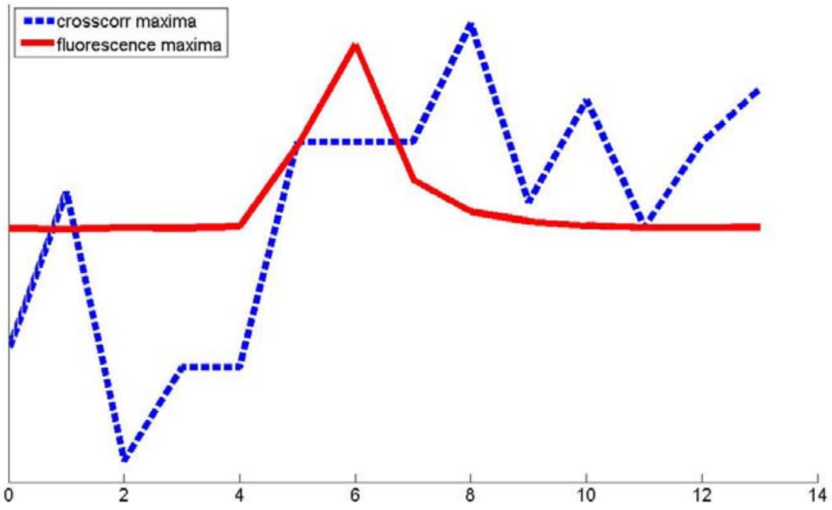

Figure 4.28 Cross-correlation maxima (Stokes side) Vs fluorescence maxima (anti-Stokes side).

For the same dataset, filtering and derivatisation indicates a significantly worse correlation. There is not a clear correspondence between the cross-correlation maxima profile and the fluorescence profile. (Figure 4.28)

4.3.2 Second experiment

4.3.2a Filtering and baseline correction of the second set of data

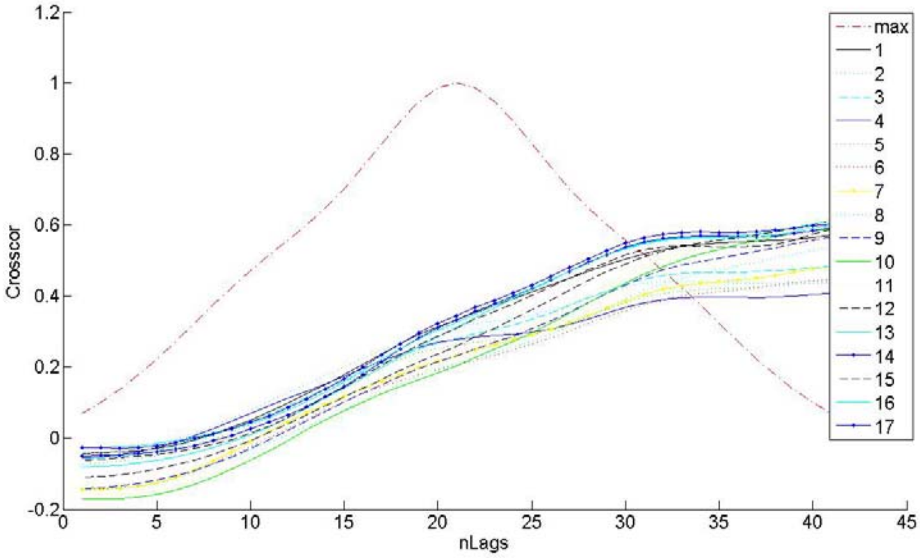

Figure 4.29 Cross-correlation of 17 points of a HaCaT cell.

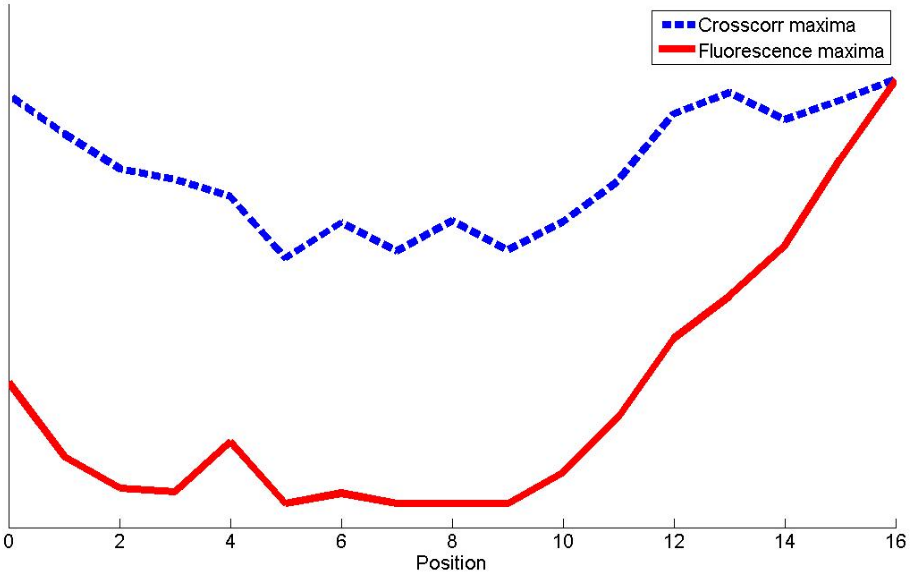

Figure 4.30 Cross-correlation maxima (Stokes side) Vs fluorescence maxima (anti-Stokes side).

Figure 4.30 illustrates a second linear map. The cross correlation profile is very flat compared to the fluorescence profile but it is possible to see a light correspondence. Again, a saturation of the cross-correlation response versus the fluorescence intensity can be observed in Figure 4.31.

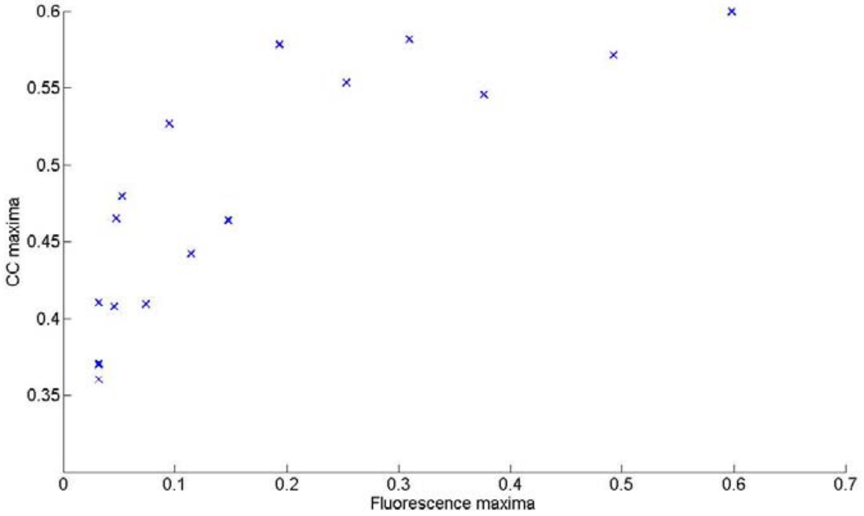

Figure 4.31 Cross-correlation versus fluorescence

4.3.2b Filtering and first derivative of the second set of data.

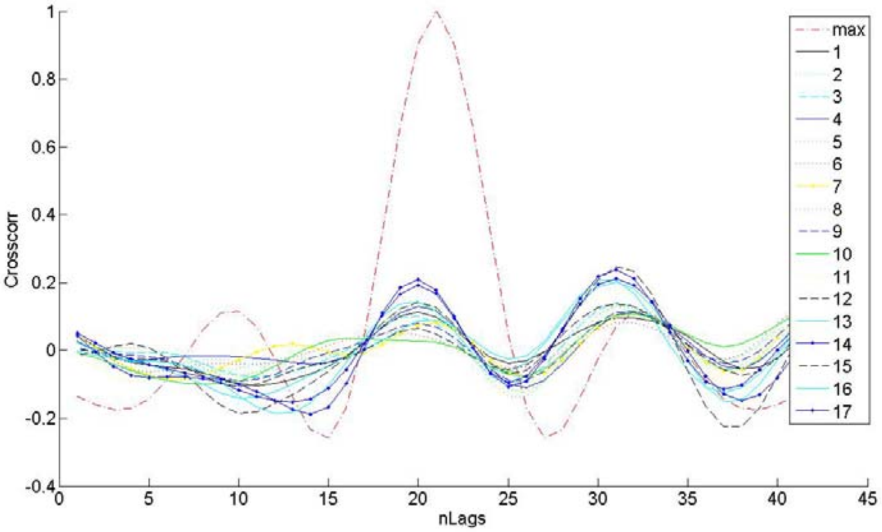

Figure 4.32 Cross-correlation of 17 points of a HaCaT cell.

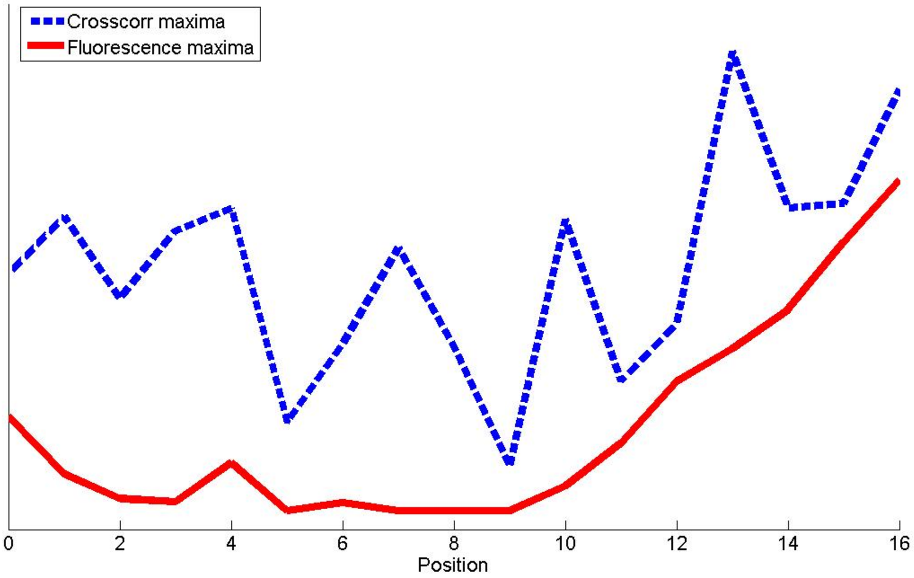

Figure 4.30 Cross-correlation maxima (Stokes side) Vs fluorescence maxima (anti-Stokes side).

As with the first profile, the cross-correlation of the derivatised Raman spectra is noisy and shows a poor correlation with the fluorescence profile.

4.3.3 Third experiment

4.3.3a Filtering and baseline correction of the fifth set of data.

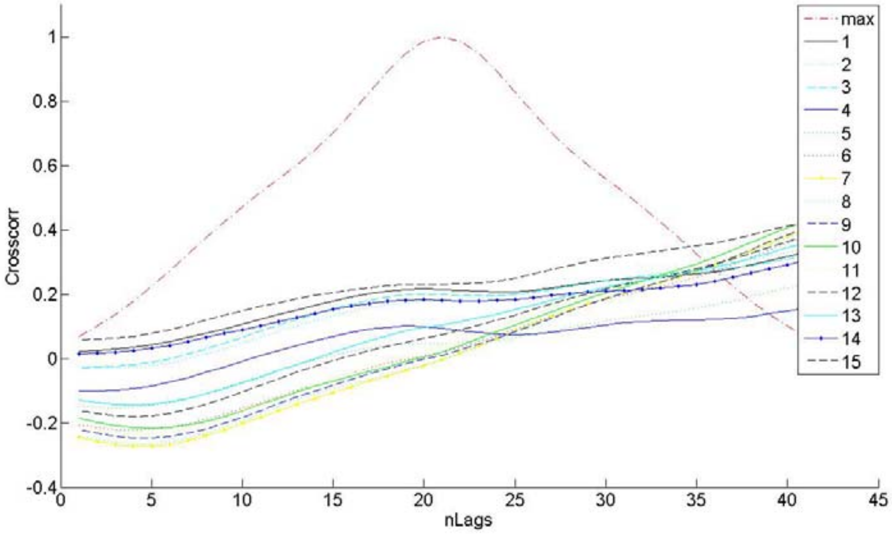

Figure 4.34 Cross-correlationof 15 points of a HaCaT cell

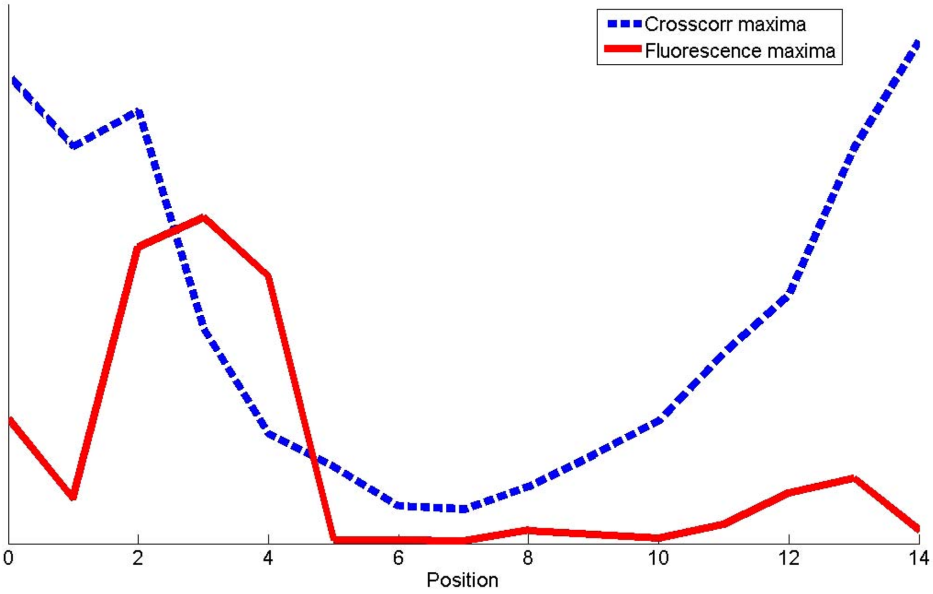

Figure 4.35 Cross-correlation maxima (Stokes side) Vs fluorescence maxima (anti-Stokes side).

In a third linear map, the patterns of the two profiles indicate some similarities; peaks at point 2 and point 13 are present in both profiles even if there is a poor correspondence of the intensities as can see in figure 4.36. Again a saturation of the cross-correlation maximum is inferred.

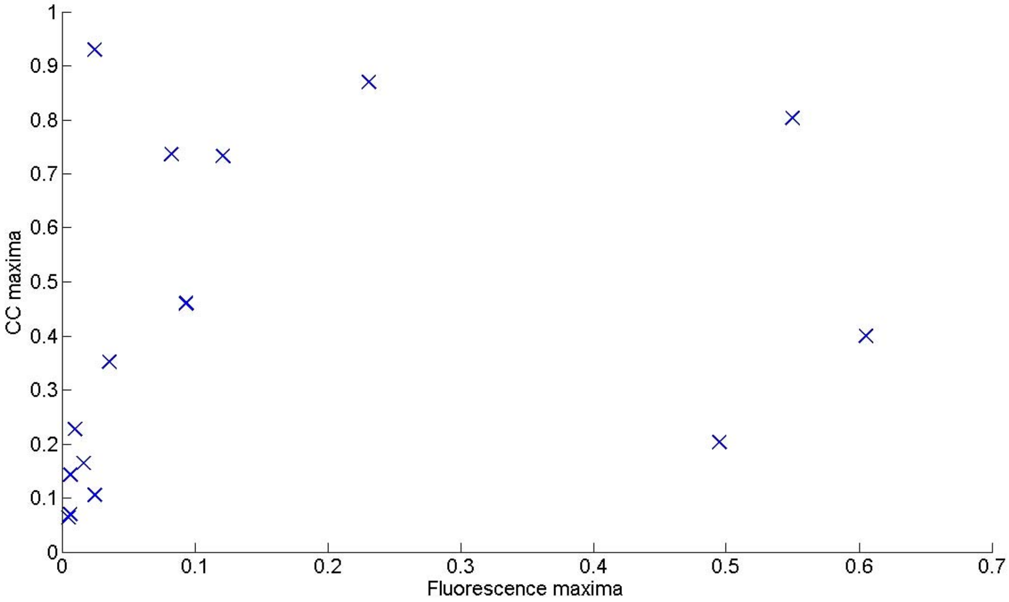

Figure 4.36 Cross-correlation versus fluorescence

4.3.3b Filtering and first derivative of the third set of data

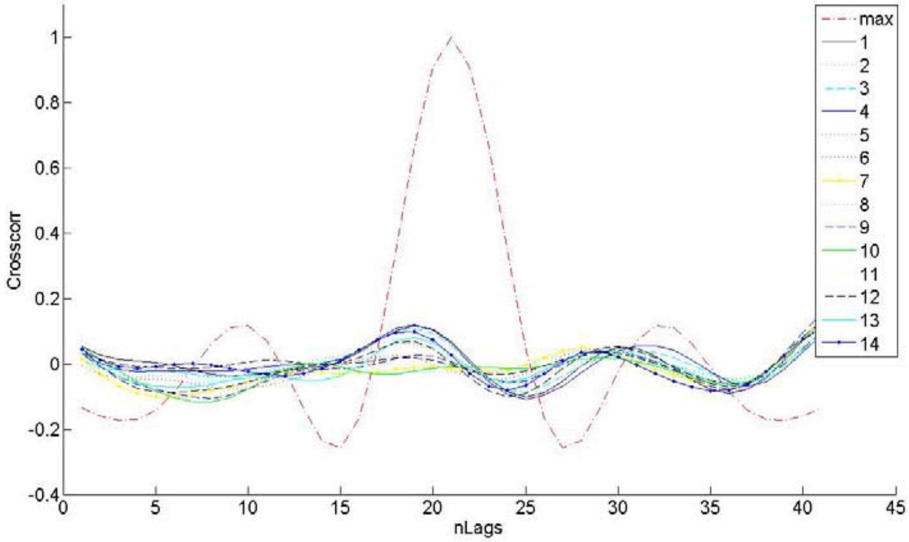

Figure 4.37 Cross-correlation of 15 points of a HaCaT cell.

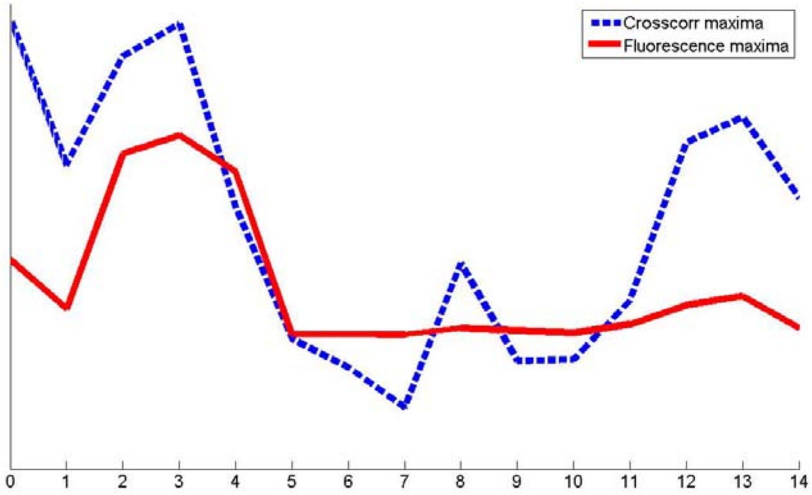

Figure 4.38 Cross-correlation maxima (Stokes side) Vs fluorescence maxima (anti-Stokes side).

In the case of this linear map, the first derivate correlation gives a much better correspondence between the two profiles.

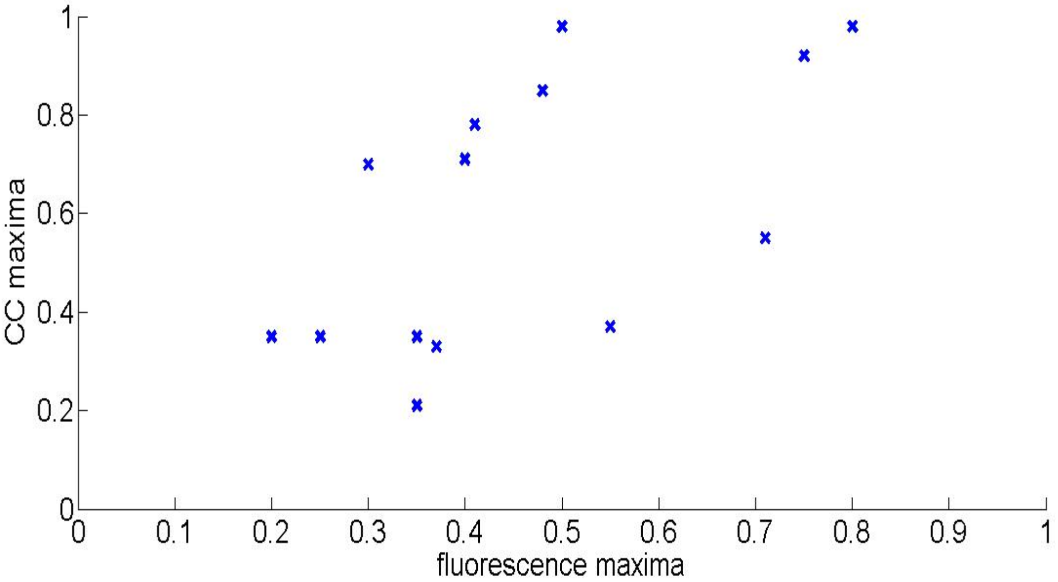

Figure 4.39 Cross-correlation versus fluorescence

4.3.4 Fourth experiment

4.3.4a Filtering and baseline correction of the fourth set of data

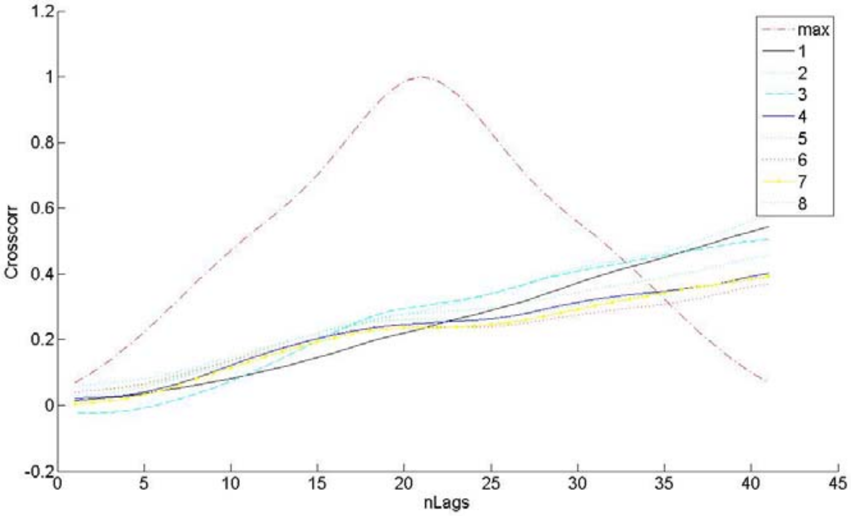

Figure 4.40 Cross-correlation of 8 points of a HaCaT cell.

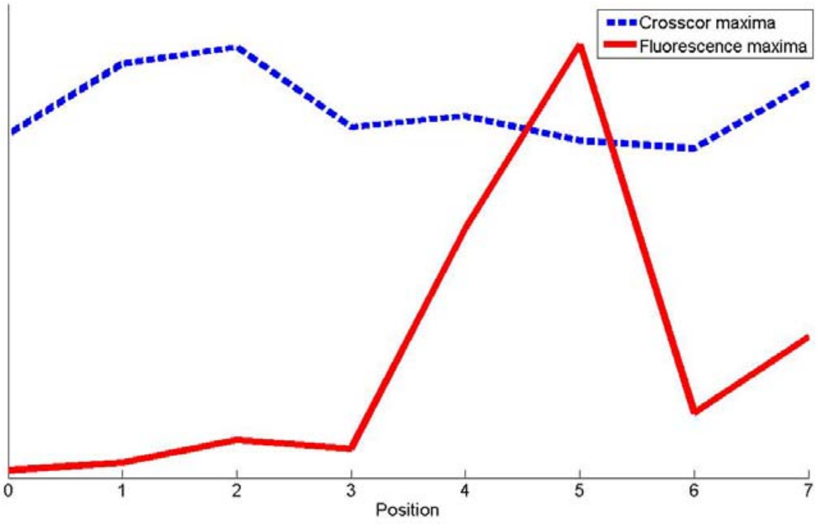

Figure 4.41 Cross-correlation maxima (Stokes side) Vs fluorescence maxima (anti-Stokes side).

The cross correlation profile is very flat while the fluorescence profile has a very intense peak at the sixth point. No correlation is seen between the cross-correlation maximum and the fluorescence intensity as shown in figure 4.41.

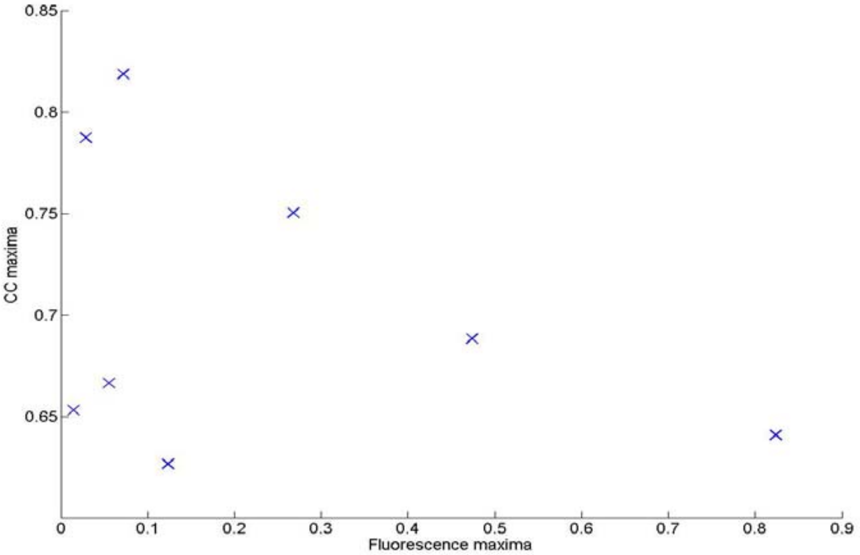

Figure 4.42 Cross-correlation versus fluorescence.

4.3.4b Filtering and first derivative of the fourth set of data

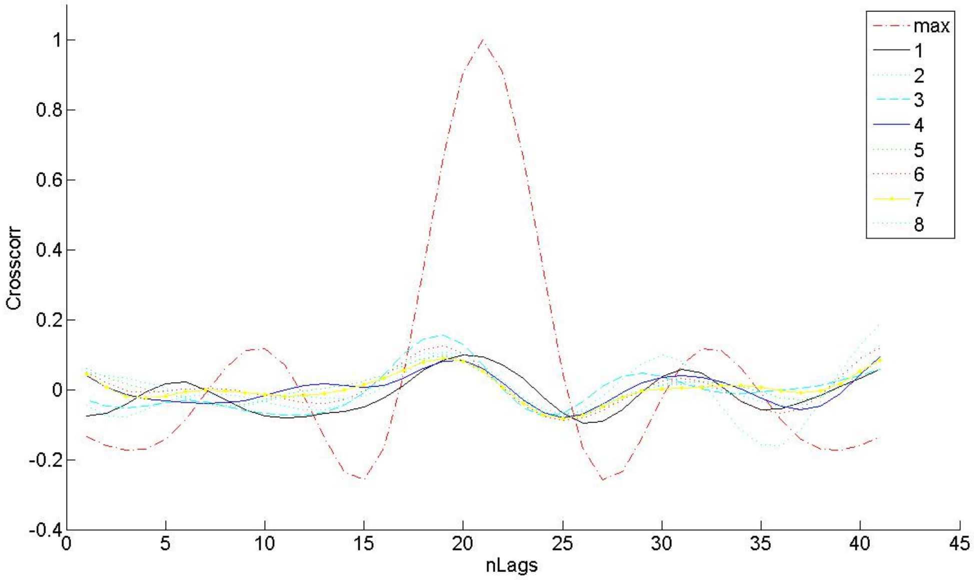

Figure 4.43 Cross-correlation of 8 points of a HaCaT cell.

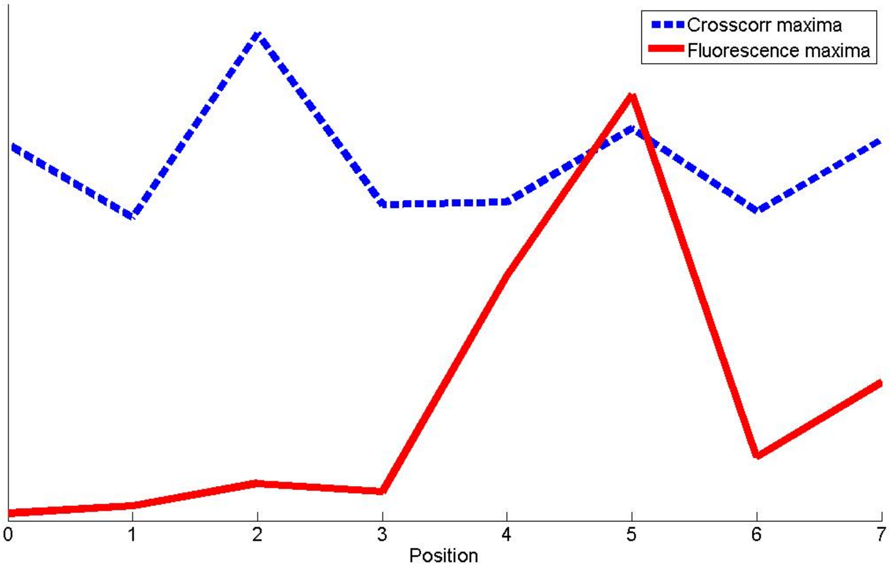

Figure 4.44 Cross-correlation maxima (Stokes side) Vs fluorescence maxima (anti-Stokes side).

As expected, no similarities between the two profiles are observed for the derivatised spectra.

4.3.5 Cross-correlation versus Fluorescence

In Figure 4.44 the cross correlation maxima with respect the fluorescence maxima for all the experimental data are plotted. There is a good correspondence at low correlation values. However, there is a clear saturation of the cross-correlation above a value of approximately 0.5.

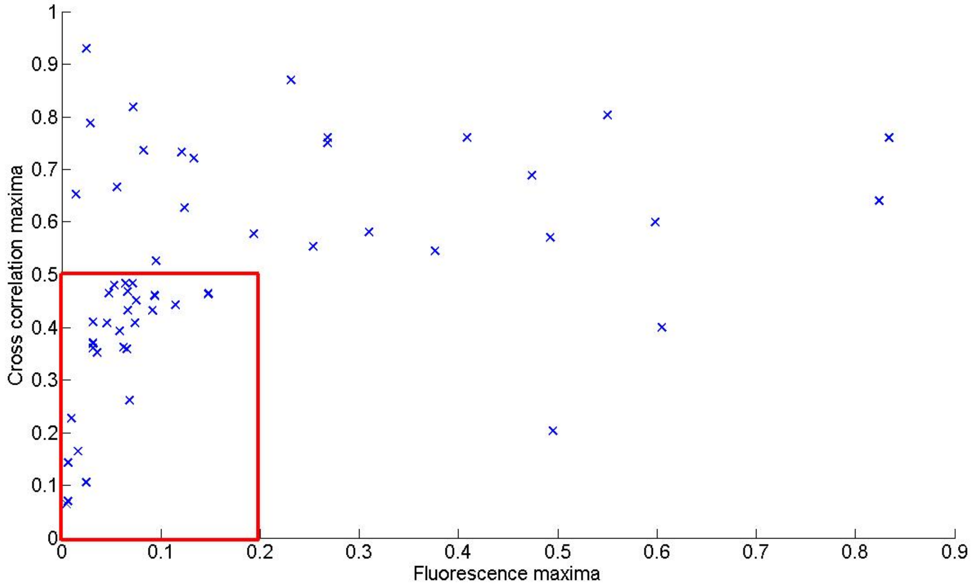

Figure 4.45 Cross-correlation maxima in the X axis and fluorescence maxima in the Y axis for the all experimental data.

4.4 Conclusion

From the experimental study it seemed that it is possible to see in some cases correspondence between the fluorescence profiles and the cross-correlation maxima profiles. However, in general a saturation of the correlation response is observed and a further evaluation of the technique is required.

It is possible to guess for what reasons it is not possible to detect in all cases the QDs presence using the cross-correlation methodology. One reason could be found in the preprocessing technique: the filtering and baseline correction of the spectra are obviously critical to obtaining good correlation and the processes employed here may not be sufficient to achieve a good correct cross-correlation between the spectra.

A second reason could be an intrinsic limit of the cross correlation process applied to this specific technique; from the theoretical study it is possible to notice a lack of linearity for the cross correlation maxima in function of the QDs spectrum percentage. A reasonable explication for this lack of linearity has to consider in all its complexity the Raman technique, the combination of more Raman spectra in a single Raman spectrum, and how the cross correlation process reads the contribution of a second spectrum. Of particular note is the shift of the maximum of the correlation “spectra” from the zero shift or nLag position as a function of concentration in both the simulated and experimental results. It should be expected that maximum correlation should occur at zero shift and this observation is not expected. It may contribute to the nonlinearities observed in the concentration dependent maxima plots.

A third reason may derive from the nature of the PEG spectrum; ideally the cross correlation should be done using a spectrum of PEG in a water solution simulating the conditions within the cell. Unfortunately the PEG of the QDs does not give a very intense Raman spectrum and it was only possible to detect a clear PEG Raman spectrum after drying the QDs nanoparticles on quartz slides. The spectrum of the dried QDs could be shifted with respect to that of the QDs in solution. Thus these possible differences between the dried and solution spectra could affect the cross correlation process.

Nevertheless, the initial exploration of the technique indicates that it is worth refining for the location of nonfluorescent particles in cells. Further exploration could employ nanoparticles with a strong intrinsic Raman signature, but which are also fluorescently labelled. Potential candidates are Fluorescently labelled polystyrene nanoparticles, which are commercially available.

4.5 References

1. Alberts, B., *Molecular Biology of the Cell.*
2. *A. Salvati, Nanobiophysics, Nanochemistry, Nanomedicine & Nanotoxicology Conference 2009, Antigua, 21st-25th Jan, (2009).*
3. *Weisstein, Eric W. "Cross-Correlation." From MathWorld--A Wolfram Web Resource. http://mathworld.wolfram.com/Cross-Correlation.html*
4. R. C. Gonzalez and R. E> Woods, Digital Image Processing (Third edition), Reading, Massachisetts, Addison-Wesley. 1992.
5. Chad, *Automated Method for Subtraction of Fluorescence from Biological Raman Spectra.* Applied Spectroscopy, 2003. 57(11): p. 1363-1367.

Chapter 5

Conclusion

5.1 Conclusion

By most if not all estimates, nanotechnology promises to impact on society to a far greater extent than the Industrial Revolution and is projected to become a $1 Trillion market by 2015. Within this context, Quantum dots (QDs) are very promising nanomaterials which are already exploited commercially and production volumes continue to rise. There is however, almost unanimous opinion among proponents and sceptics alike that attention to potential environmental and human risks of nanomaterials is required.

So far, issues regarding adverse health and environmental effects of QDs have not been resolved, but in this study contribution is made for a specific class of QDs, CdSe/ZnS QDs coated with PEG.

In this study, a range of different techniques are explored with the aim of better understanding the interaction between human cells and QDs and consequently identifing the health risks derived from the contact with these NPs.

The cytotoxicity study showed that the QDs (CdSe/ZnS covered with PEG) are not particularly toxic even at high concentration (200 nM) and after long exposure (96 hrs).

Interestingly, the combination of QDs and solar light exposure reduced the cell viability significantly, suggesting that they are phototoxic.

This preliminary result is particularly important in relation to the risks to human health associated with these NPs. Anyone working with QDs or using any device made with

QDs has to be aware that the combination of exposure to these nanoparticles and to the sun light is potentially harmful. This lay be of particular importance given that these materials are employed as labels for targeted drugs and photo dynamic therapy agents [1,2].

In order to visualize the interaction with the cells, confocal microscopy was employed. This technique revealed the internalization of the QDs within 1 h of exposure and more specifically clearly demonstrated that the particles are encapsulated within lysosomes. Such an intracellular mechanism for anionic or neutral particles has been postulated [3]. Whereas cationic particles are easily coated in (negatively charged) proteins contained in the cell culture medium, the anionic or neutral particles are recognized as foreign, engulfed in endosomes and then lysosomes for disposal [4]. The highly fluorescent QDs are thus a model particle for studying the mechanisms of NP transport within cells.

Using an excitation wavelength of 785 nm, two-photon excitation fluorescence in QDs (emission at 625 nm), can be observed. Within the Raman spectrometer, the fluorescent emission is observed as the anti-Stokes Raman signal, together with the usual Stokes Raman scatter of the particle.

When exposed to the QDs, fluorescence or two photon fluorescence can be mapped within a cell. However, since most particles are not fluorescent, it remains a challenge to track and localize them within a cell. Raman spectroscopy can localize the particles due to their unique fingerprint spectrum. However, the spectrum is often weak and swamped by the cellular spectrum. In this study, a cross correlation technique has been employed for the first time. The QD spectrum has been correlated within the cellular spectrum and through a cross-correlation process their presence and location within a cell can be determined. The preliminary results suggest that this new technique theoretically and experimentally could work although improvements in the preprocessing of the data are required. The potential success of this technique highly depends on the signature Raman spectrum; in the case explored here, the PEG spectrum is not very intense and it will be interesting to validate this technique using a nanoparticulate material with a much more intense Raman spectrum. Ultimately if developed, the technique could track nonfluorescent nanoparticles, and even therapeutic or pharmaceutical agents in cells.

5.2 References

1. Juzenas, P., et al., *Quantum dots and nanoparticles for photodynamic and radiation therapies of cancer.* Advanced Drug Delivery Reviews, 2008. 60(15): p. 1600-1614.

2. Gao, X., et al., *In vivo cancer targeting and imaging with semiconductor quantum dots.* Nat Biotechnol, 2004. 22(8): p. 969-76.

3. Andre E. Nel , L.M.a.d., Darrell Velegol , Tian Xia , Eric M. V. Hoek , Ponisseril Somasundaran , Fred Klaessig , Vince Castranova & Mike Thompson, *Understanding biophysicochemical interactions at the nano|[ndash]|bio interface.* Nature Materials 2009. **8**: p. 543–557.

4. Goffrey M. Cooper,*The Cell – A molecular approach.* Second Edition **8**: p. 543–557.

Appendix A

MATLAB codes

Cross correlation of QDs within a cell

(Baseline correction)

```
%% Cross Correlation file
%%ccorr.m baseline correction data full range 400 1800 cm-1
%%% lorenzo Salford   %15/02/2010


matrix=load('cross corr.txt');
%wavenumber=matrix(1:end,1);
%cell=matrix(:,2);
%QD=matrix(:,3);
%range 600-1800


range=141:982
wavenumber=matrix(range,1);
cell=matrix(range,2);
QD=matrix(range,3);


cell=normaliz(cell')';
QD=normaliz(QD')';


%cell=sgolayfilt(cell,5,13);cell=diff(cell);
%QD=sgolayfilt(QD,5,13);QD=diff(QD);
```

```
order=1;
sg_order=5;
window=13;
%rubberband - baseline correction
 cell=Raman_PreProcess(cell,wavenumber,order,sg_order,window);
 QD=Raman_PreProcess(QD,wavenumber,order,sg_order,window);

figure(1)

plot(wavenumber,cell,'r-');hold on
plot(wavenumber,QD,'b-');hold off

cell_QD=cell+QD;
cell_QD2=cell+(QD/2);
cell_QD5=cell+(QD/5);
cell_QD10=cell+(QD/10);
cell_QD20=cell+(QD/20);
cell_QD50=cell+(QD/50);
cell_QD100=cell+(QD/100);
cell_QD200=cell+(QD/200);
cell_QD500=cell+(QD/500);
cell_QD1000=cell+(QD/1000);
cell_QD2000=cell+(QD/2000);
cell_QD5000=cell+(QD/5000);
cell_QD10000=cell+(QD/10000);


%second normalization
```

```
cell_QD=normaliz(cell_QD')';

cell_QD2=normaliz(cell_QD2')';

cell_QD5=normaliz(cell_QD5')';

cell_QD10=normaliz(cell_QD10')';

cell_QD20=normaliz(cell_QD20')';

cell_QD50=normaliz(cell_QD50')';

cell_QD100=normaliz(cell_QD100')';

cell_QD200=normaliz(cell_QD200')';

cell_QD500=normaliz(cell_QD500')';

cell_QD1000=normaliz(cell_QD1000')';

cell_QD2000=normaliz(cell_QD2000')';

cell_QD5000=normaliz(cell_QD5000')';

cell_QD10000=normaliz(cell_QD10000')';


%range 600-1800 (1-842); 800-1800 (141-842) 800-1250 (141-457)

range1=141:842

cell=cell(range1);

cell_QD=cell_QD(range1);

cell_QD2=cell_QD2(range1);

cell_QD5=cell_QD5(range1);

cell_QD10=cell_QD10(range1);

cell_QD20=cell_QD20(range1);

cell_QD50=cell_QD50(range1);

cell_QD100=cell_QD100(range1);

cell_QD200=cell_QD200(range1);

cell_QD500=cell_QD500(range1);

cell_QD1000=cell_QD1000(range1);

cell_QD2000=cell_QD2000(range1);

cell_QD5000=cell_QD5000(range1);

cell_QD10000=cell_QD10000(range1);
```

```
QD=QD(range1);
wavenumber=wavenumber(range1);
figure(2)

plot(wavenumber,cell_QD,'r-');hold on
plot(wavenumber,cell_QD10,'b-');
plot(wavenumber,cell_QD100,'k-');
plot(wavenumber,cell_QD1000,'g-');
plot(wavenumber,cell_QD10000,'c-');
plot(wavenumber,cell_QD10000,'c-');hold off

h = legend('Cell + QD','Cell + QD/10','Cell + QD/100','Cell + QD/1000','Cell + QD/10000','Location','NorthEast');
set(h,'Interpreter','none')

%Cross-correlation
%conv or crosscorr
%max
%window 600-800 o 200-300
ccorr_QDmax=crosscorr(QD,QD);
%window=200:300;
%concentrations
ccorr_QD=crosscorr(cell_QD,QD);y(14)=max(ccorr_QD);
ccorr_QD2=crosscorr(cell_QD2,QD);y(13)=max(ccorr_QD2);
ccorr_QD5=crosscorr(cell_QD5,QD);y(12)=max(ccorr_QD5);
ccorr_QD10=crosscorr(cell_QD10,QD);y(11)=max(ccorr_QD10);
ccorr_QD20=crosscorr(cell_QD20,QD);y(10)=max(ccorr_QD20);
ccorr_QD50=crosscorr(cell_QD50,QD);y(9)=max(ccorr_QD50);
ccorr_QD100=crosscorr(cell_QD100,QD);y(8)=max(ccorr_QD100);
ccorr_QD200=crosscorr(cell_QD200,QD);y(7)=max(ccorr_QD200);
```

```
ccorr_QD500=crosscorr(cell_QD500,QD);y(6)=max(ccorr_QD500);
ccorr_QD1000=crosscorr(cell_QD1000,QD);y(5)=max(ccorr_QD1000);
ccorr_QD2000=crosscorr(cell_QD2000,QD);y(4)=max(ccorr_QD2000);
ccorr_QD5000=crosscorr(cell_QD5000,QD);y(3)=max(ccorr_QD5000);
ccorr_QD10000=crosscorr(cell_QD10000,QD);y(2)=max(ccorr_QD10000);
%min
ccorr_QDmin=crosscorr(cell,QD);y(1)=max(ccorr_QDmin);

for i=1:13
   ymax=max(y);
   ymin=min(y);
   delta=ymax-ymin;
   if ((y(i)-y(i+1))/delta ) <= 0.0001
      limit=i+1
   end
end

figure(3)
plot(ccorr_QDmax,'-.r');hold on
plot(ccorr_QD,'k-');
plot(ccorr_QD2,'c:');
plot(ccorr_QD5,'c--');
plot(ccorr_QD10,'b-');
plot(ccorr_QD20,'g:');
plot(ccorr_QD50,'r--');
plot(ccorr_QD100,'k-');
plot(ccorr_QD200,'c:');
plot(ccorr_QD500,'b--');
plot(ccorr_QD1000,'g-');
plot(ccorr_QD2000,'r:');
```

```
plot(ccorr_QD5000,'k--');
plot(ccorr_QD10000,'c-');
plot(ccorr_QDmin,'b.-');hold off

h = legend('max','1','1/2','1/5','1/10','1/20','1/50','1/100','1/200','1/500','1/1000','1/2000','1/5000','1/10000','min','Location','NorthEast');
set(h,'Interpreter','none')

x=[0,1/10000,1/5000,1/2000,1/1000,1/500,1/200,1/100,1/50,1/20,1/10,1/5,1/2,1];

figure(4)
plot(x,y,'ro-')
set(gca,'XDir','reverse')

figure(5)
y2=y-y(1);
plot(x,y2,'ro-')
```

Raman Preprocess code

```
function [X]=Raman_PreProcess(X,wavenumber,order,sg_order,window)

%Copyright Peter Knief  21-10-09

%%%%%BACKGROUND CORRECTION%%%%%

X=(rubberband_pk(X',0.01,0))';
pause (1);
close all;
```

```
% SG filtering
X=sgolayfilt(X,sg_order,window);
% %X_corr=diff(X_corr);
```

Cross-correlation of experimental data

```
%% Cross Correlation file
%%ccorr.m 800-1800

%Copyright Lorenzo Salford          17/02/2010

matrix=load('table1.txt');
range=141:982;
wavenumber=matrix(range,1);
cell1=matrix(range,3);
cell2=matrix(range,4);
cell3=matrix(range,5);
cell4=matrix(range,6);
cell5=matrix(range,7);
cell6=matrix(range,8);
cell7=matrix(range,9);
cell8=matrix(range,10);
cell9=matrix(range,11);
cell10=matrix(range,12);
cell11=matrix(range,13);
cell12=matrix(range,14);
cell13=matrix(range,15);
cell14=matrix(range,16);
```

```
cell15=matrix(range,17);


QD=matrix(range,2);


cell1=normaliz(cell1')';
cell2=normaliz(cell2')';
cell3=normaliz(cell3')';
cell4=normaliz(cell4')';
cell5=normaliz(cell5')';
cell6=normaliz(cell6')';
cell7=normaliz(cell7')';
cell8=normaliz(cell8')';
cell9=normaliz(cell9')';
cell10=normaliz(cell10')';
cell11=normaliz(cell11')';
cell12=normaliz(cell12')';
cell13=normaliz(cell13')';
cell14=normaliz(cell14')';
cell15=normaliz(cell15')';
 QD=normaliz(QD')';


%cell=sgolayfilt(cell,5,13);%cell=diff(cell);
%QD=sgolayfilt(QD,5,13);%QD=diff(QD);


ordercell=2;
orderQD=2;
sg_order=5;
window=13;
cell1=Raman_PreProcess2(cell1,wavenumber,ordercell,sg_order,window);
cell2=Raman_PreProcess2(cell2,wavenumber,ordercell,sg_order,window);
```

```
cell3=Raman_PreProcess2(cell3,wavenumber,ordercell,sg_order,window);
cell4=Raman_PreProcess2(cell4,wavenumber,ordercell,sg_order,window);
cell5=Raman_PreProcess2(cell5,wavenumber,ordercell,sg_order,window);
cell6=Raman_PreProcess2(cell6,wavenumber,ordercell,sg_order,window);
cell7=Raman_PreProcess2(cell7,wavenumber,ordercell,sg_order,window);
cell8=Raman_PreProcess2(cell8,wavenumber,ordercell,sg_order,window);
cell9=Raman_PreProcess2(cell9,wavenumber,ordercell,sg_order,window);
cell10=Raman_PreProcess2(cell10,wavenumber,ordercell,sg_order,window);
cell11=Raman_PreProcess2(cell11,wavenumber,ordercell,sg_order,window);
cell12=Raman_PreProcess2(cell12,wavenumber,ordercell,sg_order,window);
cell13=Raman_PreProcess2(cell13,wavenumber,ordercell,sg_order,window);
cell14=Raman_PreProcess2(cell14,wavenumber,ordercell,sg_order,window);
cell15=Raman_PreProcess2(cell15,wavenumber,ordercell,sg_order,window);

QD=Raman_PreProcess2(QD,wavenumber,orderQD,sg_order,window);


figure(1)
%wavenumber=wavenumber(1:end-1);
plot(wavenumber,cell7,'r-');hold on
plot(wavenumber,QD,'b-');hold off
%wavenumber=wavenumber(1:end-1);


figure(2)


plot(wavenumber,cell1,'r-');hold on
plot(wavenumber,cell2,'b-');
plot(wavenumber,cell3,'k-');
plot(wavenumber,cell4,'g-');
plot(wavenumber,cell5,'c-');
plot(wavenumber,cell6,'r--');
```

```
plot(wavenumber,cell7,'b--');
plot(wavenumber,cell8,'k--');
plot(wavenumber,cell9,'g--');
plot(wavenumber,cell10,'c--');
plot(wavenumber,cell11,'k--');
plot(wavenumber,cell2,'b--');
plot(wavenumber,cell3,'k--');
plot(wavenumber,cell4,'g--');
plot(wavenumber,cell5,'b--'); hold off

h = legend('Cell1','Cell2','Cell3','Cell4','Cell5','Cell6','Cell7','Cell8','Cell9','Cell10','Cell11','Cell12','Cell13','Cell14','Cell15','Location','NorthEast');
set(h,'Interpreter','none')

%Cross-correlation
%conv or crosscorr
%max
%range 800-1250
range1=141:457
cell1=cell1(range1);
cell2=cell2(range1);
cell3=cell3(range1);
cell4=cell4(range1);
cell5=cell5(range1);
cell6=cell6(range1);
cell7=cell7(range1);
cell8=cell8(range1);
cell9=cell9(range1);
cell10=cell10(range1);
cell11=cell11(range1);
```

```
cell12=cell12(range1);
cell13=cell13(range1);
cell14=cell14(range1);
cell15=cell15(range1);
QD=QD(range1);

ccorr_QDmax=crosscorr(QD,QD);window=8:32;
%concentrations
win=50;
[ccorr_QD1,Lags1,Bounds1]=crosscorr(cell1,QD);y(1)=max(ccorr_QD1(window));
[ccorr_QD2,Lags2,Bounds2]=crosscorr(cell2,QD);y(2)=max(ccorr_QD2(window));
[ccorr_QD3,Lags3,Bounds3]=crosscorr(cell3,QD);y(3)=max(ccorr_QD3(window));
[ccorr_QD4,Lags4,Bounds4]=crosscorr(cell4,QD);y(4)=max(ccorr_QD4(window));
[ccorr_QD5,Lags5,Bounds5]=crosscorr(cell5,QD);y(5)=max(ccorr_QD5(window));
[ccorr_QD6,Lags6,Bounds6]=crosscorr(cell6,QD);y(6)=max(ccorr_QD6(window));
[ccorr_QD7,Lags7,Bounds7]=crosscorr(cell7,QD);y(7)=max(ccorr_QD7(window));
[ccorr_QD8,Lags8,Bounds8]=crosscorr(cell8,QD);y(8)=max(ccorr_QD8(window));
[ccorr_QD9,Lags9,Bounds9]=crosscorr(cell9,QD);y(9)=max(ccorr_QD9(window));
[ccorr_QD10,Lags10,Bounds10]=crosscorr(cell10,QD);y(10)=max(ccorr_QD10(window));
[ccorr_QD11,Lags11,Bounds11]=crosscorr(cell11,QD);y(11)=max(ccorr_QD11(window));
[ccorr_QD12,Lags12,Bounds12]=crosscorr(cell12,QD);y(12)=max(ccorr_QD12(window));
[ccorr_QD13,Lags13,Bounds13]=crosscorr(cell13,QD);y(13)=max(ccorr_QD13(window));
[ccorr_QD14,Lags14,Bounds14]=crosscorr(cell14,QD);y(14)=max(ccorr_QD14(window));
[ccorr_QD15,Lags15,Bounds15]=crosscorr(cell15,QD);y(15)=max(ccorr_QD15(window));

figure(3)
plot(ccorr_QDmax,'-.r');hold on
plot(ccorr_QD1,'k-');
plot(ccorr_QD2,'c:');
plot(ccorr_QD3,'c--');
```

```
plot(ccorr_QD4,'b-');

plot(ccorr_QD5,'g:');

plot(ccorr_QD6,'r:');

plot(ccorr_QD7,'y.-');

plot(ccorr_QD8,'c:');

plot(ccorr_QD9,'b--');

plot(ccorr_QD10,'g-');

plot(ccorr_QD11,'y:');

plot(ccorr_QD12,'k--');

plot(ccorr_QD13,'c-');

plot(ccorr_QD14,'b.-');

plot(ccorr_QD15,'k--');hold off


h = legend('max','1','2','3','4','5','6','7','8','9','10','11','12','13','14','15','16','17','Location','NorthEast');

set(h,'Interpreter','none')


%max abs

figure(4)


x=0:14;

yfl=[4200,1500,10000,11000,9000,120,110,90,450,300,180,650,1700,2200,450];

nor_y=y/norm(y);

nor_yfl=yfl/norm(yfl);

nor_y=2*nor_y

plot(x,nor_y,'b'); hold on

plot(x,nor_yfl,'r');hold off


window2=20:22

%concentrations

win=50;
```

```
y2(1)=max(ccorr_QD1(window2));
y2(2)=max(ccorr_QD2(window2));
y2(3)=max(ccorr_QD3(window2));
y2(4)=max(ccorr_QD4(window2));
y2(5)=max(ccorr_QD5(window2));
y2(6)=max(ccorr_QD6(window2));
y2(7)=max(ccorr_QD7(window2));
y2(8)=max(ccorr_QD8(window2));
y2(9)=max(ccorr_QD9(window2));
y2(10)=max(ccorr_QD10(window2));
y2(11)=max(ccorr_QD11(window2));
y2(12)=max(ccorr_QD12(window2));
y2(13)=max(ccorr_QD13(window2));
y2(14)=max(ccorr_QD14(window2));
y2(15)=max(ccorr_QD15(window2));

%max around 21
figure (5)
nor_y2=y2/norm(y2);
nor_y2=2*nor_y2
plot(x,nor_y2,'b'); hold on
plot(x,nor_yfl,'r');hold off

figure (6)
plot(nor_y2,nor_yfl)
yx=(nor_y2)';
yy=(nor_yfl)';
```

Appendix B

Conferences

1) DASIM4 – Diagnostic Applications of Synchroton Infrared Microspectroscopy

12th and 13th, June 2008

Dublin, Ireland

2) BIGSS' 08 BioPhotonics and Imaging Graduate – Summer School

August 29 – September 02, 2008

Ballyvaughan, Co. Clare, Ireland

Poster

3) SPEC 2008: Shedding Light on Disease: Optical Diagnosis for the New Millenium-

October 25 – October 29, 2008

São José dos Campos, Sao Paulo, Brazil

Poster

4) NBIP 2009: NBIP Ireland inaugural Conference- March 26, 2009, Dublin, Ireland

Poster

5)ICAVS5 2009: 5th International Conference on Advanced Vibrational Spectroscopy – 12-17 July, 2009.

Melbourne, Australia

Poster

6) ECSMB 2009: XIII European Conference on the Spectroscopy of Biological Molecules- 28 August 2009 - 02 September 2009

Palermo, Italy.

Poster

Prize as best poster

7) INSPIRE Bionano international conference-

October 15-16, 2009

Dublin, Ireland

Poster